Carbonized Metal-Organic Frameworks as Bifunctional Electrocatalysts for Oxygen Reduction/Evolution Reactions

by

Hamidreza Parsimehr

Master of Science, Iran Polymer and Petrochemical Institute, 2017

A Thesis Submitted in Partial Fulfillment

of the Requirements for the Degree of

Master of Science

in the Graduate Academic Unit of Chemistry

Supervisor: Anna Ignaszak, Ph.D., Department of Chemistry

Examining Board: Stijn De Baerdemacker, Ph.D., Department of Chemistry
Adam Dyker, Ph.D., Department of Chemistry
Zahra Khatami, PhD., Department of Electrical Engineering

This thesis is accepted by the
Dean of Graduate Studies

THE UNIVERSITY OF NEW BRUNSWICK

October 2023

ABSTRACT

Electrochemical energy devices like batteries and fuel cells as benign high-performance solutions for energy issues have been swiftly developed in recent decades. Both metal-air batteries and fuel cells use a positive electrode (cathode) that has a similar chemical composition to facilitate oxygen reduction reactions (ORR) during their operation. The second important reaction involving oxygen species is the oxygen evolution reaction (OER). This process is used in water electrolyzers to generate oxygen. An electrocatalyst incorporated in the electrodes in the above-listed energy systems is key to the efficient ORR and OER processes. Such electrocatalyst plays a critical role in overall performance, stability, and long cycle lifetime.

The main objective is to synthesize and evaluate the electrochemical performance of heteroatom-doped carbons made by pyrolysis of metal-organic frameworks (MOFs) and zeolitic imidazole frameworks (ZIFs). Although some of these catalysts demonstrated decent activity, further work is needed to prove their electrocatalytic performance.

ACKNOWLEDGEMENTS

I want to thank my supervisor Dr. Anna Ignaszak who has been immensely helpful throughout our time together. I want to acknowledge my colleagues who have helped me throughout my work on this thesis. Also, I would like to thank Dr. Adam Dyker and Dr. Stijn De Baerdemacker, who read and reviewed this thesis. Finally, I would like to thank Dr. Stijn De Baerdemacker and Dr. Zahra Khatami, who examined this thesis.

Table of Contents

List of Tables

List of Figures

List of Abbreviations

2-MIM	2-Methylimidazole
AEM	Adsorbate evolution mechanism
ATR	Attenuated Total Reflectance
BET	Brunauer-Emmett-Teller Surface Analysis
BOE	Bifunctional Oxygen Electrocatalyst
BTC	1,3,5-Benzenetricarboxylic acid
CO_2	Carbon dioxide
CoFeZIF	Cobalt/Iron-based hybrid ZIF
CoN	Cobalt (II) nitrate hexahydrate ($(Co(NO_3)_2)\times 6\ H_2O$)
CoZIF	Cobalt-based ZIF (ZIF-67)
CuN	Copper (II) nitrate pentahydrate ($(Cu(NO_3)_2)\times 5\ H_2O$)
CV	Cyclic Voltammetry
DI	Deionized water
EES	Electrochemical Energy Storage Devices
$E_{\frac{1}{2}}$	Half-wave potential
E_{onset}	Onset potential
FCs	Fuel Cells
FeN	Iron (III) nitrate nonahydrate ($(Fe(NO_3)_3)\times 9\ H_2O$)
FeZIF	Iron-based ZIF
FT-IR	Fourier-transform infrared
GDE	Gas Diffusion Electrode
g	gram
HKUST MOF	Hong Kong University of Science and Technology Metal-Organic Framework
I_2	Iodine
K-L	Koutecky-Levich
KOH	Potassium hydroxide
LOM	Lattice oxygen-mediated mechanism
LSV	Linear Sweep Voltammetry
Ml	Metal
MABs	Metal-Air Batteries
MIM	2-methylimidazole
mg	Milligram
MOFs	Metal-Organic Frameworks
ml	Milliliter
N_2	Nitrogen
N-doped	Nitrogen-doped
O_2	Oxygen
OER	Oxygen Evolution Reaction
ORR	Oxygen Reduction Reaction
PEMFCs	Proton-Exchange Membrane Fuel Cell
PPy	Polypyrrole
PtC	Platinum (20%)-carbon
RDE	Rotating disc electrode

RPM	Revolutions per minute
RRDE	Rotating ring disc electrode
XPS	X-ray photoelectron spectroscopy
XRD	X-ray diffraction spectroscopy
ZABs	Zinc-Air Batteries
ZIFs	Zeolitic Imidazolate Framework
ΔE	Bifunctional potential
µl	Microliter

1.0 Introduction

1.1 Energy

Energy consumption is an uprising concern that we are facing worldwide. Conventional hydrocarbons massively used in energy production led to severe damage to the environment as their combustion caused an enormous production of greenhouse gases. Therefore, a transition from fossil fuel-based energies to clean energies is one of the priorities of our lifetime. Fortunately, it has adapted renewable technologies (hydropower, solar, wind, and nuclear energy) at a reasonably low cost, so there is a hope that provide a cleaner and healthier planet for future generations, and slow down global warming.

Electrochemical energy - a type of energy produced at zero (or almost zero) CO_2 emission - can significantly contribute to reduce pollution, in particular when it is greatly adapted in transportation. Hence, the production and storage of electrochemical energy have been extensively studied in recent decades. Fuel cells (FCs) are one of the cleanest energy generators as they deliver electricity at the zero-emission level. This is because water is the only product of electrochemical reactions during their operation. Among several types of fuel cells, the low-temperature proton-exchange membrane fuel cells (PEMFCs) have been adapted in novel FC vehicles such as Chevrolet Equinox, Toyota Mirai, Hyundai Nexo, and Honda Clarity [1]. A PEMFC is a clean and efficient electrochemical device that generates electricity through a chemical reaction between hydrogen and oxygen, with water as the primary byproduct [2]. It consists of a polymer electrolyte membrane that conducts protons and separates the hydrogen and oxygen gases. When hydrogen is supplied to the anode side and oxygen to the cathode side, a

catalyst facilitates the splitting of hydrogen molecules into protons and electrons [3]. The protons pass through the membrane, while the electrons flow through an external circuit, generating electrical power. At the cathode, oxygen, and electrons combine with protons to form water as the waste product [4]. PEMFCs are widely used in various applications, including transportation and stationary power, due to their high efficiency, and low emissions capabilities [2].

The second important electrochemical energy storage (EES) is batteries. In this family of EES, the Li-ion battery is a flagship. However, due to the lithium shortage [5], alternative energizers such as metal-air batteries (MABs)[6,7] such as Na-air, Zn-air, Al-air, and Mg-air are considered [8–10]. MABs can be constructed using transition metals like iron, copper, and cobalt, or main group metals such as aluminum that are abundant and more affordable as compared to lithium [11]. MABs offer several advantages, including high energy density, which enables them to store a significant amount of energy in a compact form, making them ideal for applications where space and weight constraints are crucial, such as electric vehicles [12]. Their scalability and low cost, such as zinc-air batteries, make them an attractive option for large-scale energy storage and grid applications.

FCs and batteries have an undeniable role in zero-emission transportation resulting in the reduction of CO_2 emission. The annual CO_2 emission in 2020 was 35 billion metric tons [13]. To demonstrate the rate of increase in CO_2 emission, in 2000 was about 25 billion metric tons.

In this research project, we focus on electrochemical processes that drive both MABs and FCs. These two EES systems have one similarity, they use the same type of positive electrode (cathode). Furthermore, a cathodic process in both energizers is based

on an electrochemical oxygen reduction reaction (ORR). As such, atmospheric pressure or compressed oxygen permeates into the porous gas diffusion electrode (GDE) and is reduced at the electrocatalyst surface in the presence of electrolyte. The ORR process requires a suitable electrocatalyst to facilitate this reaction. Hence, intensive studies have been carried out to search for the most efficient and cost-effective electrocatalyst to be implemented in cathode for MABs and PEMFCs [14].

Furthermore, water electrolyzers that generate oxygen and hydrogen for the FCs also rely on electrochemical oxygen evolution reaction (OER) and this anodic process requires an OER electrocatalyst. Fabrication of bifunctional electrocatalysts for both ORR and OER processes has been extensively examined in recent years [15]. The results of these studies have indicated unique carbonaceous materials such as Co-N-, Ni-N-, and Fe-N-doped carbons that demonstrated catalytic activities for both ORR and OER - hence the name bifunctional electrocatalysts. It is demonstrated that such heteroatom-doped carbons can have comparable electrochemical activity and stability to the famous and expensive peers made of Pt and Ru [16]. The mechanism of their function will be detailed in the following section of this thesis.

1.2 Electrocatalyst Importance in Energy Conversion Systems

The electrochemical reactions of some species, such as oxygen, hydrogen, methanol, ethanol, nitrogen, and carbon dioxide, need to be accelerated by electrocatalysts coated on the electrode surface [17]. The reduction and evolution of oxygen (O_2) must be expedited in MABs and FCs [18]. The sluggish kinetics of ORR and OER is a challenging situation on the surface of electrodes, which imposes large overpotential and affects the

energy output of fuel cells [19]. The sluggish kinetics are related to the production of hydroxyl groups (OH^-) from oxygen. However, even benchmark catalysts still suffer from sluggish kinetics [20]. Hence, numerous studies have been done to improve ORR and OER performance using electrocatalysts on the electrode surface [21].

1.3 Electrocatalyst Importance in MABs

The MABs have an anode made from pure metal and an external air cathode, typically with an electrolyte (aqueous or aprotic non-aqueous). During the discharging of MABs, a reduction reaction occurs in the air cathode while the metal anode is oxidized. In MABs batteries, metal ions travel from anode to cathode through a liquid electrolyte, and these ions undergo chemical reactions at both the battery's anode and its cathode. Oxygen can penetrate the porous structure of the cathode in metal-air batteries and be reduced to hydroxyl groups. This electrochemical reaction has been known as the ORR. Despite their early start and great potential, the development of MABs batteries has been impeded by problems associated with the cathode's electrocatalyst. The reduction of oxygen in the discharging process of MABs[22] and the evolution of oxygen for the rechargeable MABs[23] need appropriate electrocatalysts to facilitate these two reactions [24]. The MABs can not have appropriate electrochemical performance without electrocatalysts for the reduction/evolution of oxygen [25]. Some precious metals like Pt [26], Ru [27], and Pd [28] compounds have the best performance for the oxygen reduction in the MABs[29] but the higher cost of these precious has limited their applications as electrocatalysts. Therefore, low-cost electrocatalysts for the reduction/evolution of oxygen in MABs have been developed.

For example, Zinc-air batteries (ZABs) are considered appropriate MABs. Zinc as a raw material is orders of magnitude more abundant than lithium. The zinc-based batteries are cheaper, less environmentally harmful, and less susceptible to supply-chain issues than lithium [30,31]. ZABs are noted for their high energy densities but low power output capability (<10 mW for hearing aid button cells) due to the inefficiency of oxygen reduction electrocatalysts available. In addition, the development of electrically rechargeable ZABs with an extended cycle life has been troubled by non-uniform zinc dissolution and deposition [32], and the need for more satisfactory bifunctional oxygen electrocatalyst [24]. The following electrochemical reactions (equations 1-4) are the anode and cathode reactions of the ZABs [33].

1) Negative electrode: $Zn + 4OH^- \rightarrow Zn(OH)_4^{2-} + 2e^-$

2) $Zn(OH)_4^{2-} \rightarrow ZnO + H_2O + 2OH^-$

3) Positive electrode: $O_2 + 4e^- + 2H_2O \rightarrow 4OH^-$

4) Overall reaction: $2Zn + O_2 \rightarrow 2ZnO$

A schematic MAB is illustrated in Figure 1. The airflow is absorbed into the porous cathode and the ORR process is performed on the cathode surface. The ORR process has an essential role in the discharging of MABs. Also, MABs must have the OER process to be considered rechargeable batteries.

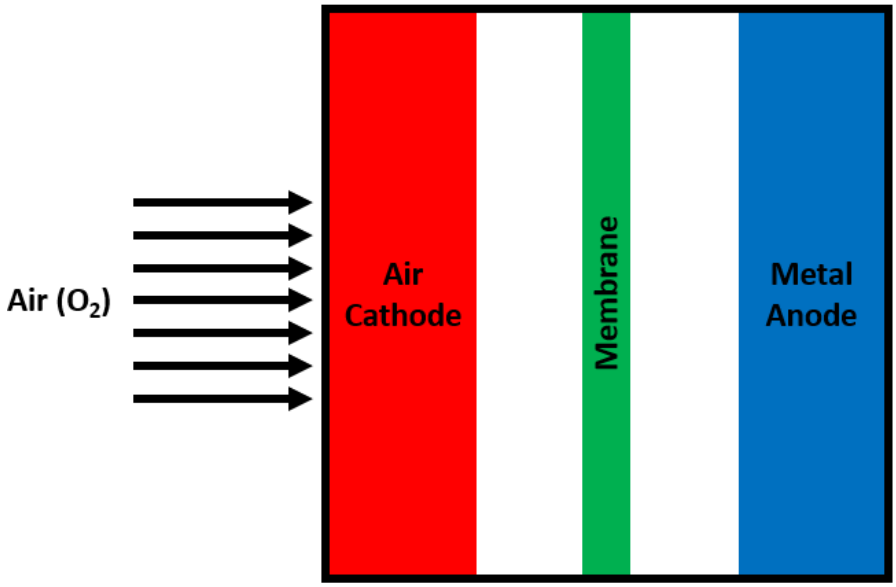

Figure 1: The scheme of a MAB.

1.4 Electrocatalyst Importance in PEMFCs

Also, the PEMFCs as low-temperature fuel cells have ORR in their porous cathode. The following electrochemical reactions are the anode and cathode reactions of the PEMFCs. The sluggish ORR on the cathode precludes the widespread commercialization of PEMFCs [34], which makes the active electrocatalysts indispensable for enhanced ORR performance [35]. The Pt-based electrocatalysts have been used as ORR electrocatalysts in PEMFCs [2,34]. However, the higher price of those Pt-based compounds led to develop the low-cost ORR electrocatalysts such as transition metal-based[36] and carbon-based[37] electrocatalysts for PEMFCs. The lower cost and higher ORR performance are two crucial parameters in developing ORR electrocatalysts for the PEMFCs [38]. The following electrochemical reactions (equations 5-7) are the anode and cathode reactions of the PEMFCs [39].

5) Negative electrode: $\frac{1}{2}O_2 + 2H^+ + 2e^- \rightarrow H_2O$

6) Positive electrode: $H_2 \rightarrow 2H^+ + 2e^-$

7) Overall reaction: $\frac{1}{2} O_2 + H_2 \rightarrow H_2O$

The schematic structure of a PEMFC is illustrated in Figure 2.

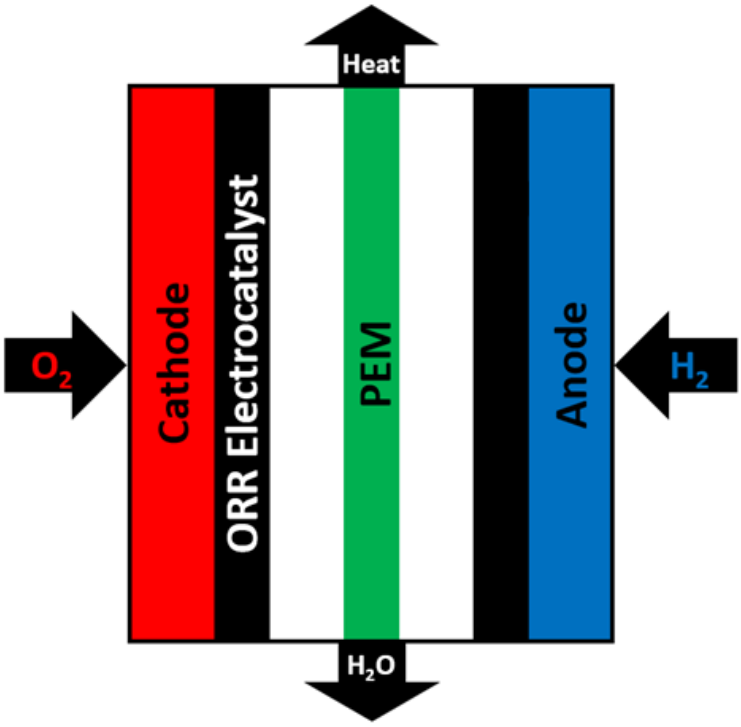

Figure 2: The scheme of a PEMFC.

Oxygen is reacted with hydrogen to produce water. This reaction is exothermic and produces energy. The produced energy can be used for different applications, like the driving force of vehicles. PEMFCs, like MABs, need high-performance ORR electrocatalysts.

1.5 Electrocatalyst Properties

Generally, the ideal electrocatalysts should meet the following parameters: activity, conductivity, stability, selectivity, and low cost [40].

(I) Activity; The catalyst activity is related to the intrinsic catalytic active site type and the number of active sites. First, heteroatom doping (metal atoms, N, O, S, P, and B) and defect control (vacancy and/or edge) generate charge redistribution and change the electronic structure. Each of these modifications can improve the electrochemical activity of the electrocatalysts [41]. The heteroatom doping improves the electrocatalytic activity by generating polar bonds in the carbon structure. These polar bonds improve the attachment of reactant species like O_2 to the electrocatalyst surface [42]. The heteroatom doping reduces O_2 adsorption energy on the electrocatalyst surface and improves the intrinsic electrocatalytic activity. Second, porous structure control (including nanopores, micropores, mesopores, and macropores) increases the exposed number of active sites on the electrocatalyst surface. The mesopores and micropores contribute to larger specific surface areas to improve the reactant's accessibility to the active centers, while the macropores provide more mass transfer pathways [43].

(II) Conductivity; The higher conductivity has a significant role in electron transport in electrocatalytic processes. For example, π-conjugated conductive structures from sp^2 carbon structures lead to swift charge transport in redox reactions enhancing electrocatalytic activity.

(III) Stability; The ideal catalyst must have excellent chemical and structural stability in the harsh alkali/acidic media. Due to the increasing particle size, the particle's agglomeration, and the change of oxidation state on the surface of the electrocatalyst during the long-term operation of a battery, the electrocatalyst will gradually be consumed and partially inactivate, which will lead to the decay of the battery and

PEMFC performance. Therefore, electrocatalyst durability is an essential parameter for the batteries' commercialization.

(IV) Selectivity; The ideal electrocatalysts should have high selectivity towards specific processes. For example, O_2 can be transformed to hydrogen peroxide (H_2O_2) by $2e^-$, or electrochemically reduced to water (H_2O) by $4e^-$. The electrochemical reduction to water is preferred in the fuel cell reaction to maximize the energy conversion efficiency, while the $2e^-$ pathway is a green synthesis method of H_2O_2. Therefore, the electrocatalyst selectivity can effectively regulate the reaction pathway and ORR products.

(V) Environmentally friendly Noble metal (e.g., Pt, Ru, Ir, etc.) electrocatalysts possess high catalytic activity. Still, the shortcomings of high cost, low stability, and resource scarcity seriously restrict their applications. Metal-organic framework (MOF)-based electrocatalysts, metal-free-based carbon electrocatalysts, or transition metal-based electrocatalysts have been developed as future electrocatalyst designs due to intrinsic catalytic activity and low cost. Thus, the design and fabrication of electrocatalysts should follow the principles of low cost, low energy consumption, and low pollution [40].

Overpotential (η) is a significant parameter to evaluate the electrocatalyst performance [44]. Ideally, the applied potential for driving a reaction should equal the reaction potential at equilibrium. In most cases, overpotential, the difference between the applied potential to deliver a certain current density and the thermodynamic potential value, is selected as the primary parameter to evaluate the activity of an electrocatalyst [44]. The applied potential is much higher than at equilibrium to overcome the electrode kinetic reaction barrier. According to the Nernst equation, the applied potential can be calculated by equation 8:

8) $$E=E^0+\frac{RT}{nF}\ln\left(\frac{C_O}{C_R}\right)$$

E^0 is the formal potential of the overall reaction, and E is the applied potential. R is the universal gas constant, T is absolute temperature, n is the number of transferred electrons in the reaction, F is the Faraday constant, and C_O and C_R are the oxidized and reduced materials concentrations, respectively [45].

The overpotential (η), as illustrated in equation 9, is a difference between the applied potential (E) and potential under equilibrium conditions (E_{eq}).

9) $\eta = E - E_{eq}$

The overpotential (η) is commonly referred to as a value that has to be applied to achieve a specified current density, and a lower overpotential of an electrocatalyst in the system indicates its superior electrocatalytic activity for the specific reaction [46]. Reaction overpotential can be reduced with the use of electrocatalysts [47]. The electrochemical reaction rate and related current density are dictated by the electrocatalyst kinetics and substrate concentration [48].

1.6 Oxygen Reduction Reaction

The ORR is a core reaction for EES devices such as MABs and FCs. The ORR performance on the cathode surface of the MABs and PEMFCs needs an active ORR electrocatalyst to expedite the ORR process. The ORR at the cathode of the MABs and PEMFCs involves four steps: first, O_2 diffusion and adsorption at the electrocatalyst surface; second, transport of electrons from anode to adsorbed oxygen; third, splitting of O=O binding; and fourth, OH^- ions removal [21]. There are two ORR pathways, an efficient one-step $4e^-$ pathway, or a sluggish two-step $2e^-$ pathway to reduce oxygen

molecules to OH^- ions. For direct one-step $4e^-$ pathway, their reactions in alkaline solution (equation 10):

10) $O_2 + 2H_2O + 4e^- \rightarrow 4OH^-$.

For indirect two-steps $2e^-$ oxygen reduction, their reactions in alkaline solution (equation 11):

11) $O_2 + 2e^- + H_2O \rightarrow OH^- + HO_2^-$, and $H_2O + 2e^- + HO_2^- \rightarrow 3OH^-$.

The $4e^-$ pathway typically occurs on noble metals, while the $2e^-$ pathway occurs predominantly on carbon materials [21,49].

1.7 Linear Sweep Voltammetry

Linear sweep voltammetry (LSV) is a voltammetric method where the current at a working electrode is measured while the potential between a reference electrode and a working electrode is swept linearly in time. For the purpose of this thesis, the LSV curves determine the onset potential (E_{onset}) of the ORR reaction and half-wave potential ($E_{\frac{1}{2}}$) of the ORR reaction. E_{onset} is the potential at which the ORR starts, $E_{\frac{1}{2}}$ is the potential for half the limiting current value. limiting current density (I_{lim}) indicates the maximum diffusion current density in ORR during RDE measurement, which should be a fixed value in theory for a $4e^-$ ORR in a particular concentration solution and at a certain rotation speed. However, in experiments, I_{lim} is always variable and smaller than the theoretical value even though with the same electrocatalyst, electrode, and rotator [50]. The electrocatalyst loading and O_2 inlet condition (smaller O_2 bubbles in electrolyte increase the I_{lim}value) are the key factors influencing the I_{lim} of ORR [50].

Usually, the LSV curve is intuitively S-shaped [51]. The LSV curves for ORR have three main regions: kinetic-controlled, diffusion-controlled, and kinetic-diffusion mixed

regions [52]. These three regions are illustrated in Figure 3. The ORR electrocatalysts evaluation is usually based on the ORR LSV curves, which generally displays three areas in the potential range [53].

Specifically, in the high-potential area, the overpotential is insufficient to cross the reaction barrier to effect substantial electrochemical reactions. Therefore, within such a potential range, the surface reaction kinetics serves as the limiting factor on overall electrocatalytic performance, which is called the surface kinetic-controlled region. In the low-potential region, the potential deviates far enough from the equilibrium potential. The reaction rate of dissolved oxygen on the electrode is so fast that the dissolution and diffusion of oxygen become the limitation and the current remains almost unchanged with increased overpotential, this is thus called the diffusion-controlled region. Between these two regions, ORR is co-dominated by surface reaction and mass diffusion called the mixed controlled region. The half-wave potential ($E_{\frac{1}{2}}$) in the mixed controlled region is generally employed to evaluate the activity of the electrocatalyst and therefore simultaneously reflects the coupling behavior of surface reaction and mass diffusion [51].

The higher E_{onset} and $E_{\frac{1}{2}}$ (more positive) mean the electrocatalyst is more active. The inflection point of the LSV diagram is $E_{\frac{1}{2}}$.

The ORR has been evaluated by LSV analysis through a rotating disc electrode (RDE). The RDE is a hydrodynamic electroanalytical method used to control the diffusion layer thickness. The RDE is an electrode used to analyze redox reactions and measure their kinetic parameters. Using an RDE, the steady-state mass transport regime can be obtained, for which the reaction extent depends on the rotation rate of the electrode [54]. The RDE has been used to study ORR electrocatalysts, which requires understanding the

combined effects of mass transport (i.e., how fast does oxygen transport to the disk electrode?) and fundamental kinetics (i.e., how quickly is the oxygen reduced once it reaches the electrode?). The hydrodynamic RDE has the advantage of more significant mass transport rates than the rates at stationary electrodes at the electrode surface, which facilitates the charge-transfer kinetics study even in the presence of mass transport limitation. The RDE consists of a disk-shaped electrode material (usually glassy carbon) fashioned and covered by an inert insulating polymer such as Polytetrafluoroethylene (PTFE) or Polyether ether ketone (PEEK).

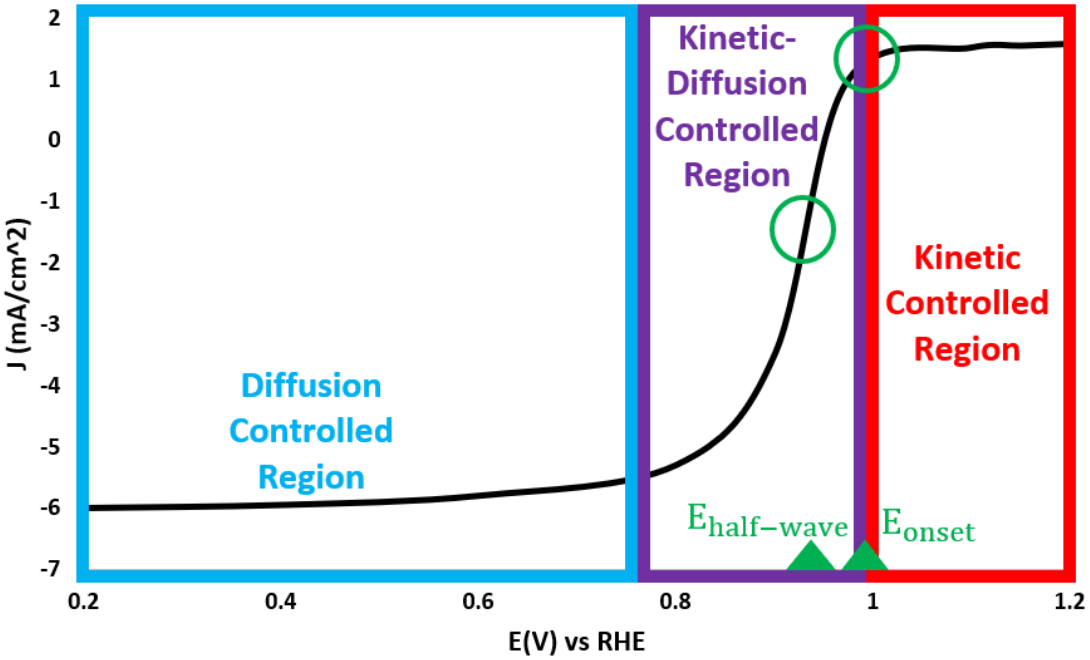

Figure 3. Scheme of different oxygen reduction regions in a typical LSV curve.

1.8 ORR Electrocatalysts

Nowadays, several reported electrocatalysts have approached the diffusion-limited region with a much lower overpotential. It means the activity of the novel electrocatalysts has been improved. ORR catalysts have been limited to Pt, which meets the requirements of

high activity and durability. Tremendous efforts have been accomplished to prepare a Pt-free ORR electrocatalyst with similar ORR performance. Over the last decade, various materials have been tested as non-Pt catalysts, metal-organic structures, and metal-free electrocatalysts. The metal-doped carbons have been widely developed to replace Pt-based ORR electrocatalysts [42]. Doped-carbon structures have been used as oxygen electrocatalysts in MABs and PEMFCs. Heteroatom doping can provide defect [55] and polar bonds[56] in carbon structure with facilitate ORR reaction on the carbon surface [57]. In particular, nitrogen-doped graphitic carbon materials, including N-doped graphene and N-doped carbon nanotubes, have been extensively studied [42]. Furthermore, doping different transition metals in carbon structures has an amazing influence in improving ORR performance [58]. Both metal-free heteroatom-doped carbon electrocatalysts[59] and metal-based heteroatom-doped carbon electrocatalysts[60] have been developed as ORR electrocatalysts.

There are two adsorption types on the surface of carbon materials based on the computational charge density distribution [61]. One is the bidentate O_2 molecule adsorption (two oxygen atoms coordinating with the electrocatalyst surface) and the other is the end-on O_2 molecule adsorption (one oxygen atom coordinating perpendicularly to the surface) [62]. The latest research results about the reaction mechanism on N-doped carbon materials demonstrated that carbon atoms next to pyridinic N show Lewis basicity. The oxygen molecule is first adsorbed at such carbon atoms, followed by protonation of the adsorbed O_2 [61].

The ORR pathways can be analyzed by H_2O_2 formation as an intermediate by using rotating ring disc electrodes (RRDE). The critical point in RRDE is understanding that

the ORR products (hydroxides and peroxides) generated at the disk must subsequently transport past the ring electrode. The difference between an RDE and an RRDE is the addition of a second ring-shaped working electrode around the central RDE as the first working electrode [63]. Furthermore, the disk generates (produces) the products, and the ring collects (detects) the products. This generator-collector geometry allows direct detection of any peroxide formed by the electrocatalyst.

In the LSV analysis, the electron transfer coefficient of ORR can be calculated by fitting the Koutecky-Levich (K-L) equation to elaborate the reaction pathway [63]. Equation 12 is the K-L equation in which i_m is the measured current (A), i_k is the kinetic current (A) from the electrochemical reactions, B_L is the Levich constant, and ω is the angular rotation rate of the electrode (rad/s).

12) $\frac{1}{i_m} = \frac{1}{i_k} + \frac{1}{B_L \omega^{0.5}} \Rightarrow \frac{1}{i_m} = \frac{1}{i_k} + (\frac{1}{B_L})\ \omega^{-0.5}$

B_L can be calculated by the K-L equation. Plotting of the K-L plot using i_m^{-1} as Y-axis and $\omega^{-0.5}$ as X-axis provides $\frac{1}{B_L}$ as slop and $\frac{1}{i_k}$ as intercept. Hence, B_L can be calculated by K-L plot. Also, $B_L$can be defined by equation 13:

13) $B_L = 0.62\ n\ F\ A\ D^{\frac{2}{3}}\ \upsilon^{\frac{-1}{6}}\ C$

F is the Faraday constant (C/mol), n is the number of moles of electrons transferred in the half-reaction, A is the electrode area (cm^2), D is the diffusion coefficient ($\frac{cm^2}{s}$), υ is the kinematic viscosity ($\frac{cm^2}{s}$), and C is the analyte concentration ($\frac{mol}{cm^3}$). Therefore, n is the number of transferred electrons that can be determined. The leading term 0.62 is from the calculation of the velocity profile near the surface of electrode [64]. Usually, n is a number between two and four. Equation 14 can calculate the n to determine the ORR pathway:

$$14)\ \frac{1}{i_m} = \frac{1}{i_k} + \left(\frac{1}{0.62\ n\ F\ A\ D^{\frac{2}{3}}\ \upsilon^{\frac{-1}{6}}\ C}\right)\omega^{-0.5}$$

$$\Rightarrow \left(\frac{1}{0.62\ n\ F\ A\ D^{\frac{2}{3}}\ \upsilon^{\frac{-1}{6}}\ C}\right)\omega^{-0.5} = \frac{1}{i_m} - \frac{1}{i_k} \Rightarrow 0.62\ n\ F\ A\ D^{\frac{2}{3}}\ \upsilon^{\frac{-1}{6}}\ C = \omega^{0.5}\left(\frac{1}{i_m} - \frac{1}{i_k}\right)$$

$$\Rightarrow n = \frac{\left(\omega^{0.5}\left(\frac{1}{i_m} - \frac{1}{i_k}\right)\right)}{0.62\ F\ A\ D^{\frac{2}{3}}\ \upsilon^{\frac{-1}{6}}\ C}$$

If n is closer to two, it means the ORR mechanism is more like the two-electron pathway. Also, if n is more comparable to four, it means the ORR mechanism is more like the four-electron pathway.

It has become common practice to estimate the numbers of electrons (n, eq mol^{-1}) transferred in faradaic reactions at rotated disk electrodes from the slope of plots of reciprocal current ($\frac{1}{I}$) vs. reciprocal square root of rotational velocity ($\frac{1}{\omega^{\frac{1}{2}}}$) [65]. This practice is based on the K-L equation derived for a one-step electron-transfer mechanism. Furthermore, the intercept of the K-L plot is assumed to be a reciprocal function of the heterogeneous rate constant (k_h, cm s^{-1}) for the electron-transfer process [65]. The Levich calculation is a common analysis performed using an RDE over a range of different rotation rates. For a simple electrochemical system, the reaction rate is controlled only by mass transport to the electrode surface, the overall voltammogram magnitude should increase with the square root of the rotation rates. K-L analysis provides a simple and effective method to extract electrokinetic information by correcting for mass transport effects [45].

The currents measured during a Levich test are plotted against the rotation rate square root in the Levich plot. According to the Levich equation, the limiting current increases linearly with the rotation rate square root (and the plot slope is $0.620nFAD^{2/3}v^{-1/6}C$).

Usually, a set of rotation rates are multiples of perfect squares (such as 100, 400, 900, 1600, and 2500 rpm, etc.) to facilitate plotting the Levich plot [45].

1.9 Oxygen Evolution Reaction

The OER process is the critical reaction to enable solar energy storage in the form of hydrogen fuel through water-splitting. Also, OER is an essential reaction in the recharging of MABs. Earth-abundant, efficient, and durable OER electrocatalysts are required for large-scale, cost-effective solar hydrogen production. While OER electrocatalysts based on metal oxides have promising electrocatalytic activity and stability, their rational design and developments are challenging due to the electrocatalyst's heterogeneous nature. Also, the OER process has immense importance in developing rechargeable MABs. The charging process of the MABs needs a reverse reaction of ORR to produce O_2 from OH^-. One of the most significant problems is that the common MABs are not rechargeable. Tremendous efforts have been made to solve this issue by providing OER in the charging process [66].

OER has two mechanisms: adsorbate evolution (AEM) and lattice oxygen-mediated (LOM) [67,68]. The AEM mechanism can be considered as the redox reactions of metal cations [66]. The AEM usually involves metal ions based on four proton-electron transfer reactions. At each step, a proton is injected into the electrolyte that coalesces with an electron on the cathode [21]. Four following steps (equations 15-18) determine the AEM mechanism through the proton-electron transfer reactions with the metal ion [69].

15) $OH^- + * \rightarrow OH^* + e^-$

16) $OH^* \rightarrow O^* + e^- + H^+$

17) $O^* + OH^- \rightarrow HOO^* + e^-$

18) $HOO^{*} \rightarrow * + O_2 + e^{-} + H^{+}$

The electron-transfer process during the oxygen evolution reaction (OER) often either proceeds solely via a metal redox chemistry (adsorbate evolution mechanism (AEM), with metal bands around the Fermi level) or an oxygen redox chemistry (lattice oxygen-mediated mechanism (LOM), with oxygen bands around the Fermi level). Unlike the AEM, the LOM involves oxygen redox chemistry instead of metal redox, which leads to the formation of a direct oxygen-oxygen (O-O) bond. As a result, such a process can bypass the rate-determining step, that is, O-O bonding, in AEM, which highlights the critical advantage of LOM as compared to conventional AEM. Thus, it has been well reported that LOM-based electrocatalysts can demonstrate higher OER activities as compared to AEM-based electrocatalysts [68].

OH adsorbs on the surface O vacancy site. The adsorbed OH (HO* species) then later experiences deprotonation to form O*. The resulting O-O bond formation step allows O* to react with another OH to generate the HOO* intermediate. Finally, O_2 evolved through the deprotonation of HOO* by restoring the active site. LOM happens on two neighboring metal sites, which differs from common AEM, which proceeds on a single metal site [69].

The OER activity can be improved through the catered geometric structure of the shortened O-O distance (~ 2.6 Å). While the O-O formation through direct coupling between metal cations and lattice anions known as LOM has also been observed in current active transition metal oxide OER electrocatalysts [70]. In general, the kinetics of the LOM is faster than that of the AEM due to the proton-electron transfer processes in

LOM-adopted metal oxides with considerably smaller lattice parameters and shorter surface oxygen separations.

In general, different mechanisms are favored by different electrocatalysts (or by different local crystal plane surfaces in an electrocatalyst) based on the minimization of activation energy. The optimization of active site adsorption capacities is regarded as an appropriate strategy to decrease the surface reaction energy barrier [70]. Usually, the turning point of the OER graph at 10mA.cm^{-2} ($E_{j_{10}}$) is a sample's OER performance. A typical OER graph is illustrated in Figure 4. The OER electrocatalysts have been widely developed to overcome the high OER overpotentials [71]. The lower $E_{j_{10}}$ considered as the higher OER activity. Usually, the OER analysis is performed by RDE electrode [72].

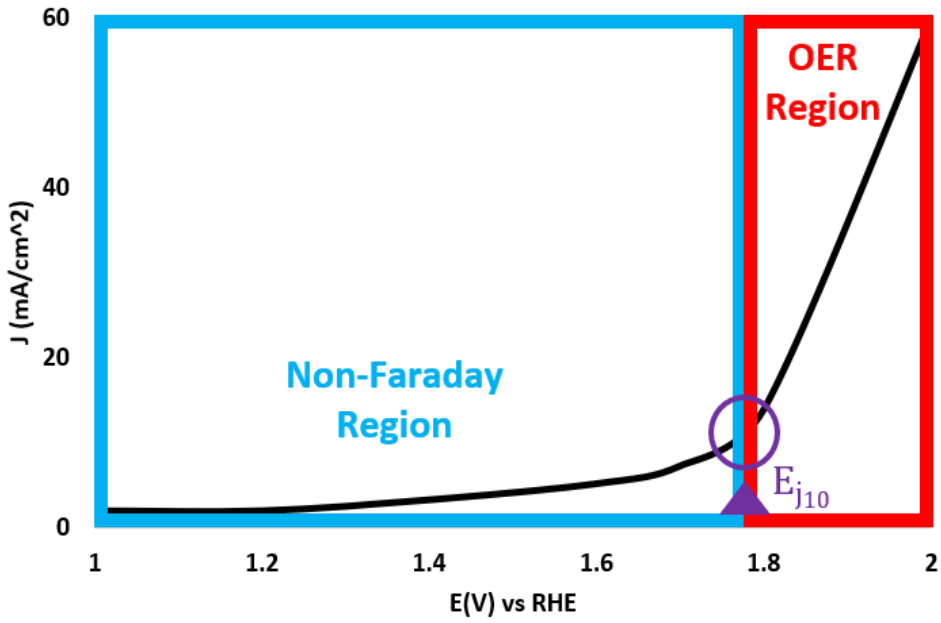

Figure 4: Scheme of oxygen evolution reaction in a typical LSV curve.

1.10 ORR/OER Bifunctional Electrocatalysts

The bifunctional oxygen electrocatalyst (BOE) is an electrocatalyst with considerable electrochemical performance in the reduction and evolution of oxygen for ORR and OER processes. ORR and OER have different procedures. Bifunctional oxygen electrocatalysts are challenging since a suitable OER electrocatalyst is not necessarily a promising ORR electrocatalyst [21]. The air electrodes should be capable of catalyzing both the ORR and OER efficiently to be considered rechargeable metal-air batteries [46]. Developing high-activity and stable BOEs is essential for developing rechargeable MABs [40]. Three main parameters to examine the bifunctional electrocatalyst performance are overpotential, stability, and electrode characteristics [73].

The most common way of measuring an excellent bifunctional electrocatalyst for ORR and OER is by analyzing its overpotential at a given current density and based on the same catalyst loading. Typically, the E_{onset} and $E_{\frac{1}{2}}$ to evaluate ORR and the onset potential and the potential at 10mA.cm^{-2} ($E_{j_{10}}$) to evaluate OER.

Equation 19 determined the bifunctional potential for the bifunctional oxygen electrocatalysts [74]:

19) $\Delta E = E_{j_{10}} - E_{\frac{1}{2}}$

ΔE (Figure 5) has been used to evaluate the activity in the bifunctional electrocatalyst, and it is more indicative than the common overpotential of ORR and OER. A smaller overpotential at a given rate is a good indicator of a promising bifunctional electrocatalyst. Also, it is necessary to fabricate a bifunctional electrocatalyst that is stable enough to withstand harsh environments encountered during ORR and OER while still delivering significant performance. The current studies have reported ΔE values

lower than 0.7V as the current benchmark of the ΔE value for the bifunctional oxygen electrocatalysts [74–76].

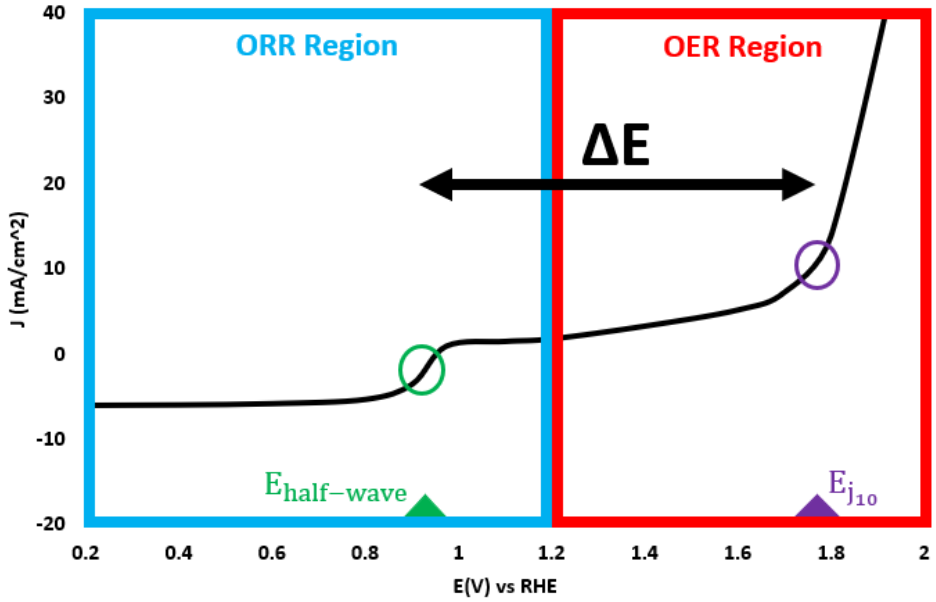

Figure 5: Scheme of bifunctional potential for ORR and OER processes.

The second important parameter is electrocatalyst stability. The electrocatalyst stability is directly related to the cycle life of the MABs. An appropriate bifunctional oxygen electrocatalyst should be durable in harsh alkaline or acidic media. The ΔE value for durable bifunctional oxygen electrocatalysts is stable after long cycles [77].

The last significant parameter is the working electrode characteristics, such as wettability and binding force. The electrocatalyst should have high wettability, which decreases the reactants' separation from electrocatalyst active sites [78]. Also, the electrocatalyst should be firmly attached to the substrate, especially during the OER process, where a large amount of O_2 will be generated. If the electrocatalyst is not firmly bonded to the substrate, it will cause the electrocatalyst to fall off, and the electrode will stop being

active. However, excessive use of the binder can directly affect the wettability and increase the batteries and PEMFCs resistivity.

1.11 Heteroatom-doped Carbon Electrocatalyst

Massive number of studies have evaluated different materials to develop high-performance oxygen electrocatalysts for ORR and OER processes [79–81]. In recent years, tremendous efforts have been accomplished to develop electrocatalyst carbon as the bifunctional electrocatalyst [82]. Carbon materials have always played a significant role in the field of electrocatalysis due to their superior electrical conductivity and high specific surface area. However, the pure carbon material's inherent ORR and OER electrocatalytic performance are poor, mainly affected by the two-electron pathway. The formation of OH* and OOH*, which are the rate-determining steps of OER, require high activation energy during the electrocatalytic process of the graphene-like material, thus increasing the difficulty of OER [83]. Three types of materials have been widely used as oxygen electrocatalysts, including carbon-based materials, carbon-based metal composite materials, and carbon-free materials [73].

Carbon-based oxygen electrocatalysts have three types: metal-free heteroatom doping nanostructured carbons [84], intrinsic defects, and metal-free heteroatom doping combined with intrinsic defects. Metal-free heteroatom doping nanostructured carbons like N-doped [85], P-doped [41,85], S-doped [86], B-doped [87], and dual-doped carbons[88] like N, P co-doped carbons [85] have been used as oxygen electrocatalysts. These heteroatoms have different atomic radii and electronegativity compared to carbon and doping them in carbon materials will form different active sites, resulting in different electronic properties and coordination structures. Multi-atom-doped carbon materials should be used if single

heteroatom doping cannot meet the bifunctional electrocatalyst performance. Hence, co-doped carbon structures have been developed as the bifunctional oxygen electrocatalysts such as S, N co-doped carbon [82], Co, N co-doped carbon [89], Fe, N co-doped carbon [90], P, N co-doped carbon [91], and O, N co-doped carbon electrocatalysts [92].

In addition to heteroatom doping, intrinsic defects in carbon structures have also provided efficient active sites for OER and ORR. Defects can make more unsaturated coordination sites in catalysts, which have more benefits for the adsorption of reaction molecules [93].

Increasing π-conjugation can increase the electrocatalytic activity of the carbon materials [94,95]. Providing intrinsic defects can improve the electrocatalytic performance of carbon-based oxygen electrocatalysts [73].

Metal-free carbon electrocatalysts have appropriate electrocatalytic activity but their stability is very low, especially in corrosive electrolytes like potassium hydroxide (KOH), 6 mol per liter (M). Hence, metal-doped electrocatalysts have been developed primarily to enhance the cycle stability of rechargeable MABs [96]. Carbon-based metal composite oxygen electrocatalysts have three types: graphene-based metal composite materials, MOF-derived materials, and single-atom electrocatalysts. Loading transition metal nanoparticles on graphene materials is an efficient method for preparing electrocatalysts. A single metal cannot meet the bidirectional requirements for both OER and ORR. Therefore, co-doping of two metals can better provide OER and ORR activity than a single atom-doped carbon electrocatalyst. MOFs can form controllable size hollow structures through a combination of metal centers and organic ligands and provide considerable electrocatalytic activity. Finally, a single atom on the graphene surface has significant oxygen electrocatalytic activity due to unsaturated coordination bonds and

maximum atom utilization efficiency. The problem for a single atom is its stability in alkaline media, which needs to be improved in future studies. The metal loading on the graphene surface should be lower than 1% to fabricate the single-atom electrocatalysts and prevent particle generation. Therefore, synthesizing diatomic and even polyatomic electrocatalysts can increase the active site density and improve the bifunctional activity.

Also, carbon-free oxygen electrocatalysts including spinel-type oxides (AB_2O_4 [A, B represent divalent and trivalent ions, respectively, such as $Mn_xCo_{3-x}O_4$ and $Ni_xCo_{3-x}O_4$]), perovskite oxides (ABO_3) like $LaMnO_3$ and $LaBO_3$, and layered double hydroxides [97] have been developed as carbon-free oxygen electrocatalysts [73]. The layered double hydroxides have a two-dimensional structure consisting of the primary layer and anions and water molecules between the layers.

1.12 Metal-Organic Frameworks-based Electrocatalyst

The carbon-based electrocatalysts for ORR and OER processes have been extensively examined in recent years [98]. For example, a bifunctional ORR/OER electrocatalyst was reported in 2022 that was fabricated from nitrogen-doped carbon encapsulated Co-$Co_6Mo_6C_2$ nano polyhedron using ZIF-67 (CoZIF) as a precursor [16] or another bifunctional ORR/OER electrocatalyst was made in 2019, through pyrolysis of graphene oxide supported CoZIF under a nitrogen atmosphere [99]. Another study in 2021 reported ZIF-67 derived carbon nanotubes coated nitrogen-doped CoNi alloy nanocomposites as a bifunctional ORR/OER electrocatalyst [96].

The existence of metal in the carbon structure can improve the electrochemical performance of carbon materials as oxygen electrocatalysts. To enhance these electrocatalysts' bifunctional activity and stability, doped-carbon composite catalysts

have been explored [100]. MOFs have been fabricated through a reaction of metal ions and organic ligands. Also, ZIFs, as a subcategory of MOFs, have imidazole as an organic linker. The carbonization (pyrolysis) of MOFs and ZIFs can provide oxygen electrocatalysts for ORR and OER. The advantage of ZIFs over MOFs is the existence of nitrogen in the ZIFs structure. Doped nitrogen in the carbon structure improves the electrocatalytic activity of ZIF-based electrocatalysts. The carbonization of MOFs and ZIFs provides a carbon structure by doping metals and nitrogen [101].

Different carbon structures such as two-dimensional, core-shell, and hollow-core have been prepared as oxygen electrocatalysts [101]. These special structures can increase the specific surface area of electrocatalysts. Doped carbons (especially from ZIFs) have been widely used as ORR, OER, and bifunctional ORR/OER [60,102] electrocatalysts. Hence, porous nitrogen and metal-doped carbon alternate to common precious metals like Pt (for ORR) and Ru (for OER). Also, the electrochemical analyses determined the appropriate stability of the doped carbon (primarily N-doped carbon [103]) as oxygen electrocatalysts [104]. The research projects are ongoing to improve the electrochemical performance of the doped carbon structures as ORR and OER electrocatalysts.

1.12.1 Metal-Organic Frameworks

MOFs have been widely developed in recent years. are assembled by interconnection of inorganic metal nodes with organic ligands [105]. For example, HKUST MOF was fabricated in 1991 through a reaction of copper(II) nitrate trihydrate with benzene-1,3,5-tricarboxylic acid in an aqueous solution of 50:50 H_2O:ethanol at 180°C for 12 hours in a Teflon-lined 23-ml Parr pressure vessel [106]. The HKUST framework comprises dimeric cupric tetracarboxylate units with a short Cu-Cu internuclear separation.

The carbon derived from MOFs has been used to prepare electrocatalysts [107]. For example, polyaniline-coated MOF has been prepared as an electrocatalyst for ORR reaction [108]. MOFs have two advantages for electrocatalyst precursors: porosity and metal-carbon bonds. The MOFs can be fabricated in an autoclave through a hydrothermal reaction [109,110]. MOFs have been used to prepare heteroatom-doped carbon-based electrocatalysts for ORR and OER [111]. The pyrolysis of MOFs can provide heteroatom-doped carbon structures that can be used as oxygen electrocatalysts. The pyrolyzed MOFs have high porosity because of the higher porosity of MOFs [112].

1.12.2 Zeolitic Imidazolate Frameworks

The ZIF is a branch of MOFs with imidazole as an organic linker in their structure [113]. Like MOFs, ZIFs have been prepared by reacting 2-methylimidazole and metal compounds such as cobalt (II) nitrate hexahydrate. For example, ZIF-67 has been fabricated through the aqueous reaction of 2-methylimidazole and cobalt (II) nitrate hexahydrate at room temperature for 24 hours [114]. The carbon materials derived from ZIFs have been widely used to fabricate electrocatalysts [115].

The advantage of ZIFs over MOFs is the existence of nitrogen in the ZIFs structure for fabricating electrocatalysts. The number of publications that used ZIFs as a precursor of heteroatom-doped carbon-based electrocatalysts is far more extensive than the MOFs studies. 2-methylimidazole (MIM), as a nitrogen source in ZIFs, provides an N-doped structure that improves ORR and OER performance [116]. MIM has been widely used to prepare ZIFs. Most studies prepared ZIFs in a media like dry non-polar, aprotic polar, and protic polar (like aqueous) [117,118] solvents [119,120]. The solvent-free synthesis as a novel method of preparing MOFs and ZIFs has been developed recently. First, Stuart L. James'

research group reported the solvent-free synthesis of a porous MOF by grinding and heating isonicotinic acid and copper (II) acetate [121]. Then, several articles reported ZIF preparation by melting metal oxides like ZnO [122] or CoO [123] and mixing with MIM to provide ZIFs. The articles that reported the solvent-free synthesis of ZIFs used temperatures higher than 100˚C, and the reaction time was about 2-5 hours [122,124,125]. In this research, we used metal nitrates instead of metal oxides which helps to reduce the reaction temperature for the ZIF formation process.

1.13 Project Novelties

In this project, different MOFs and ZIFs were pyrolyzed by a tube furnace to fabricate carbons as ORR and OER electrocatalysts. The first novelty of this project is to prepare ZIFs by a modified solvent-free method that is faster and easier than the current solvent-free synthesis method. This project's second important novelty is fabricating a hybrid carbon structure containing cobalt and iron. Previous studies have reported F-doped carbon ORR electrocatalyst [126] and Co-doped carbon ORR electrocatalyst [127].

In this study, we reported a novel hybrid C, Fe, N-doped electrocatalyst. This hybrid triple-doped structure has considerable ORR and OER performances and cyclic stability that can compete with current standard ORR/OER electrocatalysts like platinum (for ORR) and ruthenium (for OER).

The current price for one kilogram of platinum in September 2023 is about 34000 USD, while the cost to produce one-kilogram hybrid ZIF from cobalt nitrate, iron nitrate, and 2-methylimidazole in September 2023 is about 500 USD, and the total production costs for one-kilogram carbon for the mentioned ZIF (with 50 percent pyrolysis efficiency) in September 2023 is about 1000 USD. It determined that ZIF-based carbons' production

costs are much cheaper (3% of Pt price) than common precious metal-based electrocatalysts. Furthermore, the electrochemical properties of the prepared samples from ZIFs have determined their considerable potential as ORR and OER electrocatalysts [128].

2.0 Experimental

2.1. Materials

All materials for synthesizing HKUST MOF and Polypyrrole (PPy) are listed in Table 1. Also, deionized water (DI) is used to prepare HKUST MOF.

Table 1. Chemical substances and suppliers.

Chemical substance	Company	Cas number
Anhydrous ethanol	Merck-Millipore	64-17-5
1,3,5-Benzenetricarboxylic acid	Tokyo Chemical Industries	554-95-0
2-Methylimidazole	Millipore-Sigma	693-98-1
Copper (II) nitrate pentahydrate ($Cu((NO_3)_2) \times 5\ H_2O$)	Millipore-Sigma	19004-19-4
Cobalt (II) nitrate hexahydrate ($Co((NO_3)_2) \times 6\ H_2O$)	Millipore-Sigma	10026-22-9
Hexane	Millipore-Sigma	110-54-3
Iron (III) nitrate nonahydrate ($Fe((NO_3)_3) \times 9\ H_2O$)	Millipore-Sigma	7782-61-8
Iodine	Merck-Millipore	7553-56-2
Pyrrole	Millipore-Sigma	109-97-7

2.2 Synthesis of HKUST MOF

The HKUST MOF has been prepared through the hydrothermal chemical reaction of CuN and BTC. In a typical method, first, CuN was dissolved into 5 mL DI water. It was

followed by the addition of BTC in 5 mL of ethanol. Both mixtures were mixed thoroughly by stirred magnet for 30 minutes until completely dissolved. The resultant solutions were transferred into a 25 mL Teflon-lined stainless-steel autoclave [129]. It was kept at 120 °C for 72 hours in the oven. Then the autoclave was cooled down to room temperature [130]. The blue crystals were isolated by filtration. The suspension was washed three times with ethanol and dried. The color of the synthesized HKUST MOF is light blue. The product is stored in the oven for 12 hours. Then MOF color changed to dark blue [130]. HKUST MOF can absorb water. The drying process removes moisture in the MOF structure. The MOF was kept in a vial, and the air was replaced by N_2 to prevent any humidity absorption. Figure 6 illustrates the schematic synthesis of HKUST MOF.

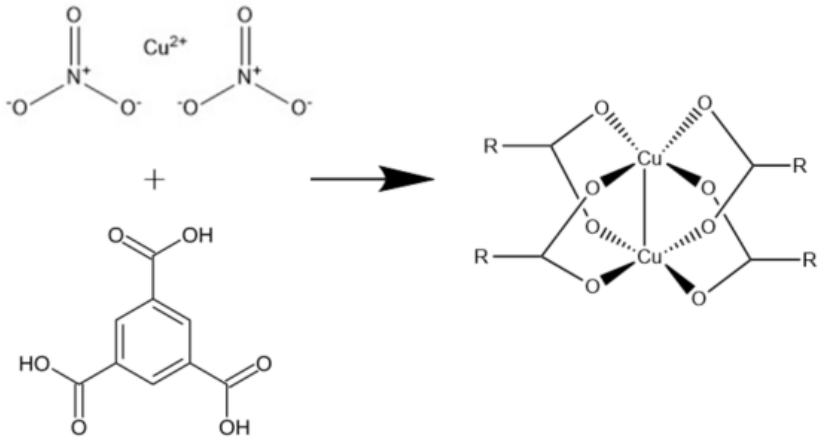

Figure 6. Scheme of the synthesis of HKUST MOF through the aqueous reaction of CuN and BTC.

2.3 Synthesis of Polypyrrole

As a highly active monomer, the pyrrole monomer must be distilled before polymerization. Pyrrole monomer is colorless, but two pyrrole monomers can react and produce pyrrole dimer. This self-polymerization can continue to produce trimer, tetramer,

and higher PPy chains. The self-polymerization changes the pyrrole color to light yellow. Also, longer PPy chains change their color to dark brown. O_2 and temperature can increase the pyrrole self-polymerization. Therefore, pyrrole must be stored in a refrigerator under an inert gas such as nitrogen [130].

First, pyrrole must be purified through a distillation process. Then, distilled colorless pyrrole monomers can be used for polymerization. There are two types of initiators for the radical polymerization process. The first group is the thermal initiators, such as benzoyl peroxide, ammonium persulphate, and potassium persulphate. The high temperature of about 80 to 100˚C leads to the symmetrical breaking of a bond in these thermal ignitors, which produces two radicals. The active radical at the high temperature starts to react with other monomers considered the propagation step in polymerization. Thermal initiators are considered fast initiators. Another type of polymerization initiator reacts slower than the thermal initiators. The second group of radical initiators is the redox initiator. The redox initiators are reacted at lower temperatures, 0 to 30˚C, which produce one anion and one radical initiator. For two reasons, thermal initiators' polymerization reaction is faster than redox initiators. First, the thermal initiators produce two radicals, while the redox initiators produce one. Therefore, the thermal initiators have more opportunity to start polymerization than the redox initiators. Second, the thermal initiators are active at higher than 70˚C. The higher temperature means the higher motion of all components in the system. Hence, a more significant number of radicals and more molecular movement due to an increase in the activity of the thermal initiators than the redox initiators.

2.4 Preparation of PPy-coated HKUST MOF

The PPy particles should slowly sediment and permeate in MOF pores. Therefore, the coating process of HKUST MOF by PPy has been performed using redox initiators at 5˚C in the fridge. First, monomer distillation was performed to produce pure pyrrole monomers. Then, the colorless pure pyrrole was added to dried HKUST MOF in a vial to cover the HKUST MOF surface. This mixture was kept in the fridge for 12 hours to let pyrrole monomers penetrate inside the HKUST MOF pores [131]. Finally, iodine/hexane solution as an initiator was added to the mixture of pyrrole and HKUST MOF. The vial was kept in the fridge for three days. Finally, the coated MOF was washed with hexane to remove extra and non-attached PPy particles. PPy-coated HKUST MOF was characterized by attenuated total reflection infrared spectroscopy (ATR-IR), X-ray diffraction (XRD), X-ray photoelectron spectroscopy (XPS), and scanning electron microscopy (SEM) to determine the functional groups and structure. The results will be presented in the next sections.

2.5 Preparation of CoZIF and FeZIF

In this project, ZIFs have been prepared by a solvent-free method. Usually, MOFs and ZIFs have been fabricated in a media [132]. Stuart James' research group reported the first solvent-free synthesis of ZIFs in 2006 [121]. They mixed copper acetate monohydrate with isonicotinic acid with a ball mill. Then the ground mixture was heated at 200˚C for three hours. It was the first solvent-free mechanochemical ball-milling method for synthesizing MOFs and ZIFs. Afterward, several studies have been reported on the solvent-free synthesis of MOFs and ZIFs. All these reports need time (between one to five hours) and temperature (between 150-300˚C) to complete the solvent-free synthesis. One of the

essential advantages of the current project is to design a novel synthesis method that provides ZIFs at lower times and temperatures. The metal nitrates, including cobalt (II) nitrate nonahydrate (CoN) and iron (III) nitrate nonahydrate (FeN), were melted at 90˚C. Afterward, 2-methylimidazole (MIM) was added to them to prepare ZIFs. This process is significantly faster than conventional solvent-free ZIF synthesis because metal nitrates replaced metal oxides. Metal nitrates have more activity to react with MIM than metal oxides. Therefore, ZIF synthesis by metal nitrates needs less energy and time than metal oxides. The molar ratio (metal nitrate:MIM) is (1:2). This synthesis method has some significant advantages, such as a fast process and lower (safer) temperature. For the synthesis of CoZIF, CoN (1 mol) was melted in a vial at 90˚C. Then MIM (2 mol) was added to the vial and vigorously mixed for a few seconds. The color of CoN (dark red) was changed immediately to purple. According to previous studies, CoZIF (ZIF-67) has a purple color [133,134]. Also, FeZIF is fabricated like CoZIF. FeN (1 mol) was melted in a vial at 90˚C, and then MIM (2 mol) was added. The mixture was mixed vigorously for a few seconds. The color of melted FeN is pink, and it turned brown after adding MIM. Co-FeZIF was prepared by mixing CoN (0.5 mol) and FeN (0.5 mol). The mixed nitrates (CoN and FeN) were melted at 90˚C. Then, MIM (2 mol) was added to the melted mixture and mixed vigorously for a few seconds. Three prepared samples are named CoZIF, FeZIF, and Co-FeZIF respectively. Figure 7 illustrates the schematic synthesis of CoZIF (ZIF-67). The ZIFs were characterized by ATR-IR, XRD, EDX, and SEM to determine the functional groups and structure. The results will be presented in the next sections.

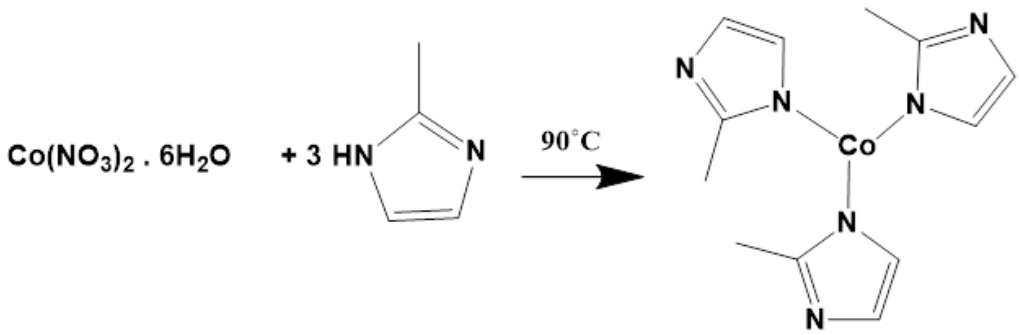

Figure 7: Scheme of the solvent-free synthesis of CoZIF (ZIF-67).

2.6 ZIFs Purification

The prepared ZIFs were washed to remove any probable impurities before characterizations [125]. The prepared ZIFs were washed with methanol three times. The washed ZIFs were dried in an oven at 80˚C for 12 hours. The effect of purification on ZIFs was analyzed by XRD which reported in the next sections.

2.7 Pyrolysis

The samples including MOFs and ZIFs were pyrolyzed in the tube furnace under N_2 inert gas. The pyrolysis process was performed by a tube furnace from Thermo Scientific model Lindberg Blue M (Figure 8). N_2 inert gas protects samples in a crucible in a ceramic tube against oxidation. Different temperatures (600, 700, 800, 900, and 1000˚C) were used to determine the effect of temperature on the pyrolysis process. The heating process has three steps including a heating ramp (in 1.5 hours), constant heating (in 2.0 Hours), and cooling (in 6 hours). The heating process was constant for all samples, and only the highest temperature was altered to evaluate the influence of the temperature on the pyrolysis. For example, for 900˚C: 25-900˚C (1.5 hours), 900-900˚C (2.0 hours), and 900-25˚C (6.0 hours). The influence of the pyrolysis process on PPy-coated HKUST MOF was analyzed by ATR-IR, XRD, and XPS to determine the functional groups and

structure. The results will be presented in the next sections. Also, the influence of the pyrolysis process on ZIFs was analyzed by ATR-IR, XRD, and EDX to determine the functional groups and structure. The results will be presented in the next sections.

Increasing the carbonization temperature can increase the porosity of the carbon-based samples. But in higher temperatures like 1000˚C, the nanopores can be destroyed and the porosity will be reduced [135]. Hence, thermal optimization has a considerable importance to enhance the porosity of the carbon-based precursors [136,137].

Figure 8: Tube furnace for the pyrolysis process.

2.8 Purification of the Samples

First, the pyrolyzed samples were ground by mortar to increase the surfaced area and remove any aggregations. Then, the pyrolyzed ZIFs washed with HCl (2M) for 2 hours at 70˚C. This process removes any impurities, such as metal and metal oxides. The solid

part was separated by vacuum filtration and dried in an oven for 12 hours at 60˚C. The resulting fine black powder can be used for electrochemical analyses.

2.9 Samples Characterization Methods

First, MOFs and ZIFs samples were tested by ATR-IR to determine the functional groups. ATR-IR is a facile and fast method to determine the functional groups of the samples. ATR-IR is a sampling technique used in conjunction with infrared spectroscopy which enables samples to be examined directly in the solid or liquid state without further preparation. Spectroscopy is the branch of science concerned with the investigation and measurement of spectra produced when matter interacts with or emits electromagnetic radiation [138]. Spectroscopic characterization is the process of utilizing spectroscopy to investigate and understand the properties of a material or substance. These techniques involve analyzing the interaction between the material and electromagnetic radiation (such as light, X-rays, or radio waves) to extract information about its composition, structure, and behavior [139]. The ATR-IR device was Bruker Alpha II (Figure 9). ATR-IR is a sampling technique used in conjunction with FTIR. ATR technique is widely used for solid samples without preparing a KBr pellet. All samples were powder, and ATR-IR detected each sample (powders) to determine the functional groups of the samples. Second, XRD is a rapid and non-destructive analytical technique primarily used for phase identification of a crystalline material and can provide information on unit cell dimensions. XRD is a scattering method that uses X-rays to investigate the atomic and molecular structure of materials [140]. When X-rays interact with a crystalline sample, they scatter off the regularly spaced atomic planes within the crystal lattice [140]. This scattering results in a diffraction pattern of constructive and destructive interference, which is

recorded as a series of diffraction peaks on a detector [140]. The analyzed material is finely ground, and homogenized, and average bulk composition is determined. MOFs and ZIFs samples were tested by a XRD device to evaluate their structure's crystallinity and functional groups. The device model of XRD is Bruker AXS D8 XRD. Third, XPS is a spectroscopic technique based on the photoelectric effect[141] that can identify the elements in the sample. A XPS device analyzed the chemical structure of MOFs. The XPS device was ESCALAB QXi X-ray Photoelectron Spectrometer Microprobe, Thermo Fisher. XPS can precisely identify and quantify the types of elements and chemical species present in a sample, as well as their chemical environments and bonding states [142]. This enables researchers to discern subtle differences in chemical bonding, oxidation states, and functional groups, making it a valuable tool for materials science, surface chemistry, and surface analysis [142]. XPS spectra were obtained by irradiating a solid surface with a X-ray beam and measuring the binding energy of electrons emitted from the material's top layer (1-10 nm). If deeper analysis is required, other techniques like Auger electron spectroscopy or depth profiling methods may be employed [142,143]. XPS is primarily used for the analysis of the top few atomic layers of a material's surface [142]. The binding energies of the photoelectrons emitted from a surface sample were used as a fingerprint to identify elements [144]. Chemical shifts in XPS spectra were observed when an element enters a different bound state, which changes the binding energy of electrons. Fourth, the morphology of the samples was analyzed by scanning electron microscopy (SEM). The SEM device was JEOL 6400 SEM. The surface of the samples was coated with gold before SEM analysis. A SEM projects and scans a focused stream of electrons over a surface to create an image. The electrons in the beam interact with the sample, producing

various signals that can be used to obtain information about the surface's topography and composition. An EDX device was used to identify the elemental composition of materials. The EDX device was the ThermoFisher Spectra Ultra. An X-ray beam is focused on the sample being studied to stimulate the emission of characteristic X-rays from a specimen. The EDX device is attached to an SEM device (SEM) where the imaging capability of the microscope identifies the elemental composition of the samples. The data generated by EDX analysis consists of spectra showing peaks corresponding to the elements making up the composition of the sample. Also, the elemental mapping of a sample can be provided by EDX analysis.

2.10 Electrochemical Analyses of the Pyrolyzed Samples

In this thesis, an RDE electrode was used. For this purpose, first, an ink from each sample was prepared by the following instruction. The inks were made by mixing Nafion solution with samples. First, Nafion solution in iso-propanol (1:10 V/V%) was prepared. Nafion is a brand name for a sulfonated tetrafluoroethylene-based fluoropolymer-copolymer discovered in the 1960s by Dr. Walther Grot in DuPont Inc [145]. The Nafion solution in the prepared ink served as the binder and ion conductor that provides an appropriate interface between the electrode materials and Nafion [146].

Afterward, 1 ml of Nafion solution was added to a vial. Then, 5 mg of the sample (black powder) was added to the vial. Finally, the mixture was mixed again with a shaker for 10 minutes to disperse any powder accumulation. The next step is ink casting by following instructions. First, 3.33 µl mixture was added to the RDE by an Eppendorf pipette and dried in a few minutes. Then, 3.33 µl cast again. Finally, 3.34 µl cast to reach 10 µl of the

mixture. Each time the film needs five minutes to dry, and then the next addition until it reaches three times. All samples have the same film and amount of sample on the RDE.

The electrochemical tests have two parts: CV and linear sweep voltammetry (LSV). The voltammetric analysis is a category of electroanalytical methods obtained by measuring the current as the potential is varied [147]. CV is an electrochemical technique commonly employed to determine molecular species' oxidation and reduction processes. CV, a potential sweep method, is the most used measurement technique in electrochemistry. CV involves sweeping an electrode potential linearly as a function of time and measuring the resulting current that flows through the circuit, which is a three-electrode electrochemical cell [148]. Unlike in LSV, after the set potential is reached in a CV analysis, the working electrode's potential is ramped in the opposite direction to return to the initial potential. These cycles of ramps in potential may be repeated as many times as needed (Like 300 cycles to evaluate the electrode's stability). The current at the working electrode is plotted versus the applied voltage (the working electrode's potential) to assess the redox reactions of sample [149]. The CV scan rate at room temperature was 10 $mV.s^{-1}$.

LSV is a voltammetric method where the current at a working electrode is measured while the potential between the reference electrode and the working electrode is swept linearly. Reduction and oxidation of species are determined as a peak or trough in the current signal at the potential at which the species begins to be reduced or oxidized [150]. Also, a wide range of rotation rates from 100 to 2500 rpm with a scan rate of 10 $mV.s^{-1}$ was used to perform the LSV analysis. All electrochemical analyses were performed in an oxygen-enriched electrolyte. For this purpose, oxygen dissolved in KOH 0.1 M using a compressed air tank for 30 minutes before any electrochemical tests. Then, CV and

LSV analyses were performed at room temperature. The LSV test in different rotations (100, 400, 900, 1600, and 2500 rpm) was performed to calculate the K-L equation and the number of electrons in the ORR process.

3.0 Results and Discussion

3.1 Characterization

The prepared MOFs, ZIFs, and their carbonized samples were characterized. The results are reported in the following sections.

3.1.1 Attenuated Total Reflectance Infrared Spectroscopy

ATR-IR spectroscopy determined the functional groups in MOFs and ZIFs before and after pyrolysis. The results of MOFs, including PPy-coated HKUST MOF before and after pyrolysis, are illustrated in Figure 9. The peaks at 489, 728, and 758 cm^{-1} are related to C-C bending, C-H rocking, and C-H alkene bending, respectively. The sharp peaks in 1367 and 1447 cm^{-1} are associated with C-H symmetrical bending and C-C aromatic stretching, respectively. Also, the peak in 1645 cm^{-1} belongs to the carboxyl groups of the HKUST MOF. Furthermore, the broad peak in 3200 cm^{-1} relates to absorbed H_2O by MOF before analysis. The peak at 599 cm^{-1} can be assigned to the vibrations of Cu-O bonds [151]. The results of ATR-IR of the MOF sample are similar to the results in the literature [152]. The IR spectra for a pyrolyzed sample at 700˚C and 800˚C are similar to graphene oxide [153]. Peaks at 1057 and 1730 cm^{-1} are related to C-O-C and C=O, respectively. Also, a peak at (3200-3700 cm^{-1}) is related to the hydroxyl groups in the Carbon_ZIFs [154]. Therefore, pyrolyzed PPy-coated HKUST MOF has similar functional groups to graphene oxide [153]. The peak intensity of the pyrolyzed samples is smaller than the sample before pyrolysis. It means the pyrolysis process removed most of the functional groups [155]. Hence, the pyrolyzed PPy-coated HKUST MOF has a graphene oxide structure.

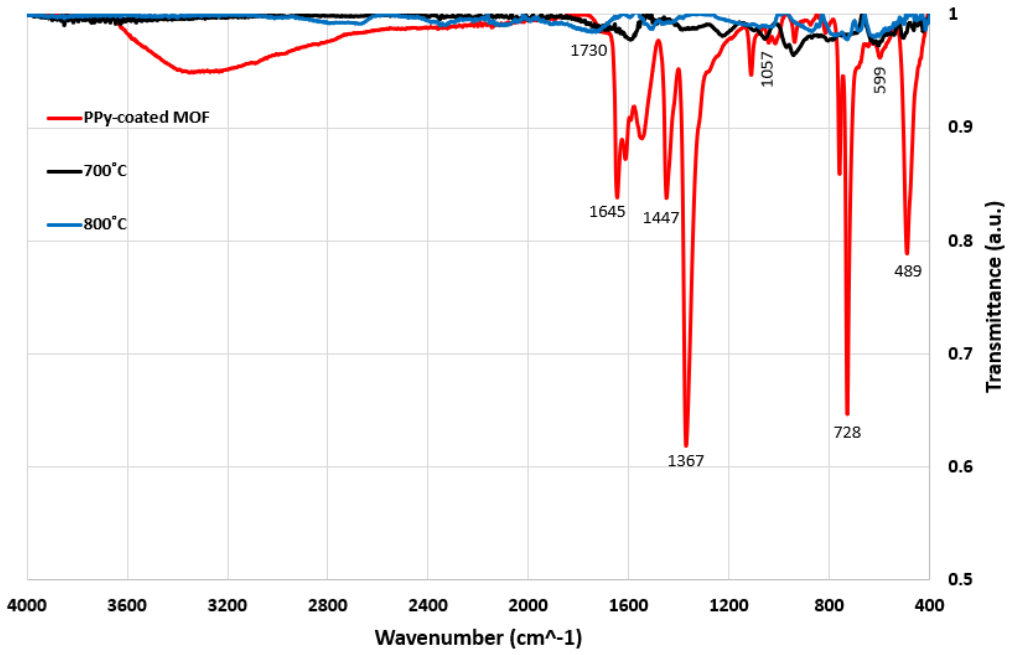

Figure 9: ATR-IR spectra of PPy-coated HKUST MOF (red), pyrolyzed PPy-coated HKUST MOF annealed at 700˚C (black), and pyrolyzed PPy-coated HKUST MOF annealed at 800˚C (blue).

The ATR-IR analysis of CoZIF, FeZIF, and CoFeZIF before pyrolysis is illustrated in Figure 10. According to Figure 10, all spectra have a broad peak in 3200 cm^{-1} related to the presence of water in the ZIF structure. This water has two origins, including the starting materials and absorption from the environment. The ZIFs have been prepared from metal nitrates that have water in their crystalline structure like $Co(NO_3)_2.6H_2O$. Since the synthesis process was completed in less than one minute, the water molecules remain in the ZIFs crystals. Also, ZIFs, a well-known humidity absorber material, can absorb water from the environment [156]. All three spectrums have a peak in 1624 cm^{-1} related to -C=N- bonds in ZIF structures. Also, peaks in (1283-1406 cm^{-1}) are related to -C-N- bonds in ZIF structures that overlap with the -C=C- peaks in 1400 cm^{-1}. The peak at 426 cm^{-1} is attributed to the Co-N stretching in CoZIF [157]. The peak at 876 cm^{-1} is

attributed to the Fe-N stretching in FeZIF [158]. The results for the CoZIF are similar to the ZIF-67 in the literature [159]. It determines that a novel solvent-free synthesis process is the correct method to prepare ZIFs.

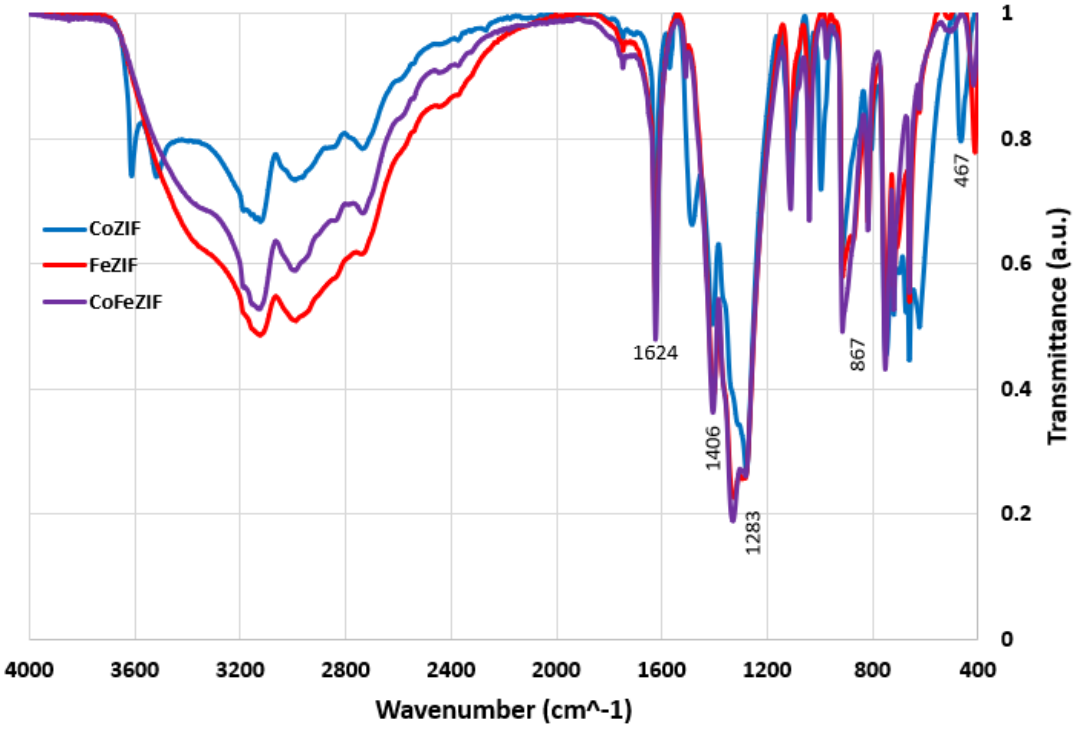

Figure 10: ATR-IR spectra of CoZIF (blue), FeZIF (red), and CoFeZIF (purple).

The ATR-IR spectra of the pyrolyzed ZIFs including CoZIF (Carbon_CoZIF), FeZIF (Carbon_FeZIF), and CoFeZIF (Carbon_CoFeZIF), have been illustrated in Figure 11. The pyrolyzed ZIFs (Carbon_ZIFs) have similar peaks to graphene oxide [155]. Peaks at 1057 and 1730 cm^{-1} are related to C-O-C and C=O, respectively [160]. Also, a peak at (3200-3800 cm^{-1}) is related to the hydroxyl groups in the Carbon_ZIFs. The peaks in Figure 11 are related to graphene oxide [153]. The peak intensity of Carbon_ZIFs is significantly lower than ZIFs in Figure 10. It indicates that pyrolysis removed most functional groups.

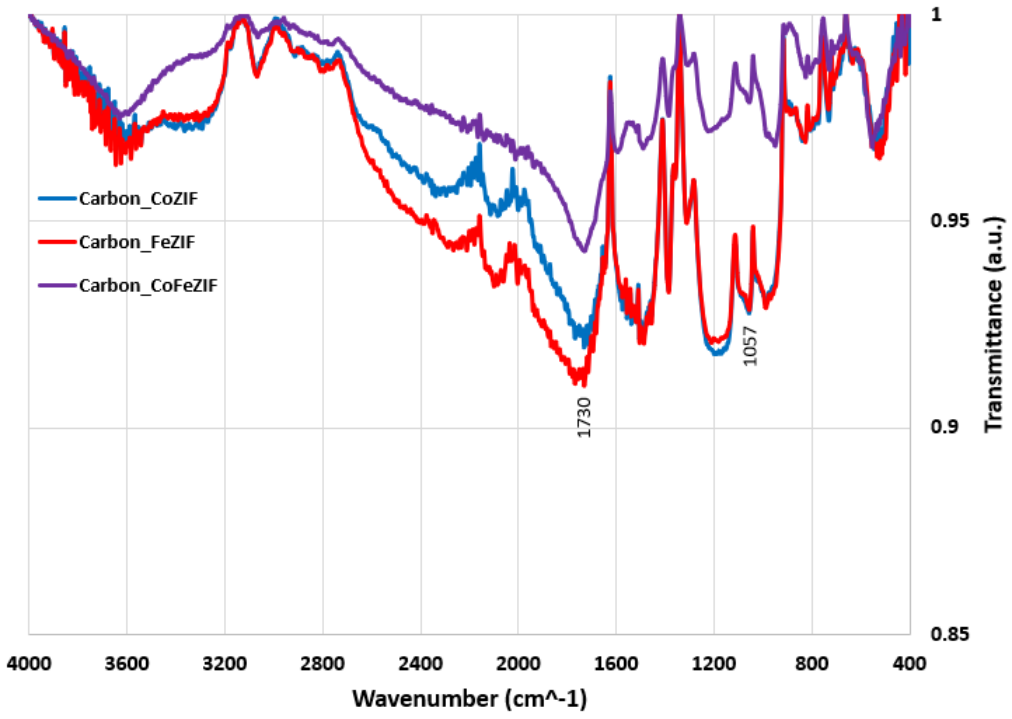

Figure 11. ATR-IR spectra of Carbon_CoZIF (blue), Carbon_FeZIF (red), and Carbon_CoFeZIF (purple).

ATR-IR analysis determined that pyrolyzed samples have a graphene oxide structure.

3.1.2 X-ray Diffraction

XRD was used to analyze the structural information of nanomaterials and crystals, such as lattice parameters and crystalline structure. The XRD patterns of PPy-coated HKUST MOF and its carbonized product at 900˚C are illustrated in Figure 12. The XRD pattern of PPy-coated HKUST MOF (Figure 12) is similar to the XRD pattern of HKUST MOF in the literature [130,152]. It is another proof to determine the synthesis method of HKUST MOF was correct. The pyrolyzed XRD pattern determined the metallic Cu existence

because of two peaks at 43 and 50 degrees [161]. Also, a broad small peak in (11-16) degrees indicates the fabrication of graphene oxide by the pyrolysis process [153]. The XRD patterns of the pyrolyzed PPy-coated HKUST MOF at different temperatures are illustrated in Figure 13. It indicates a similar crystalline structure in all pyrolyzed samples. All samples have two parts including graphene oxide metallic copper particles. Also, it indicates that the pyrolysis process leads to the turn of organic components of MOF to inorganic parts because all peaks related to the HKUST MOF have been removed after pyrolysis.

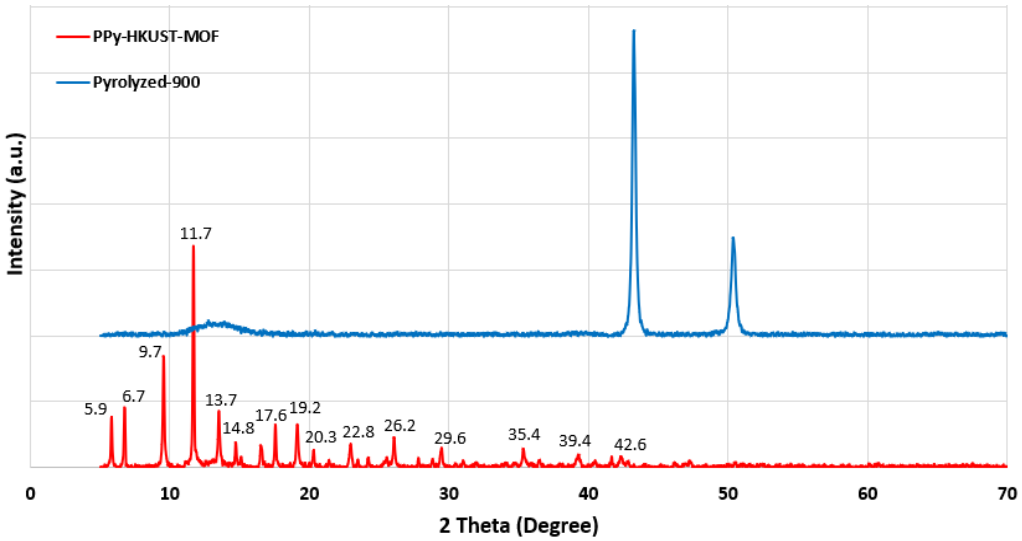

Figure 12: XRD patterns of PPy-coated HKUST MOF (red) and pyrolyzed PPy-coated HKUST MOF annealed at 900˚C (blue).

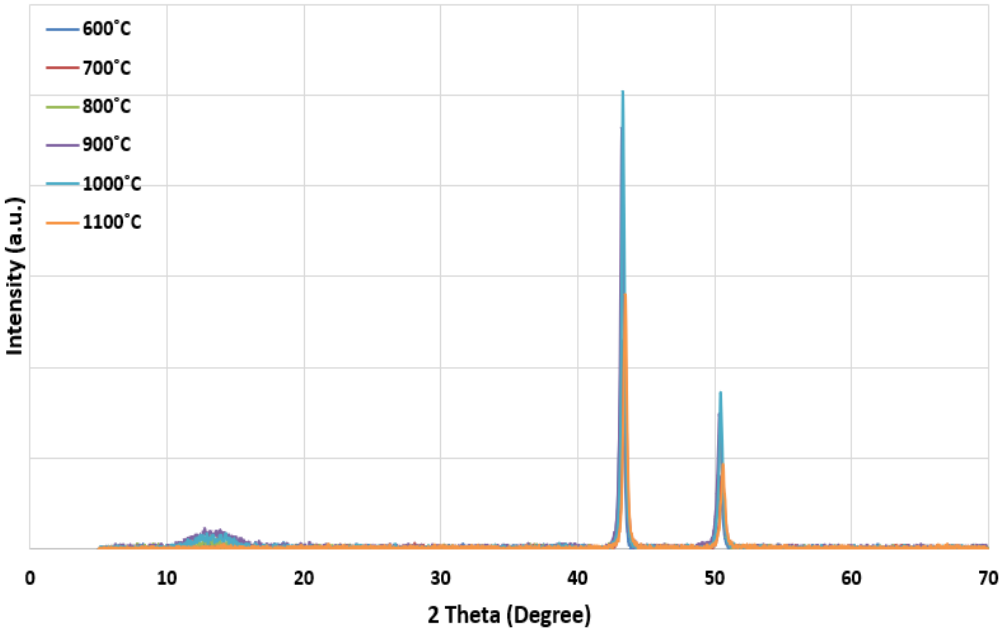

Figure 13: XRD patterns of pyrolyzed PPy-coated HKUST MOF annealed in 600, 700, 800, 900,1000, and 1100˚C.

Figures 12 and 13 determined that the MOF samples after pyrolysis in different temperatures have two significant phases: graphitic and copper. Also, a small broad peak of 15 degrees is related to the existence of graphene oxide in the pyrolyzed MOF samples.

The XRD patterns of the ZIFs are illustrated in Figure 14. The XRD pattern of CoZIF is like the XRD of CoZIF (ZIF-67) in literature [162]. It verified the modified solvent-free synthesis method for the preparation of ZIFs.

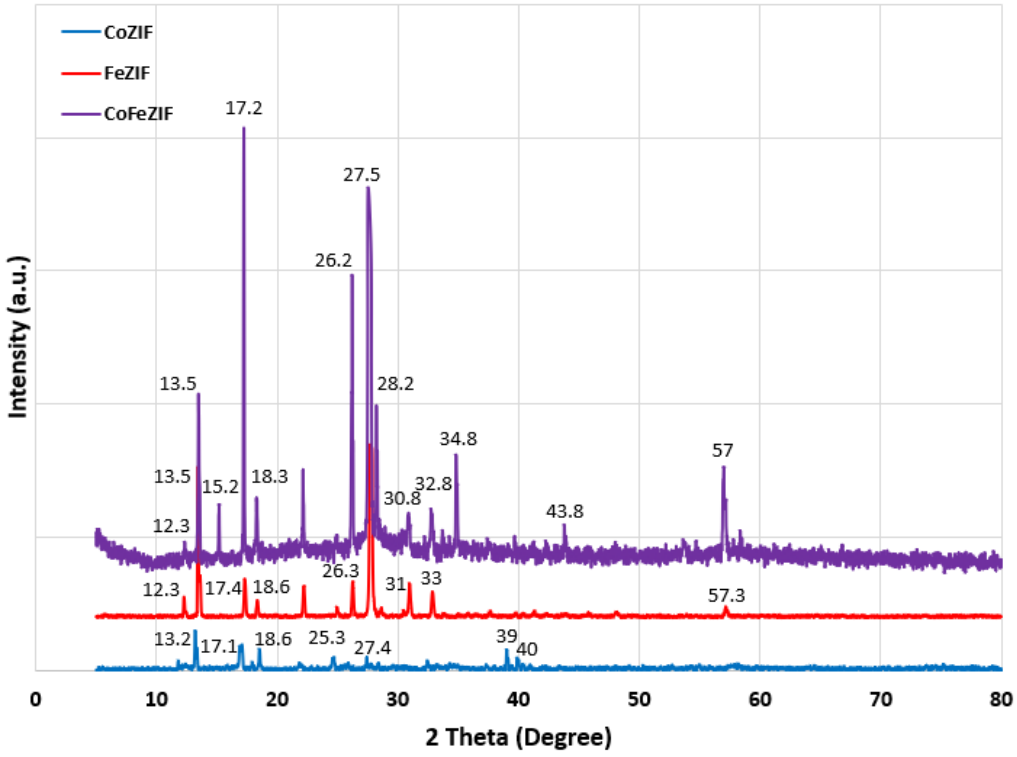

Figure 14. XRD patterns of CoZIF (blue), FeZIF (red), and CoFeZIF (purple).

Also, the XRD patterns of the pyrolyzed ZIFs before and after washing with HCl 2M are illustrated in Figures 15 and 16, respectively. According to Figure 15, the XRD patterns of Carbon_CoZIF and Carbon_FeZIF have peaks related to metallic cobalt and metallic iron, respectively [163]. The metallic cobalt has a peak at 45 degrees [163]. It indicates the presence of the metallic Co in the Carbon_CoZIF sample. The metallic Fe has two peaks at 45 and 65 degrees. It indicates the presence of the metallic Fe in the Carbon_FeZIF sample. The Carbon_CoFeZIF sample as a hybrid sample has both peaks. It means the pyrolyzed CoFeZIF has both Fe and Co metallic atoms as a separate phase [163]. The lattice planes are small but many in amorphous material [164]. The lattice planes individually scatter X-rays with low intensity, hence the broader XRD peaks [164]. Also, doping leads to

broadening the XRD peaks with less intensity because increasing of doping process decreases the crystallinity [165,166].

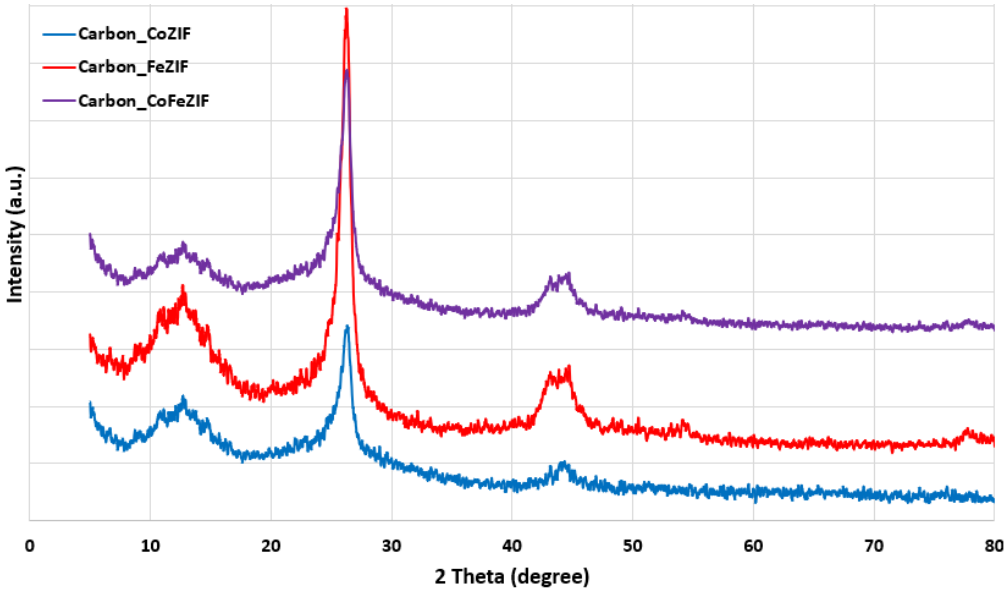

Figure 15: The XRD patterns of Carbon_ZIFs before washing with HCl 2M: Carbon_CoZIF (blue), Carbon_FeZIF (red), and Carbon_CoFeZIF (purple).

The acidic washing process removed most of the Fe and Co metallic parts on the Carbon_ZIFs. Hence, the metallic peaks have a considerable reduction after mixing with HCl. Also, the washing process leads to emerging graphite and graphene oxide peaks in the samples' patterns. The sharp peak of 26 degrees in all three samples was associated with graphite in the pyrolyzed samples. Also, the peak of 13 degrees is related to the presence of graphene oxide. According to Figure 16, the significant parts of the pyrolyzed samples are graphite and graphene oxide [167]. The XRD analysis, like ATR-IR, determined that the pyrolysis of MOF and ZIF samples provide graphite and graphene oxide structure.

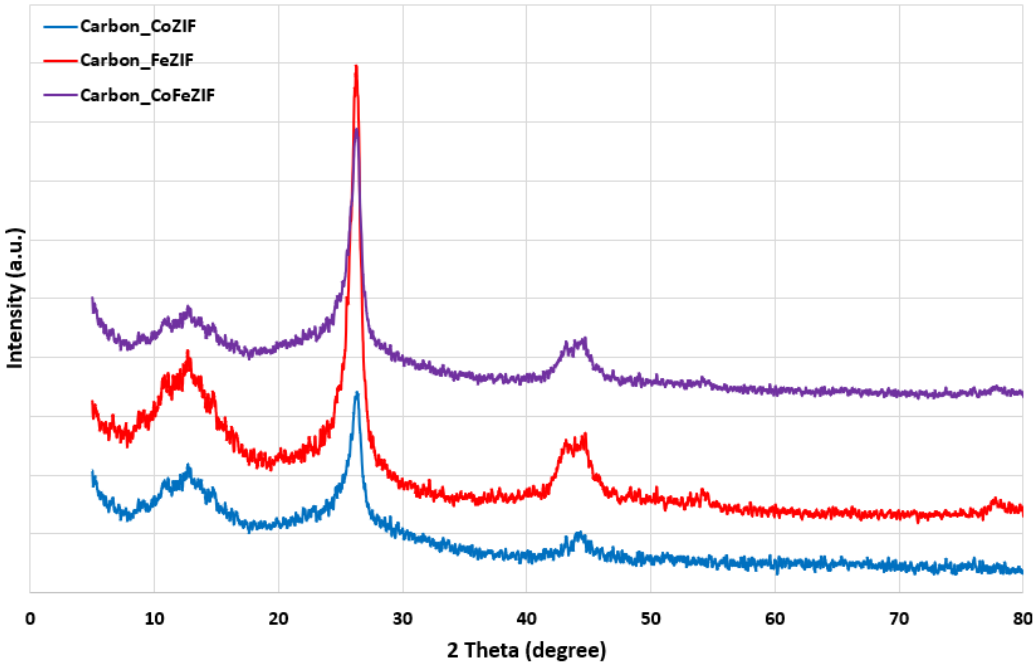

Figure 16: The XRD patterns of Carbon_ZIFs after washing HCl 2M: Carbon_CoZIF (blue), Carbon_FeZIF (red), and Carbon_CoFeZIF (purple).

3.1.3 X-ray Photoelectron Spectroscopy (XPS)

XPS analysis determines the chemical bonds in the structure by detecting the binding energies. This analysis has been widely used to determine the functional groups in the carbon structure. This project used XPS to evaluate the chemical bonds in PPy-coated HKUST MOF and the pyrolyzed sample from PPy-coated HKUST MOF. The XPS spectrum of carbon 1s (C1s) bonds in PPy-coated HKUST MOF is illustrated in Figure 17. The C1s peak can be deconvoluted into two peaks with binding energy centered at 285.08 eV and 288.88 eV. The peak value of 285.08 eV corresponds to the C-C and C-H on the surface of PPy-coated HKUST MOF [168,169]. Also, the peak value of 288.88 eV corresponds to the O-C=O on the surface of PPy-coated HKUST MOF [168,170]. The envelope spectrum was obtained from mathematical models by removing spectrum

distortions [143]. Then, the envelope spectrum was deconvoluted into sub-spectrums to determine different chemical bonds formed. Also, the background spectrum is an approximation that different mathematical methods have calculated. The background estimation is the first step for removing the background from an XPS spectrum [171].

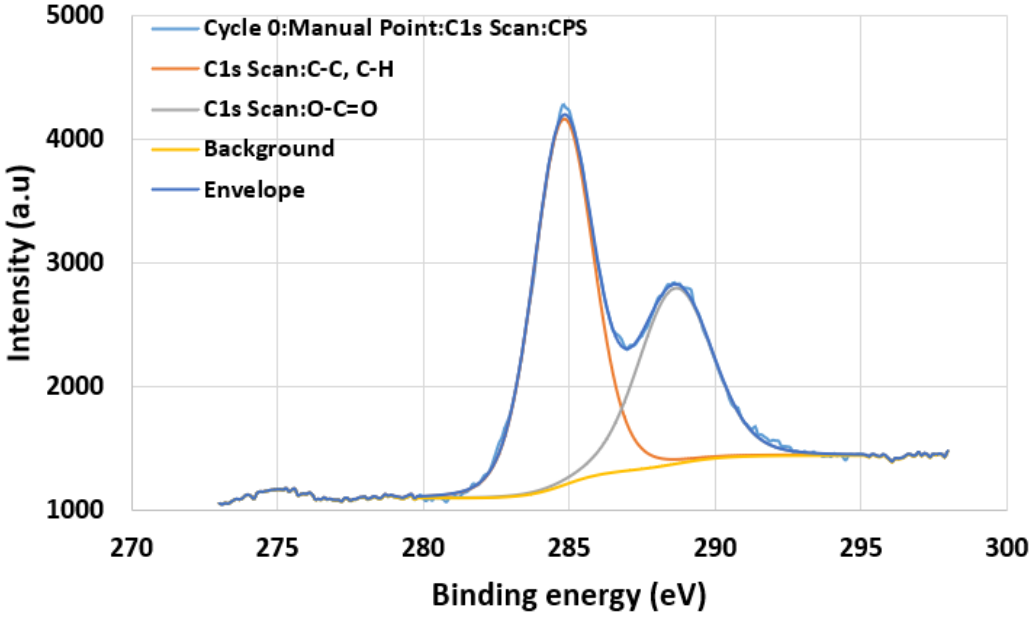

Figure 17: The C1s XPS spectrum of PPy-coated HKUST MOF.

The C1s XPS spectrum of PPy-coated HKUST MOF that was pyrolyzed at 800˚C is illustrated in Figure 18. The peak value of 284.5 eV corresponds to the C-C and C-H on the surface of sample [168]. The main part of the C1s still belongs to C-C and C-H bonds, but most of the carboxyl groups were removed after pyrolysis. There are some other functional groups with small intensity, such as hydroxyl, ether, and ketone functional groups. The peak value of 286.4 eV corresponds to the C-OH and C-O-C functional groups on the sample's surface. The peak values of 287.9 eV and 288.6 eV correspond to the C=O and O-C=O, respectively [168]. Also, the peak value of 290.4 eV corresponds to the C1s satellite peak. A satellite peak is used to identify shake-ups, energy loss, and

various unidentified peaks. It appears as a peak to the high binding energy sides of the XPS spectrum's main peak. Comparing Figures 17 and 18 determined that the pyrolysis process removed most of the carbonyl and carboxyl groups, but the C-C bonds remained.

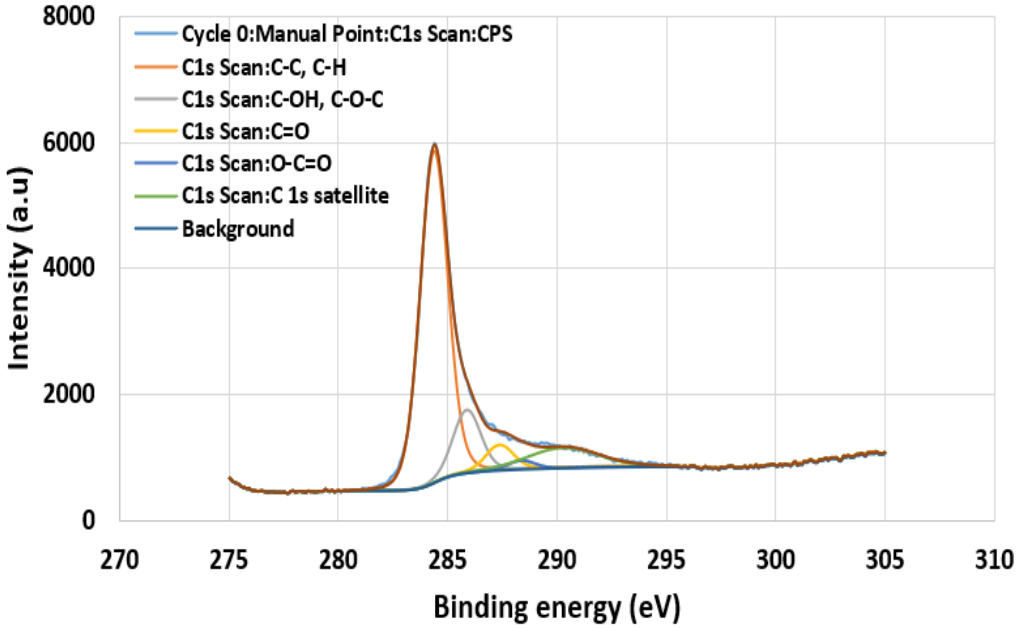

Figure 18: The C1s XPS spectrum of PPy-coated HKUST MOF that pyrolyzed at 800˚C.

The N1s XPS spectrum of PPy-coated HKUST MOF and PPy-coated HKUST MOF that pyrolyzed at 800˚C is illustrated in Figures 19 and 20, respectively. The peak at 399.28 eV is related to C-N bond [172]. This nitrogen peak originated from the polypyrrole coating on the HKUST MOF to fabricate PPy-coated HKUST MOF. Therefore, the coatings process was successfully performed and PPy particles were sedimented on the HKUST MOF surface. Also, the N1s XPS spectrum for the sample after pyrolysis determined that most nitrogen-containing compounds were removed by pyrolysis.

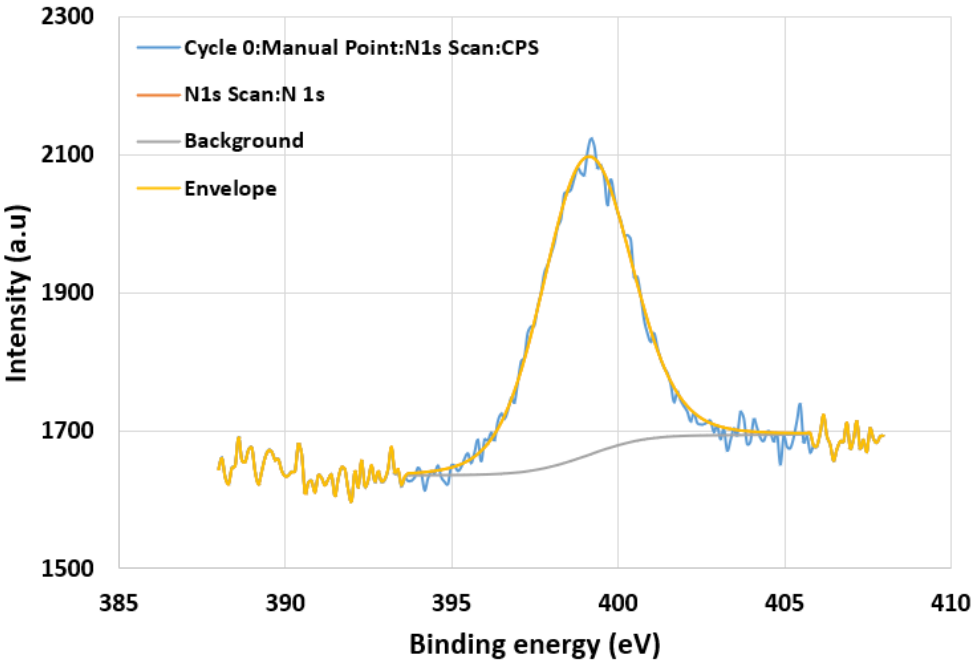

Figure 19: The N1s XPS spectrum of PPy-coated HKUST MOF.

The N1s peak in the pyrolyzed sample determined the negligible presence of nitrogen in the pyrolyzed sample. The peak intensity of N1s in pyrolyzed samples is very low at 401.11 eV. Therefore, the PPy-coating method cannot guarantee the existence of enough nitrogen in the carbon structure. The organic coating (PPy-coating) can be decomposed and evaporated in the furnace even before 800˚C. Therefore, ZIFs can be a better selection than MOFs because ZIFs have nitrogen in their structure and have covalent bonds, but PPy as a source of nitrogen was coated on the HKUST MOF surface and attached by physical bonds [109].

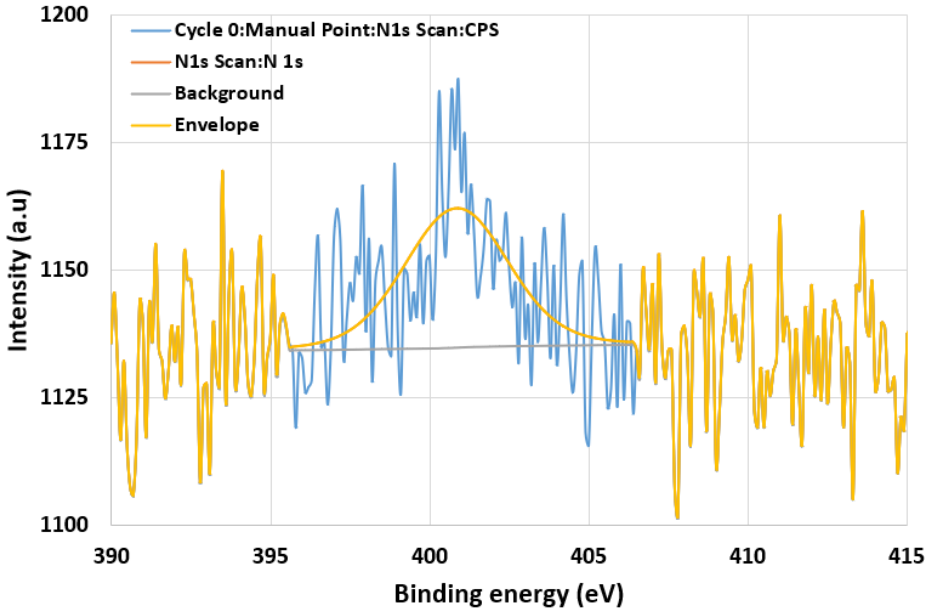

Figure 20: The N1s XPS spectrum of PPy-coated HKUST MOF that pyrolyzed at 800˚C.

The Cu2p XPS spectra of PPy-coated HKUST MOF before and after pyrolysis at 800˚C are reported in Figure 21 and Figure 22. The 2P orbital has two spin-orbit splitting: $2P_{\frac{1}{2}}$ and $2P_{\frac{3}{2}}$ [173]. Therefore, the Cu2p XPS spectrum has two types of peaks for 2P orbitals including $2P_{\frac{1}{2}}$ and $2P_{\frac{3}{2}}$. $2P_{\frac{1}{2}}$ has a peak at 952.8 eV. Each Cu atom in the HKUST MOF structure is connected to four oxygen atoms and one hydroxyl functional group. The major peak at 931.8 eV is related to Cu-O bonds, and the smaller peak at 934.4 eV is associated with Cu-OH bonds. Also, there are three shake-up peaks at 938.5, 941.4, and 943.4 eV. The shake-up in XPS spectra is described as intrinsic energy losses while the photoelectron leaves the hosting atom. The first-row transition metals, either metallic or in the oxide form, display clear shake-up features in the corresponding 2p core level [174]. There is a finite probability that an ion after photoionization will be left in a specific excited energy state a few eV above the ground state through excitation of the ion by the outgoing photoelectron. When this happens, the emitted photoelectron's kinetic energy is

reduced, which will be seen as shake-up peaks at higher binding energy than the main peak [174]. The Cu2p XPS spectrum of the MOF sample determined that the Cu atoms in the MOF structure have Cu-O and Cu-OH bonds. The Cu2p XPS spectrum of HKUST MOF is similar to the literature which confirms the synthesis method [175].

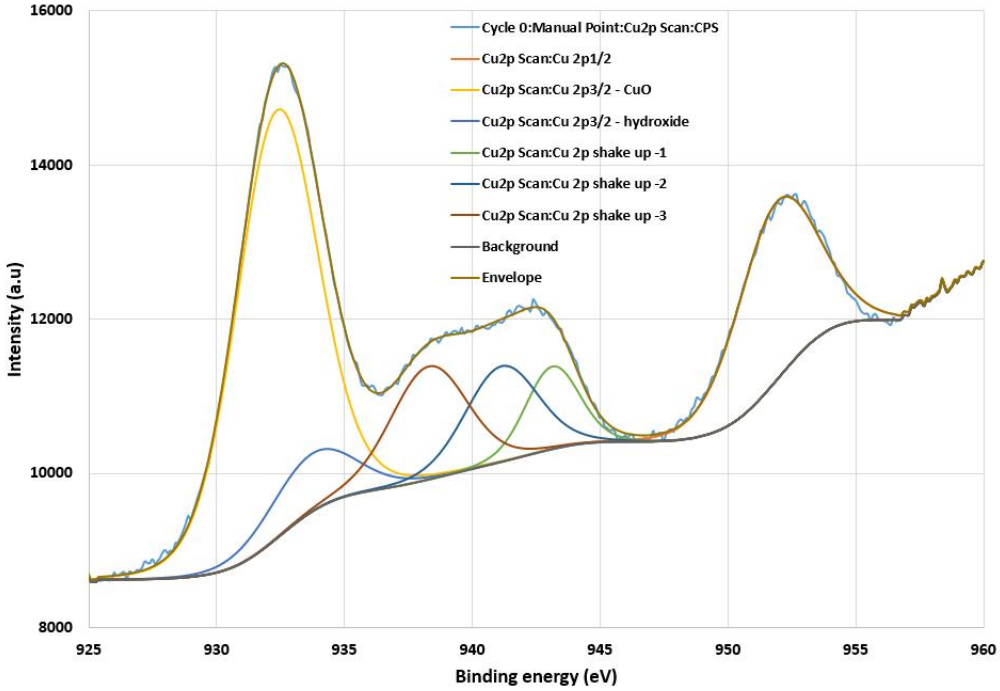

Figure 21: The Cu2p XPS spectrum of PPy-coated HKUST MOF.

The Cu2p XPS spectrum of PPy-coated HKUST MOF that pyrolyzed at 800˚C is reported in Figure 22. $2P_{\frac{1}{2}}$ can be deconvoluted to two peaks at 952.3 and 954.2 eV. There are two significant peaks for $2P_{\frac{3}{2}}$: CuO and CuO_2. It means Cu(I) oxide was produced in the pyrolysis process. Also, the peak related to Cu-OH disappeared because the MOF structure released water in the pyrolysis process. There are three shake-up peaks at 938.9, 941.1, and 943.8 eV in the Cu2p XPS spectrum. The XPS spectrum determined the Cu(I) oxide formation in the sample.

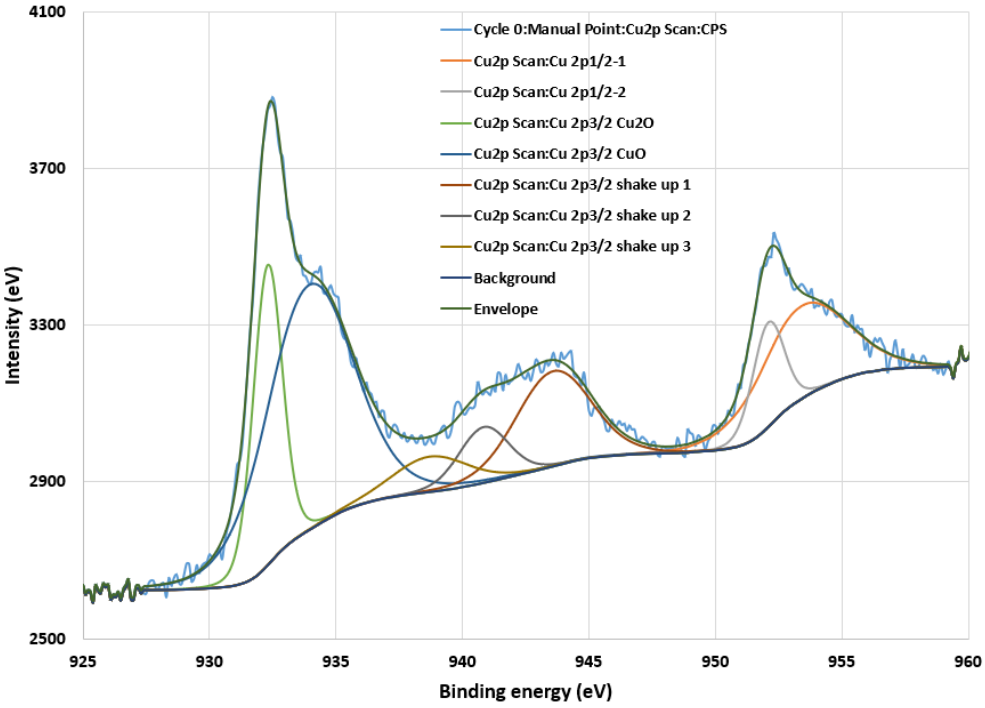

Figure 22: The Cu2p XPS spectrum of PPy-coated HKUST MOF that was pyrolyzed at 800˚C.

3.1.4 Scanning Electron Microscopy (SEM)

Scanning electron microscopy (SEM) has been used to illustrate the morphology and structure of the samples. This project used SEM images to report the microscopic structure of MOFs and ZIFs.

The SEM image of PPy-coated HKUST MOF before pyrolysis is illustrated in Figure 23. The small particles on the surface of the sample are polypyrrole. PPy-coating covers most surfaces of the HKUST MOF. The SEM image of PPy-coating HKUST MOF is similar to previous studies [109]. It determined that the coating process of HKUST MOF was completed successfully.

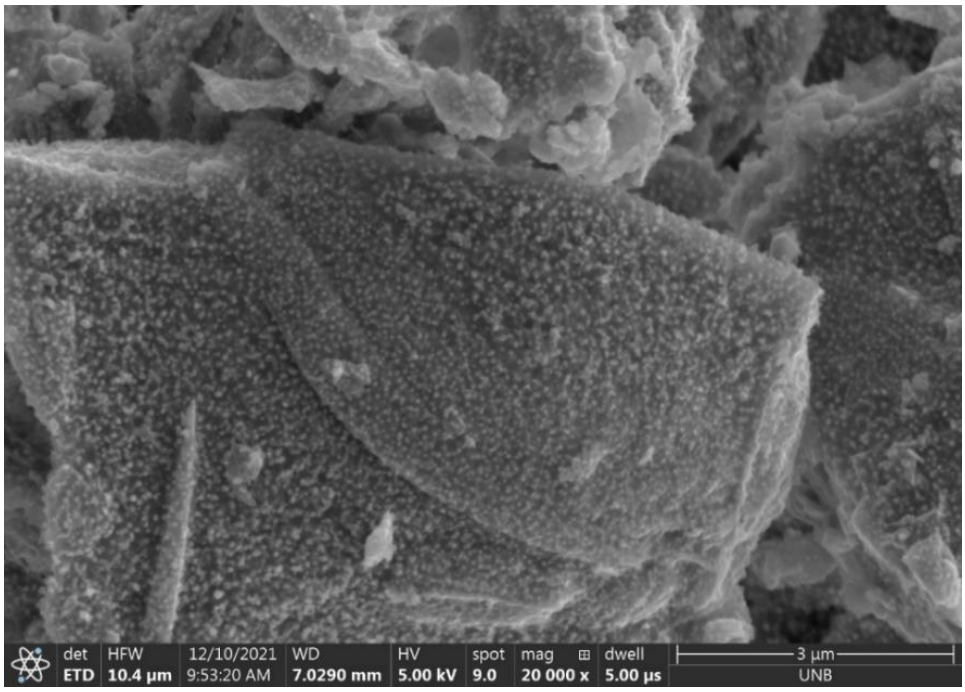

Figure 23: The SEM image of PPy-coated HKUST MOF.

The SEM image of CoZIF before and after pyrolysis is reported in Figures 24 and 25, respectively. The particles in Figure 24 are not completely cubic like the previous studies[176] because CoZIF was prepared instantly and the reaction time was about one second. The CoZIF crystals had no time to be formed.

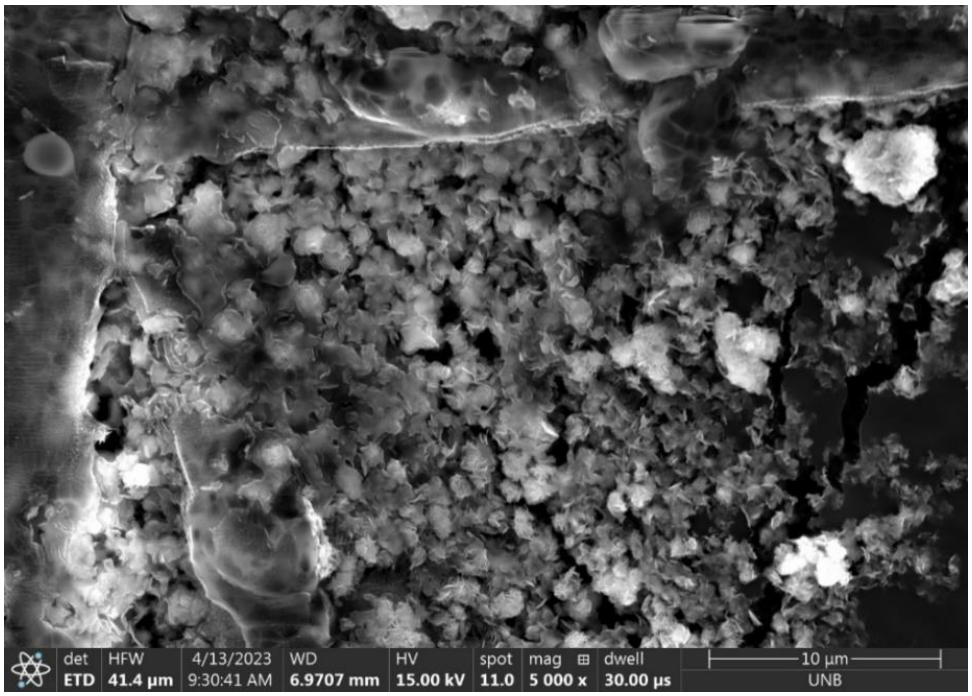

Figure 24: The SEM image of CoZIF.

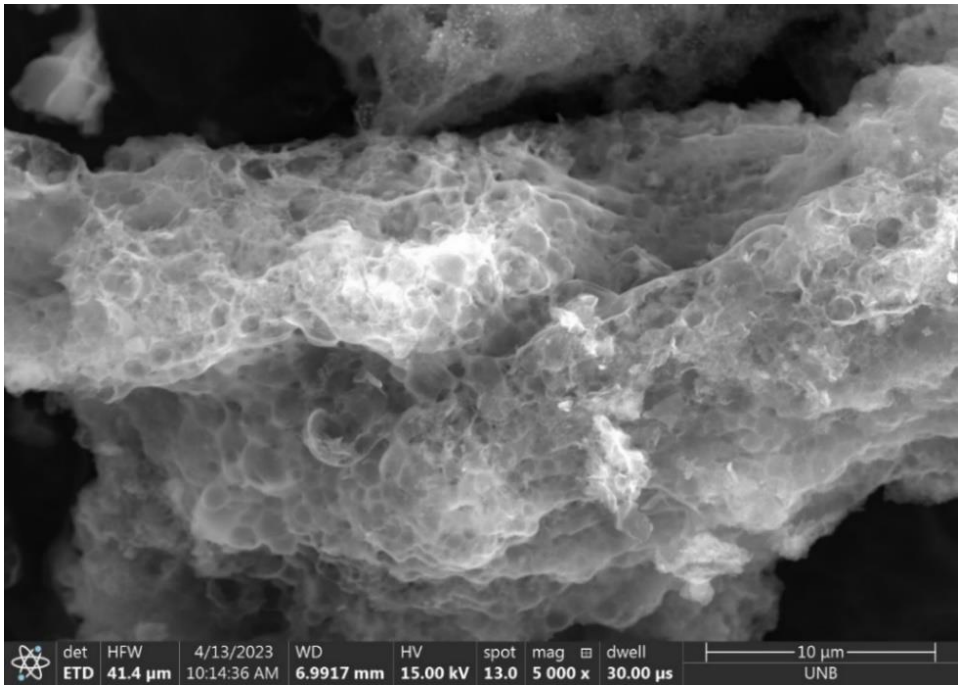

Figure 25: The SEM image of CoZIF that pyrolyzed at 800˚C.

Both SEM images of CoZIF before and after pyrolysis determined the porous structure of CoZIF. The pyrolysis of carbon materials can increase their porosity by providing

macropores (>50 nm), mesopores (2-50 nm), and nanopores (<2 nm) [177]. At the early pyrolytic stage, many small molecules such as N_2 and NH_3 are generated and stored as bubbles in the skeleton. These molecules then became different pore structures in the carbon structures. With the increasing in the pyrolytic temperature, the molecules expanded and then released from the surface of the skeleton, which destroyed the integrity of the skeleton and resulted in the volume shrinkage [178]. However, heating more than the optimized temperature can decrease the porosity [179,180] because nanopores and mesopores were decreased in higher temperatures [180]. The SEM images of FeZIF before and after pyrolysis at 800˚C are reported in Figures 26 and 27. Figures 26 and 27 determined that the FeZIF sample has pores before and after pyrolysis. Diffusion is one of the most critical parameters in the electrocatalysts' performance. The electrocatalyst diffusion is dependent on the electrocatalyst porosity. Therefore, these cobalt and iron ZIFs have an acceptable potential to be used as electrocatalysts. The SEM images of CoZIF and FeZIF differ from some publications that reported CoZIF (ZIF-67) because most publications have reported a solvent-based synthesis method, not a solvent-free procedure. The second reason is that the current study used a faster method than the common methods. Therefore, the crystals had no time to be formed.

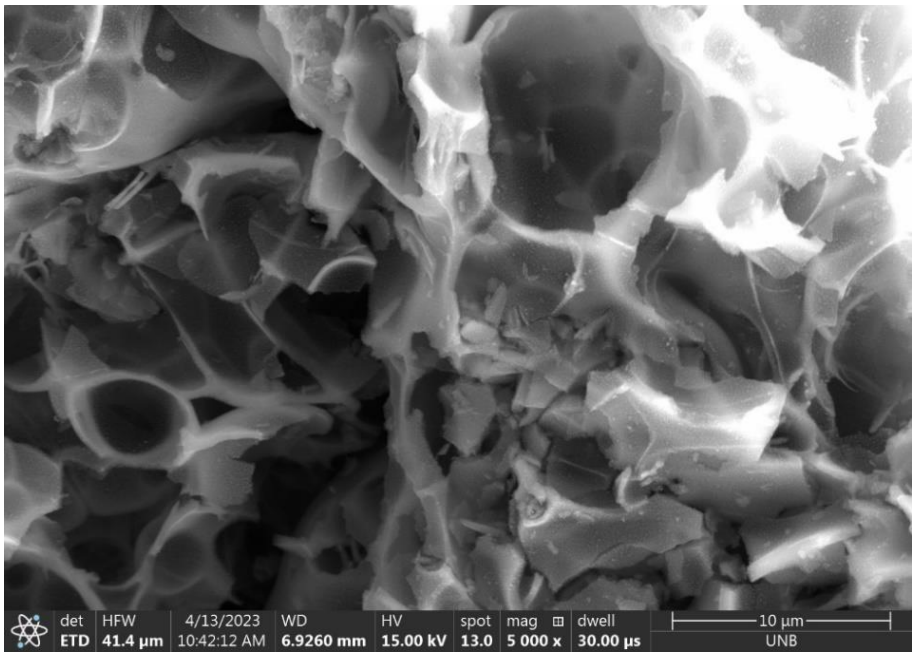

Figure 26: The SEM image of FeZIF.

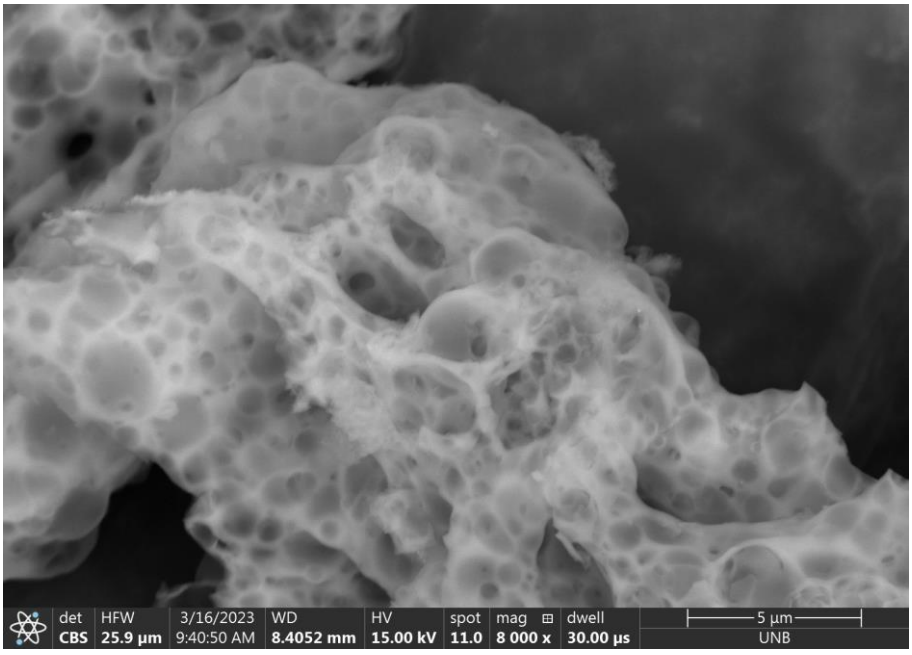

Figure 27: The SEM image of FeZIF that pyrolyzed 800˚C.

According to the SEM images, the MOFs and ZIFs have porous structures before and after pyrolysis. The higher porosity leads to improve electrocatalytic performance through increasing the mass transfer into the electrocatalyst pores [181]. Increasing the

porosity can improve the electrocatalytic activity by enhancing three parameters including increasing mass transport, reducing diffusion limitation, and increasing electrolyte penetration into electrocatalyst [181]. Also, both broad peaks in XRD patterns and SEM images confirmed the existence of the amorphous structure in the pyrolyzed MOF and ZIF samples.

3.1.5 Energy Dispersive X-Ray Analysis (EDX)

The EDX analysis was used to identify elements in CoZIF and FeZIF samples before and after pyrolysis. This method was used to evaluate the influence of the pyrolysis process on the elemental composition of CoZIF and FeZIF samples. The EDX spectrum and EDX mapping analysis of the CoZIF sample before pyrolysis are reported in Figures 28 and 29 respectively. According to Figure 28, carbon is the major element in CoZIF. Also, CoZIF contained nitrogen (from MIM) and cobalt (from CoN). The EDX-mapping analysis of CoZIF in Figure 29 determined the presence of Co and N atoms throughout the sample.

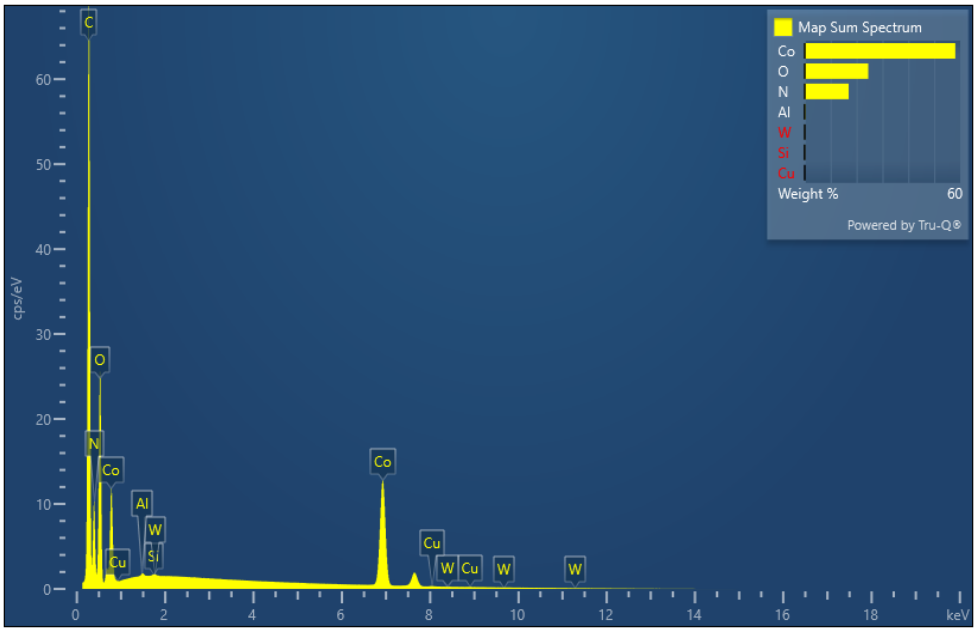

Figure 28: The EDX analysis of CoZIF before pyrolysis.

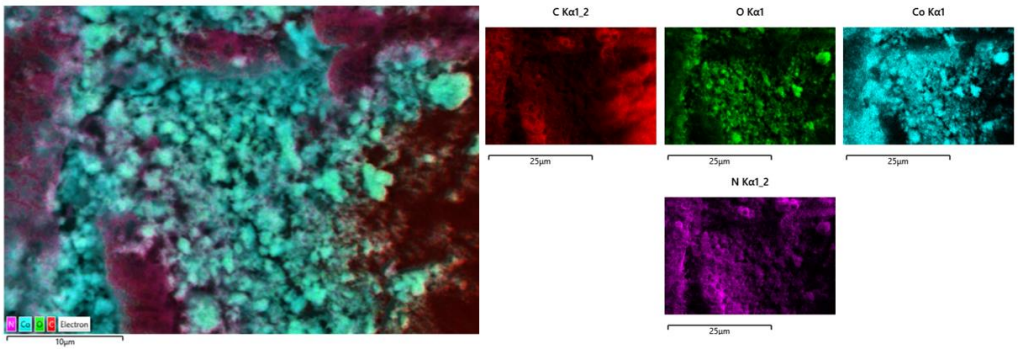

Figure 29: The EDX-mapping of CoZIF before pyrolysis.

The EDX spectrum and EDX-mapping analysis of the CoZIF sample after pyrolysis at 800˚C are reported in Figures 30 and 31 respectively. According to Figure 30, the Carbon_CoZIF sample contained N and Co atoms. The pyrolyzed PPy-coated HKUST MOF sample lost most of the nitrogen groups after pyrolysis but Carbon_CoZIF has Co and N atoms after pyrolysis at 800˚C.

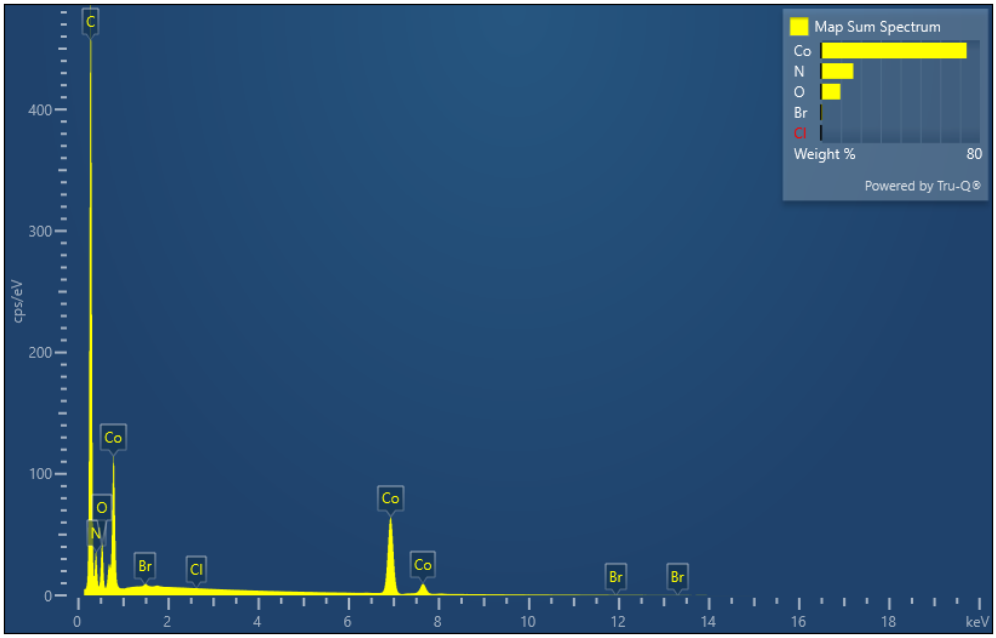

Figure 30: The EDX analysis of Carbon_CoZIF after pyrolysis at 800˚C.

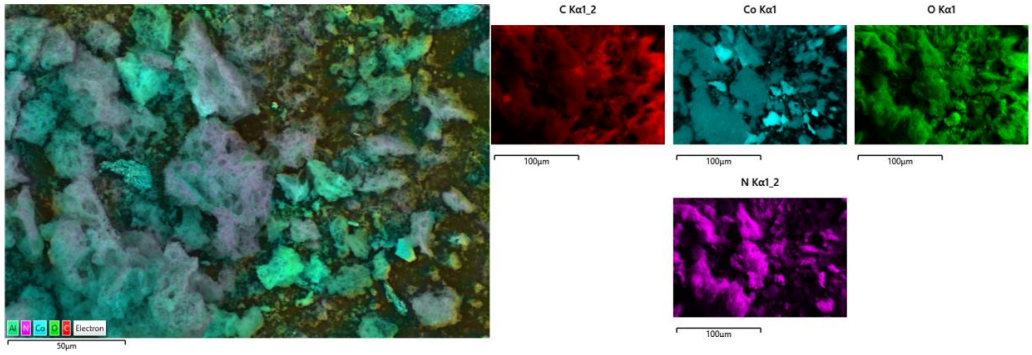

Figure 31: The EDX-mapping analysis of Carbon_CoZIF after pyrolysis at 800˚C.

The EDX spectrum and EDX-mapping analysis of the FeZIF sample before pyrolysis are reported in Figures 32 and 33 respectively. According to Figure 32, carbon is the major element in FeZIF. Also, FeZIF contained nitrogen (from MIM) and iron (from FeN). The EDX-mapping analysis of FeZIF in Figure 33 determined the presence of Fe and N atoms throughout the sample.

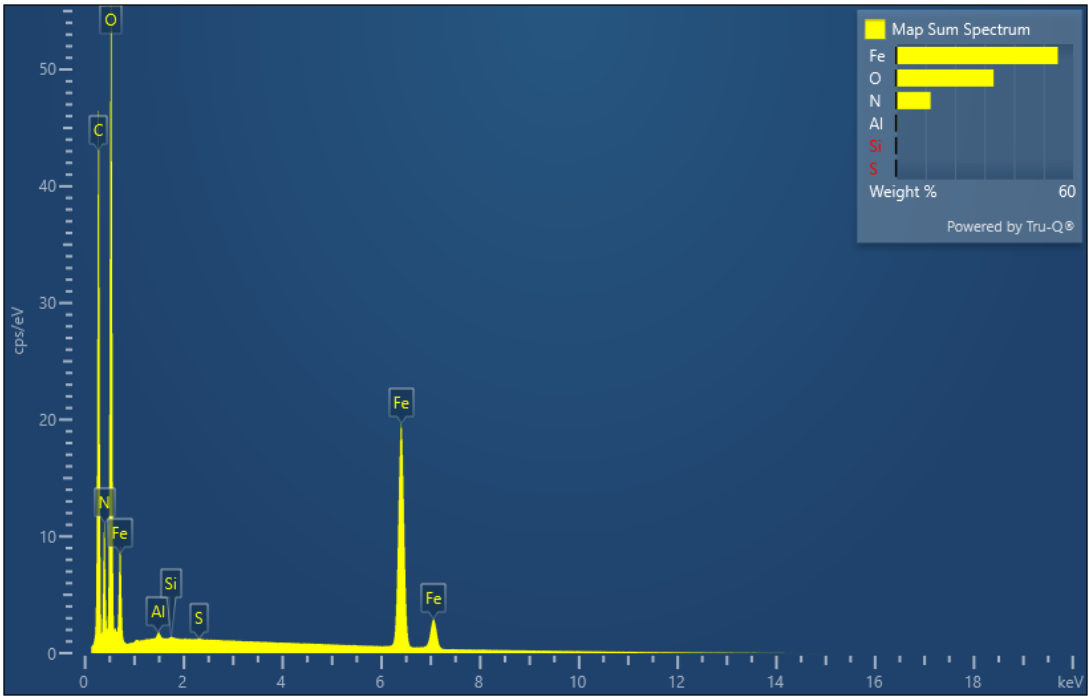

Figure 32: The EDX analysis of Carbon_FeZIF before pyrolysis.

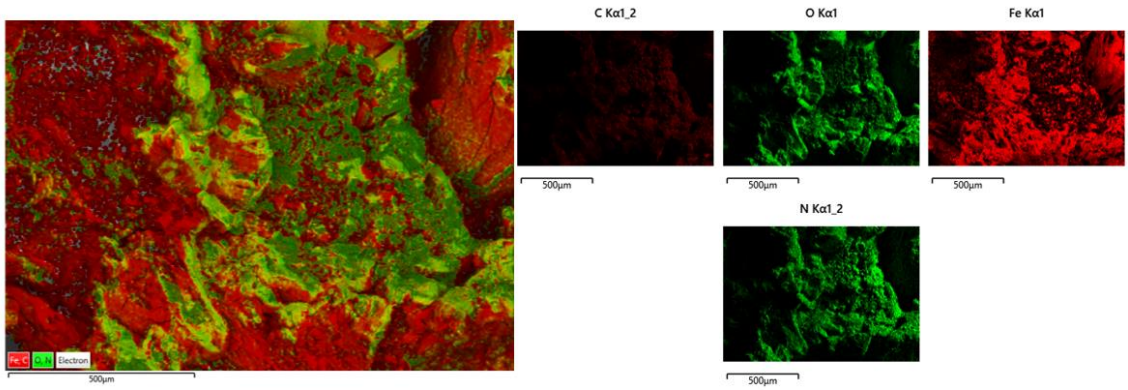

Figure 33: The EDX-mapping analysis of Carbon_FeZIF before pyrolysis.

The EDX spectrum and EDX-mapping analysis of the FeZIF sample after pyrolysis at 800˚C are reported in Figures 34 and 35 respectively. According to Figure 34, the Carbon_FeZIF sample contained Fe atoms, but it didn't contain an N peak. Also, the

carbon peak has a lower intensity than Carbon_CoZIF. It determines the pyrolysis of CoZIF provides a better sample than Carbon_FeZIF because Carbon_CoZIF contained nitrogen after the pyrolysis process.

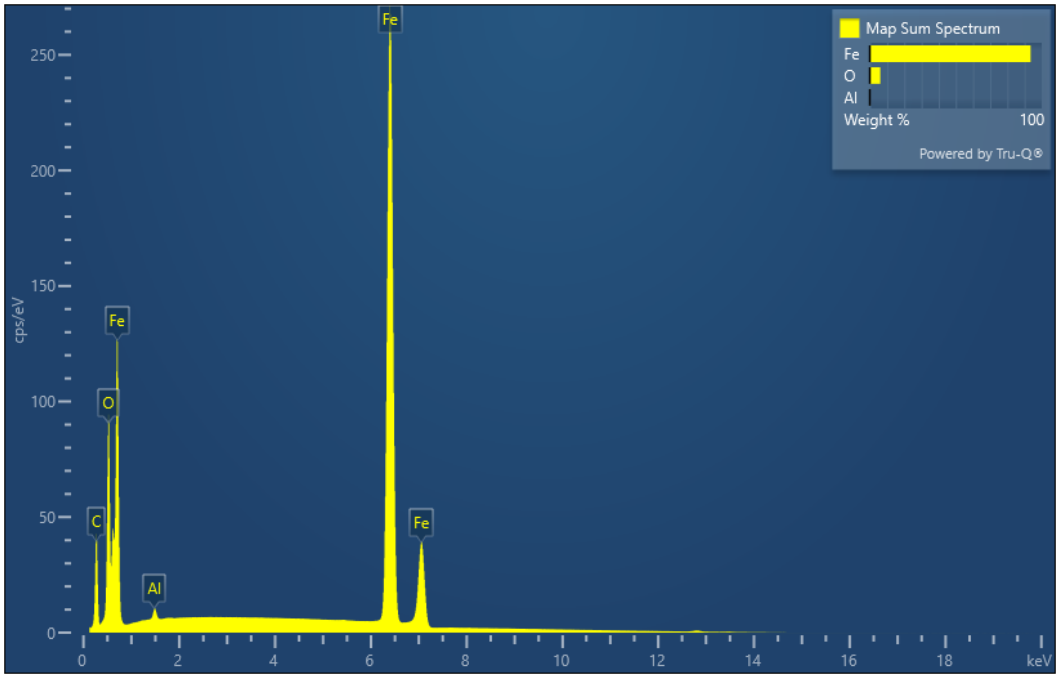

Figure 34: The EDX analysis of Carbon_FeZIF after pyrolysis at 800˚C.

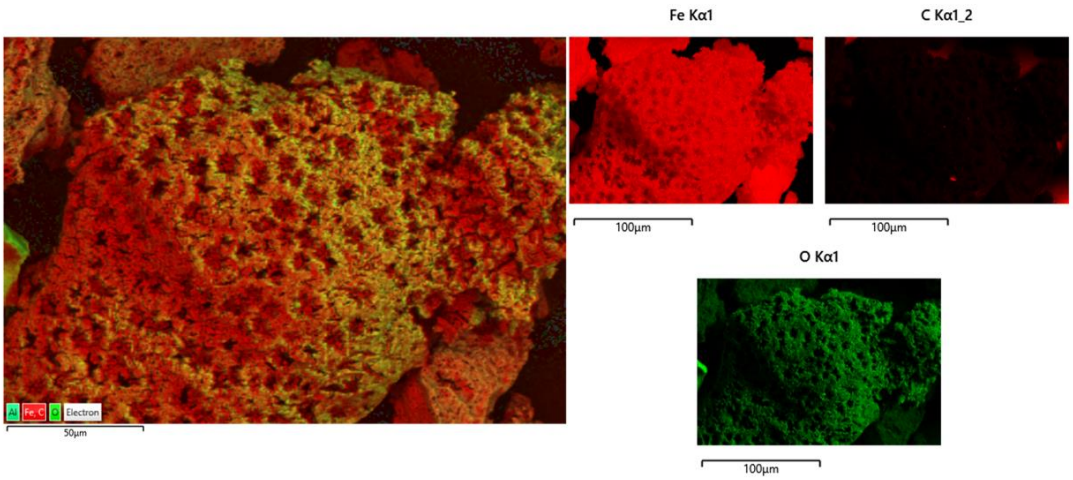

Figure 35: The EDX-mapping analysis of Carbon_FeZIF after pyrolysis at 800˚C.

3.2 Electrochemical Properties

3.2.1 Electrochemical Set-up

All electrochemical analyses were performed in KOH 0.1M as an electrolyte. Also, a RDE from Pine Instruments was used for all analyses. The electrochemical set-up is illustrated in Figure 36. The electrochemical analyses were performed at room temperature. For ORR and stability analyses, the electrolyte was saturated with oxygen.

The CV and LSV analyses for the ORR analyses were performed using an O_2-saturated KOH electrolyte. For this purpose, the electrolyte aerated with compressed air to increase the dissolved oxygen value in the electrolyte. The O_2-saturated electrolytes have been used for the ORR reaction in MABs and FCs because increasing the dissolved oxygen value leads to improving the ORR performance by improving the cathode reaction [182]. But electrolyte saturation by oxygen cannot improve the OER performance. Therefore, electrolytes for the OER analysis were not aerated [183].

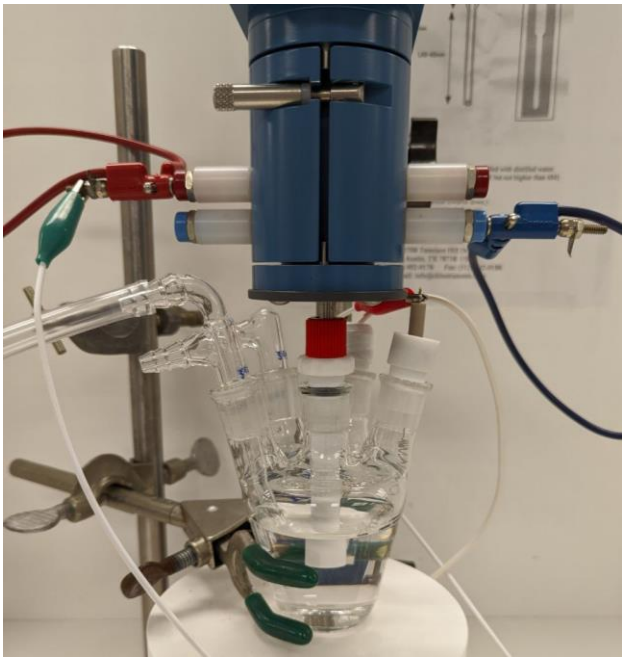

Figure 36: The electrochemical set-up.

3.2.2 Electrochemical Analysis of MOFs

CV is a type of voltammetry that allows the study of the redox properties of compounds. It determines the reduction and oxidation peaks in a potential window. The CV graphs in 10 mVs^{-1} of the PPy-coated HKUST MOF that pyrolyzed in different temperatures are reported in Figure 37. The sharp peak of sample 1100˚C at -0.16V is related to the oxidation of copper. Also, the peak at -0.52V is related to the copper reduction. The area under the CV voltammogram of PPy-coated HKUST MOF that pyrolyzed at 600˚C has the lowest current magnitude.

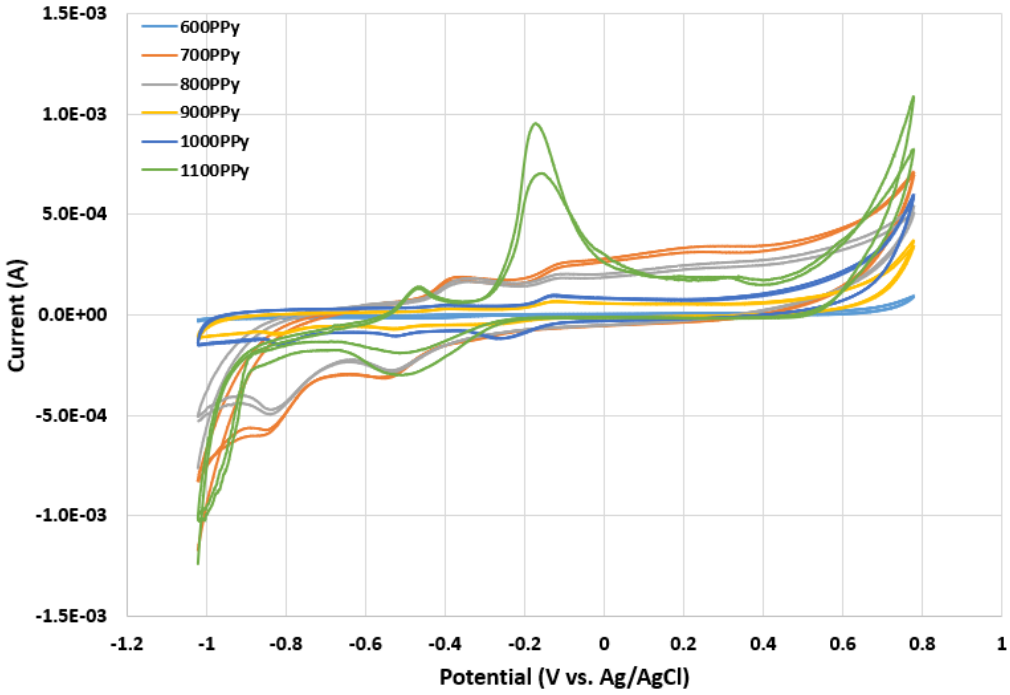

Figure 37: The cyclic voltammogram in 10 mVs^{-1} of PPy-coated HKUST MOF that pyrolyzed at 600, 700, 800, 900, 1000, and 1100˚C in O_2-saturated electrolyte.

The linear cyclic voltammetry (LSV) applied a linear potential over time and at a specific potential. The LSV graphs have been widely used to determine the electrocatalytic activity of the substances. Different samples can be compared at 1600 rpm to determine their electrocatalytic performance. In this project, the platinum-carbon with 20% platinum as the standard sample for the ORR process was used to determine the ORR performance of the samples. The LSV graphs of the pyrolyzed PPy-coated HKUST MOF and platinum-carbon (PtC) sample at 1600 rpm are illustrated in Figure 38. The oxygen reduction peak for the PtC sample starts at -0.05V. The ideal electrocatalyst should have a similar reduction peak. The reduction peak for the 1000˚C sample is -0.15V. Also, the reduction peak for samples 700, and 800 starts at -0.2V, and other samples start at -0.3V. It means samples 1000, 700 and, 800˚C have better ORR performance than other samples. But still, even the best sample (1000˚C) performs less than the standard PtC

sample. The CV and LSV analyses of PPy-coated HKUST MOF determined that the samples that pyrolyzed at 700, 800, and 1000˚C have the highest electrochemical performance (larger electrochemically active surface area) than the other samples.

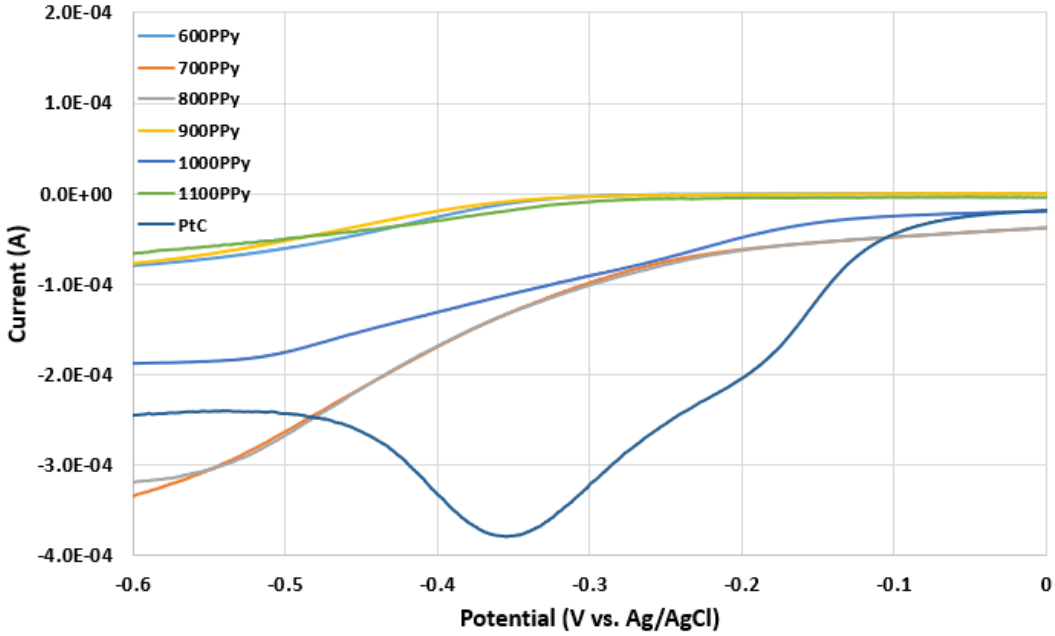

Figure 38: The LSV voltammogram in 1600 rpm of PtC and PPy-coated HKUST MOF that pyrolyzed at 600, 700, 800, 900, 1000, and 1100˚C in O_2-saturated electrolyte.

Figure 39 compares the CV voltammograms of MOF samples 700, 800, and 1000˚C with PtC as the standard sample in KOH electrolyte. The reduction peak for the 1000˚C sample started around -0.1V, and for PtC began at -0.05V. Also, samples 700 and 800˚C have an oxygen reduction peak at -0.4V. This figure determined that the optimized pyrolysis temperature can improve electrocatalytic activity. The second reduction peak in the PtC sample at -0.4V is related to Pt-O reduction. The third reduction peak in the PtC sample at -0.7V is related to Pt-H formation (H adsorption) [184]. The last reduction peak at -0.9V for the PtC sample is related to the hydrogen evolution reaction [184]. Three peaks at -0.96, -0.69, and -0.6V are related to H_2 desorption [184]. The fourth oxidation peak at -

0.17V is related to Pt oxidation and the last peak at -0.65V is related to the oxygen evolution reaction [184]. The MOF samples have a Cu oxidation peak at -0.1V and an oxygen evolution reaction at -0.6V. The 1000˚C sample has an ORR peak at -0.1V and, the 700 and 800˚C samples have an ORR peak at -0.3V. These three MOF samples have a peak at -0.7V which is related to hydrogen adsorption. The sharp peak of MOF samples at -0.9V is related to the hydrogen evolution reaction.

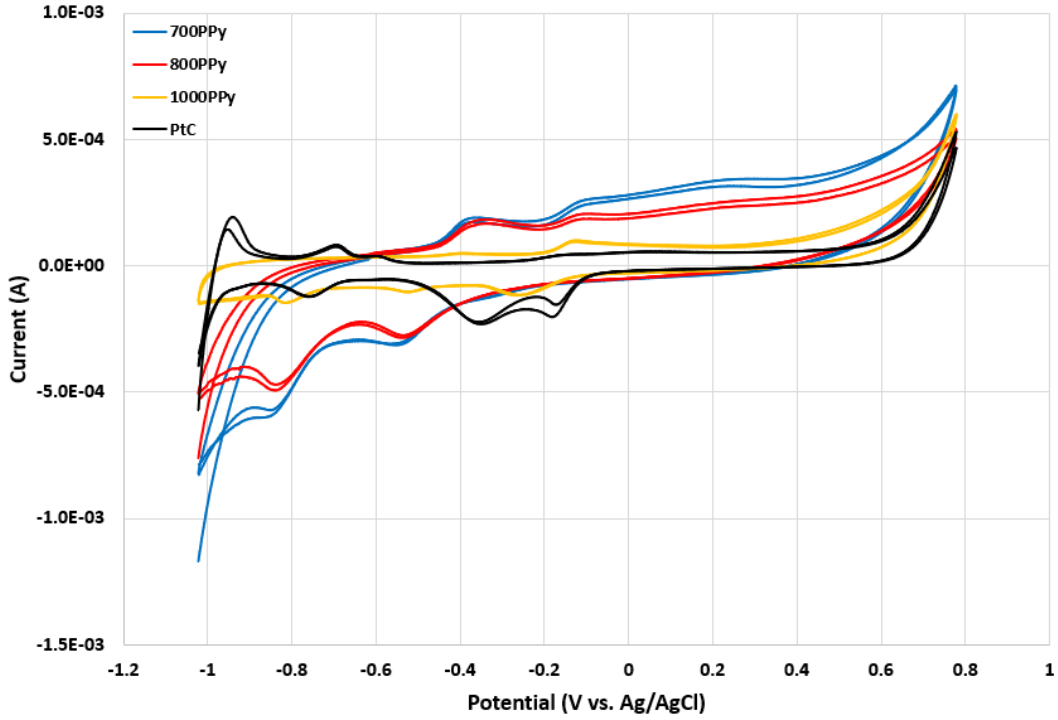

Figure 39: The cyclic voltammogram in 10 mVs^{-1} of PtC and PPy-coated HKUST MOF that pyrolyzed at 700, 800, and 1000˚C in O_2-saturated electrolyte.

As mentioned, the aerated electrolytes have been used for the ORR analysis. The CV results in a scan rate of 10 $mV.s^{-1}$ for PtC and PPy-coated HKUST MOF that pyrolyzed at 700˚C are reported in Figures 40 and 41, respectively. The CV voltammograms in

Figures 40 and 41 are reported in O_2-saturated and N_2-saturated KOH electrolytes. For this purpose, the electrolyte was aerated by a compressed air tank and nitrogen tank respectively. According to Figures 38 and 39, the dissolved oxygen in the electrolyte (aeration process) increases the ORR peak's intensity for both PtC and MOF samples.

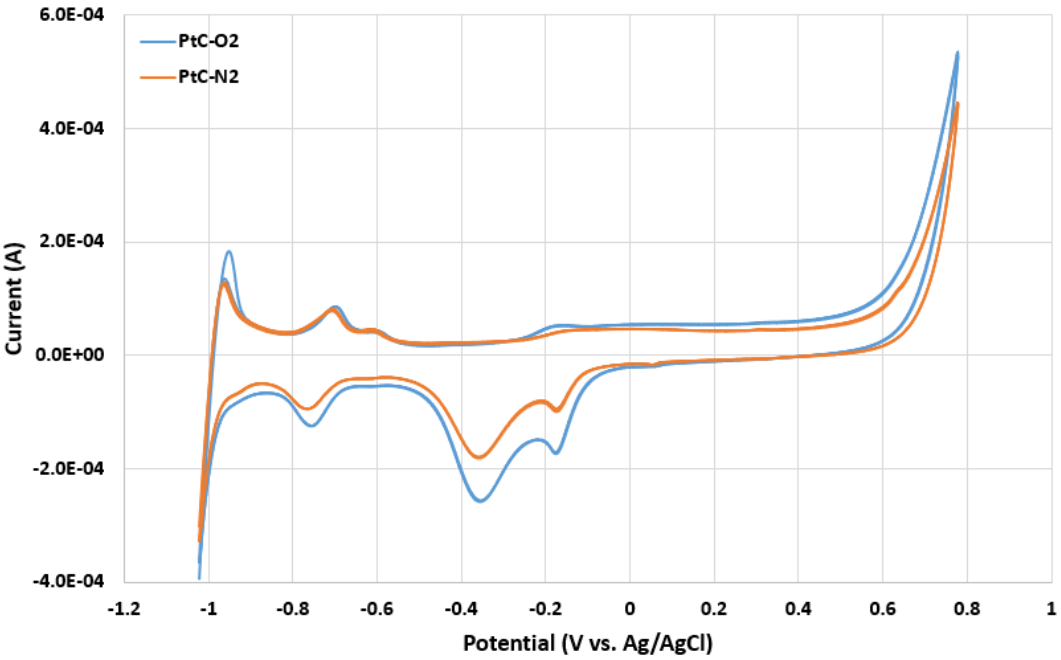

Figure 40: The cyclic voltammogram in 10 mVs^{-1} of PtC in O_2-saturated and N_2-saturated KOH electrolyte.

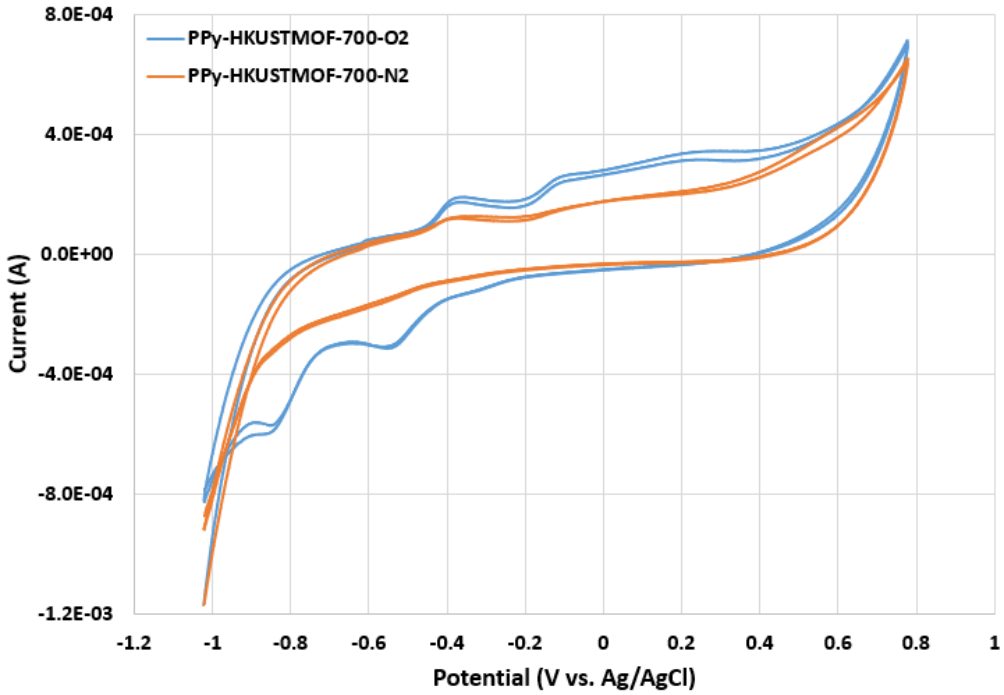

Figure 41: The cyclic voltammogram in 10 mVs^{-1} of PPy-coated HKUST MOF that pyrolyzed at 700˚C in O_2-saturated and N_2-saturated KOH electrolyte.

3.2.3 Electrochemical Analysis of ZIFs

The CV voltammograms of three prepared Carbon_ZIFs including Carbon_CoZIF, Carbon_FeZIF, Carbon_CoFeZIF, and PtC are illustrated in Figure 42. There is a small peak at 0.15V in Carbon_CoZIF and Carbon_CeFeZIF samples which is related to the reduction of cobalt. The oxygen reduction peak in CoZIF and CoFeZIF started at -0.06V, even earlier than PtC as the standard sample. This is a considerable result for two samples that contain no precious metals like Pt. The CV voltammogram of FeZIF has lower activity than the other samples, but the results for CoZIF and CoFeZIF are satisfying. Therefore, carbon from ZIFs can be an exciting option for ORR electrocatalysts.

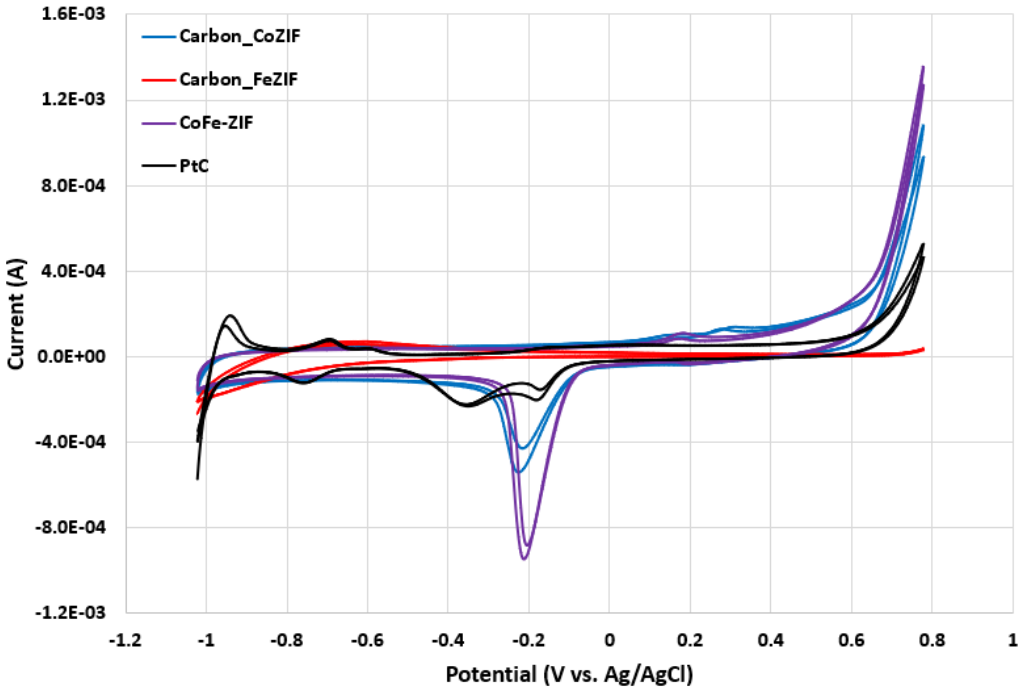

Figure 42: The cyclic voltammogram in 10 mVs^{-1} of PtC and three prepared Carbon_ZIFs that pyrolyzed at 800˚C in O_2-saturated electrolyte.

The LSV graphs of these three ZIF and PtC are reported in Figure 43. Like Figure 42, the electrochemical activity of CoZIF and CoFeZIF is slightly better than PtC and the ORR reduction peak starts earlier than the PtC sample. The ORR activity of Carbon_FeZIF is weaker than the other samples because it starts at -0.4V. There is a small peak at 0.15V in Carbon_CoZIF and Carbon_CeFeZIF samples which is related to the reduction of cobalt. The oxygen reduction peak of Carbon_CoZIF and Carbon_CeFeZIF samples starts at -0.06V (a little prior than PtC).

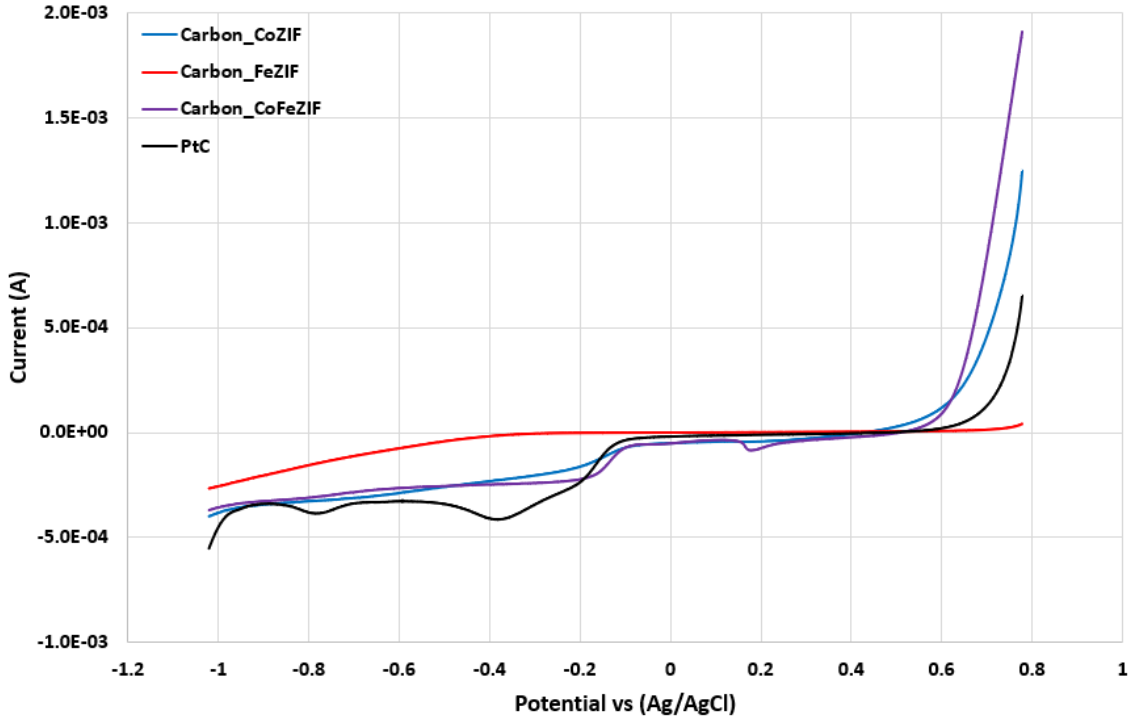

Figure 43: The LSV voltammogram in 1600 rpm of PtC and three prepared Carbon_ZIFs that pyrolyzed at 800˚C in O_2-saturated electrolyte.

3.2.4 Stability Analysis of MOFs and ZIFs

Another critical parameter of the electrocatalysts is the electrocatalyst stability within the range applied during the electrode operation. The previous section dealt with the electrochemical performance of the electrocatalysts derived from MOFs and ZIFs in the first cycle. But more than the first cycle analyses are needed to determine the quality of electrocatalysts [185,186]. Therefore, the stability of the samples in 1456 cycles is analyzed. This cycle number is the maximum number that the device used in this project can be saved. The stability analysis of PPy-coated HKUST MOF that pyrolyzed at 600, 700, 800, 900, 1000, and 1100˚C is illustrated in Figure 44. The cyclic stability means decreasing in current magnitude on CV scans by comparing the first and the last CV cycles. The sample that pyrolyzed at 700˚C initially has a higher current because it has a

higher activated surface than other samples. These samples do not have enough cyclic stability. It means the pyrolyzed PPy-coated HKUST MOF can not be considered a durable ORR electrocatalyst. The lack of cyclic stability of the electrocatalysts derived from MOF samples related to the phase separation of Cu in the pyrolysis process. Several electrochemical sweeps led to the leaching of Cu and Cu(II)O from the electrode surface. This fast leaching expedited the detachment of carbon electrocatalysts from the RDE surface.

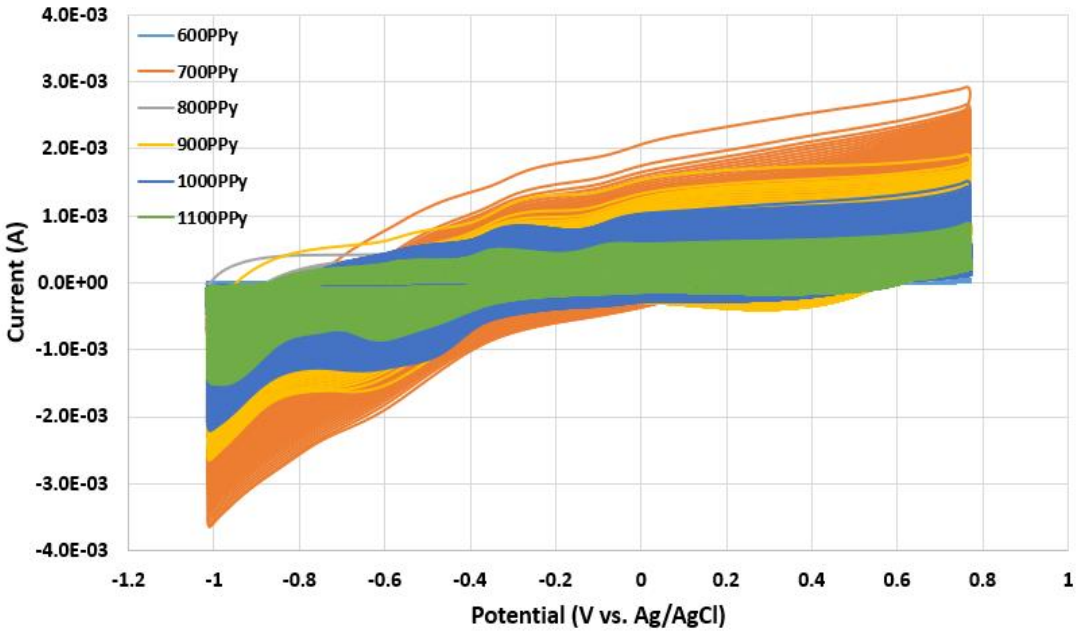

Figure 44: The cyclic stability in 100 mVs^{-1} of PPy-coated HKUST that pyrolyzed at 600, 700, 800, 900, 1000, and 1100˚C in O_2-saturated electrolyte.

The cyclic stability of PtC compared with PPy-coated HKUST MOF that pyrolyzed at 700˚C in Figure 45. The PtC sample after 1456 cycles is more stable than all PPy-coated HKUST MOF samples.

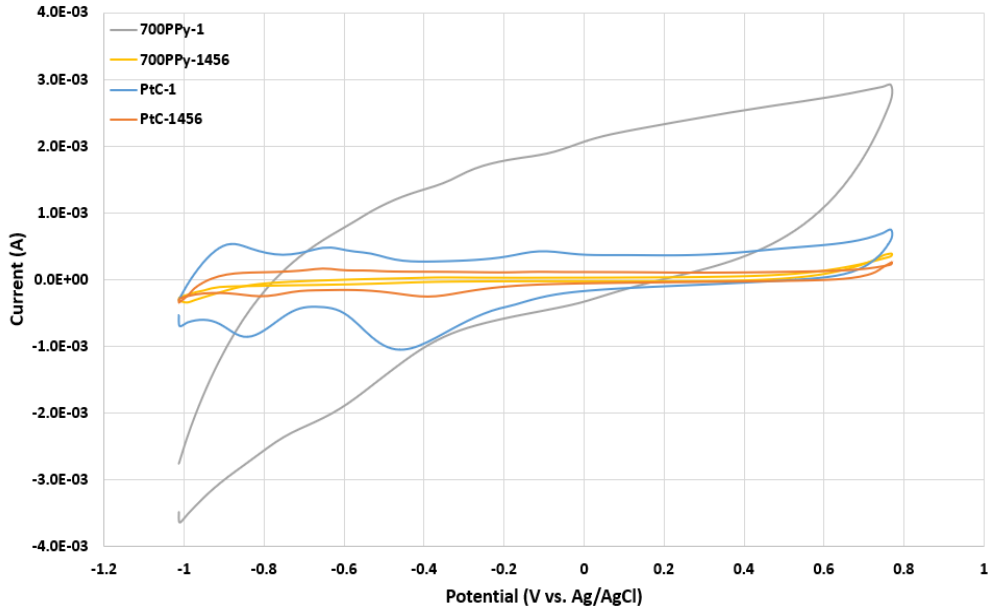

Figure 45: The cyclic stability at 100 mVs^{-1} in first and 1456 cycles of PtC and PPy-coated HKUST that pyrolyzed at 700˚C in O_2-saturated electrolyte.

The cyclic stability analysis of PtC and three pyrolyzed Carbon_ZIFs is illustrated in Figure 46. The cyclic stability of pyrolyzed ZIFs at 800˚C is higher than MOFs. The stability of pyrolyzed FeZIF at 800˚C (like pyrolyzed MOFs) is very low after 1456 cycles. The cyclic stability of CoZIF is better than FeZIF. The hybrid CoFeZIF has even higher cyclic stability than the PtC sample. The electrochemical performance of CoZIF and CoFeZIF in the first cycle is close to the PtC sample. Also, the electrochemical performance of CoFeZIF after 1456 cycles is even better than the PtC sample. Hence, the hybridization of Co and Fe in carbon structure has a synergetic improvement that improves electrochemical properties even better than the PtC sample. Also, the CV voltammogram of PtC and Carbon_CoFeZIF at first and 1456 cycles are reported in Figure 47. The Carbon_CoFeZIF sample has a higher current magnitude than the PtC sample after 1456 cycles. The Carbon_CoFeZIF has two reduction peaks at 0.5V and

0.15V which are related to the reduction of Fe and Co respectively. Both Carbon_CoZIF and Carbon_CoFeZIF have oxygen reduction peaks that start at about -0.1V. There are two reduction peaks for the PtC sample at -0.5V and -0.85V that are related to the reduction of oxygen and hydrogen adsorption on the electrocatalyst surface by forming Pt-H [187].

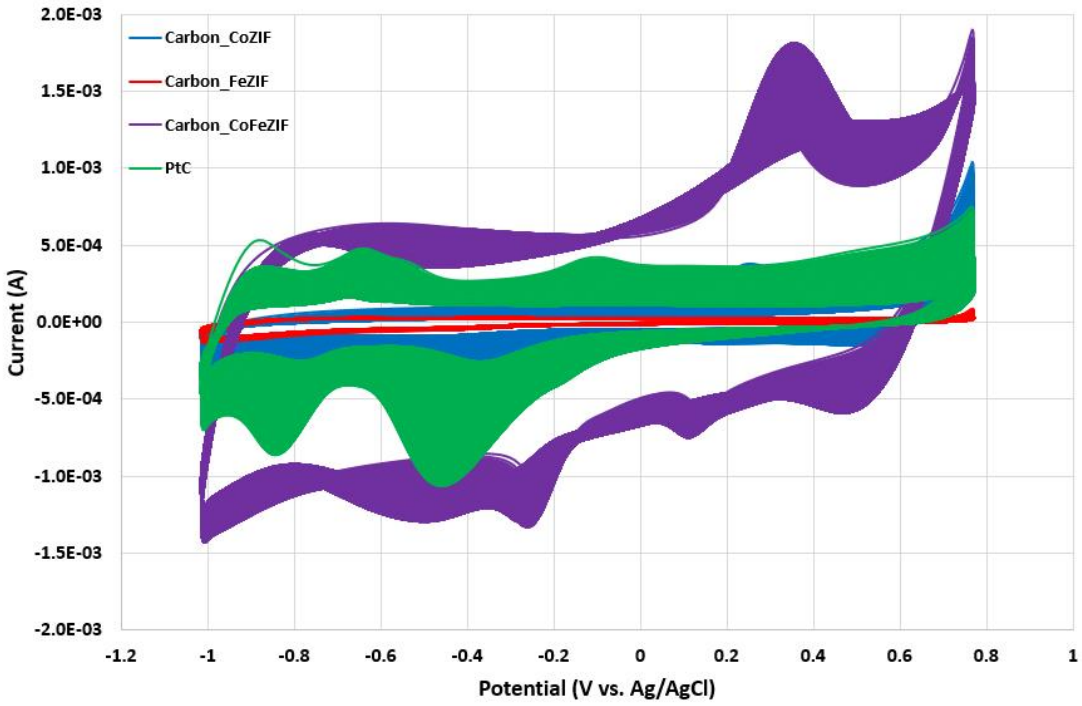

Figure 46: The cyclic stability in 100 mVs^{-1} of PtC and three prepared Carbon_ZIFs that pyrolyzed at 800˚C in O_2-saturated electrolyte.

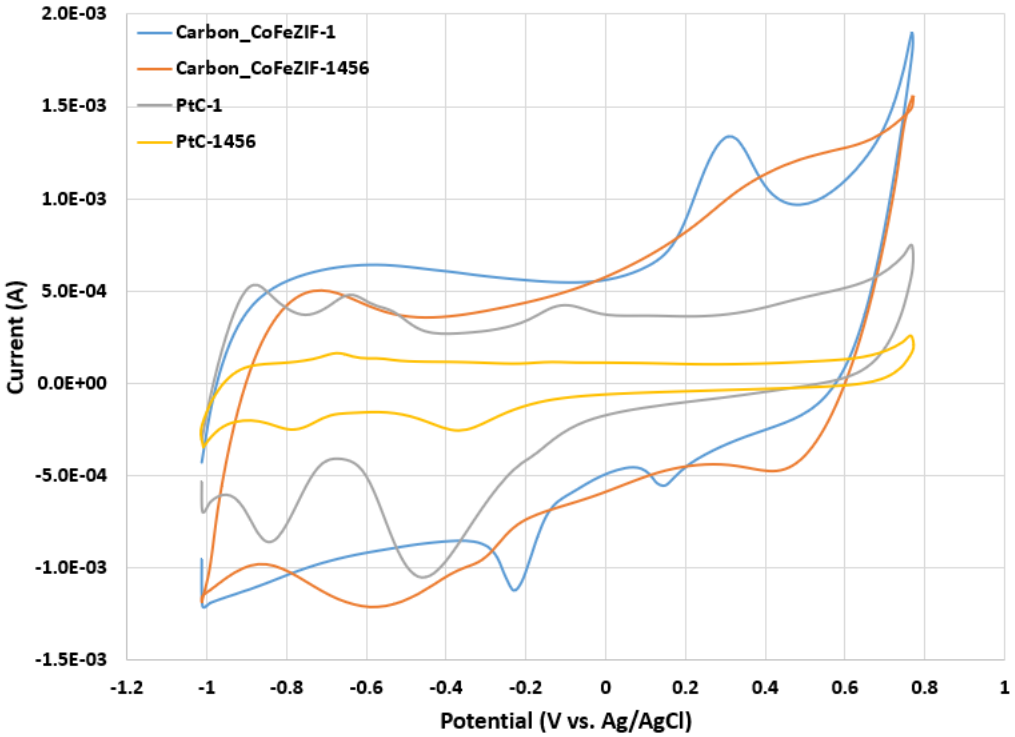

Figure 47: The first and 1456th voltammogram cycles in 100 mVs^{-1} of PtC and Carbon_CoFeZIF that pyrolyzed at 800˚C in O_2-saturated electrolyte.

The ORR analyses of ZIFs were performed in an O_2-saturated KOH electrolyte like what was performed for MOF samples. The influence of the electrolyte aeration on the ORR performance of Carbon_CoFeZIF is illustrated in Figure 48. According to Figure 48, the O_2-saturated electrolyte has an ORR peak with a higher current magnitude. It means using O_2-saturated electrolyte improved the ORR performance.

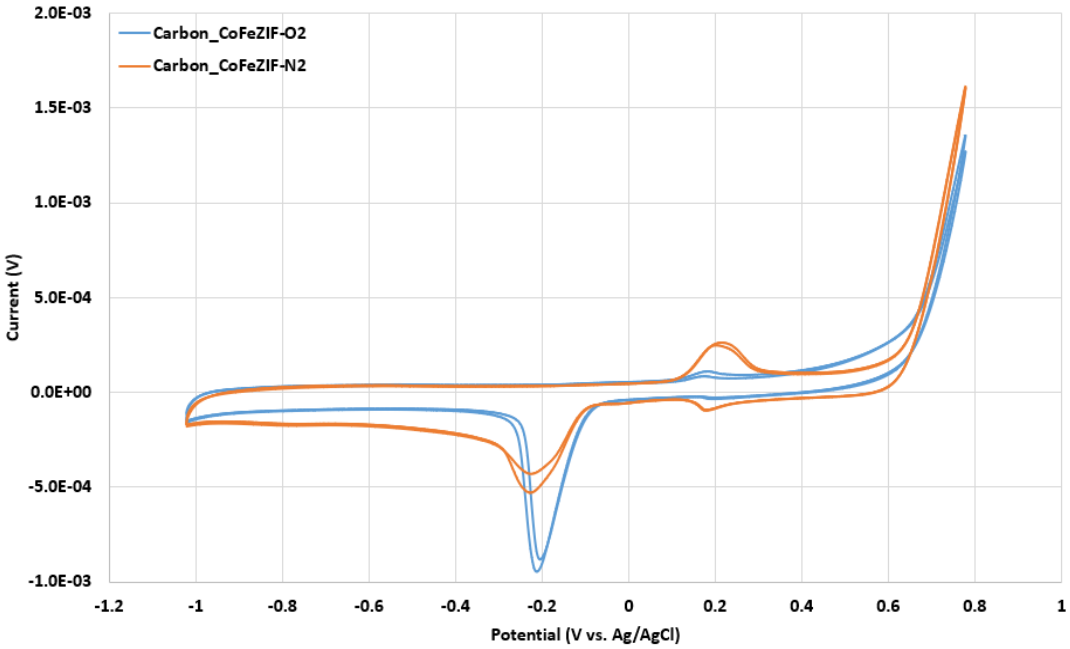

Figure 48: The cyclic voltammogram in 10 mVs^{-1} of Carbon_CoFeZIF that pyrolyzed at 800˚C in O_2-saturated and N_2-saturated KOH electrolyte.

3.2.5 Oxygen Evolution Reaction of MOFs and ZIFs

The OER is essential for rechargeable MABs. Ruthenium oxide (RuO_2) is a standard OER process electrocatalyst with the highest OER performance [188]. The OER of PPy-coated HKUST MOFs were pyrolyzed at different temperatures as illustrated in Figure 49. The turning point of the graphs (onset potential) in Figure 49 is reported in Table 2. RuO_2 has the best OER performance (onset potential at 0.42 V), and the MOF sample that pyrolyzed at 600C has the lowest OER performance (onset potential at 1.35 V). Other pyrolyzed MOF samples have OER performance very close to PtC and the MOF sample that pyrolyzed at 900˚C has better performance than the PtC sample. But still, the OER performance of PPy-coated HKUST MOF is lower than RuO_2 as a standard OER electrocatalyst.

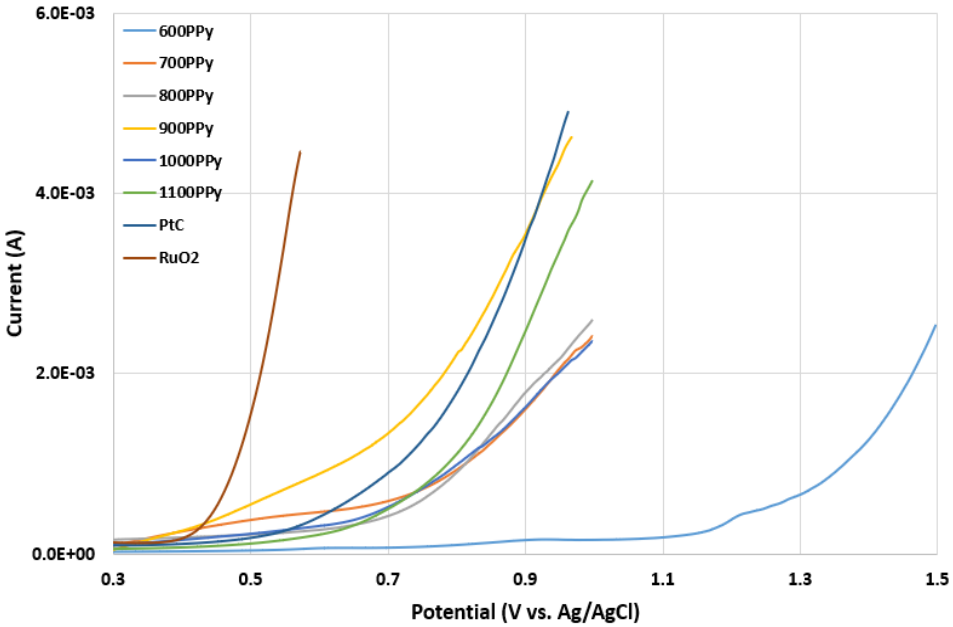

Figure 49: The OER in 10 mVs^{-1} of RuO_2, PtC, and PPy-coated HKUST MOF that pyrolyzed in 600, 700, 800, 900, 1000, and 1100˚C.

Table 2. The onset potential of the OER graph of RuO_2, PtC, and PPy-coated HKUST MOF that pyrolyzed in 600, 700, 800, 900, 1000, and 1100˚C.

Sample	600PPy	700PPy	800PPy	900PPy	1000PPy	1100PPy	PtC	RuO_2
Onset potential (V)	1.35 ±0.05	0.80 ±0.04	0.73 ±0.04	0.75 ±0.03	0.80 ±0.04	0.78 ±0.04	0.75 ±0.03	0.42 ±0.02

Also, the OER performance of the pyrolyzed ZIFs at 800˚C was analyzed and reported in Figure 50. The onset potentials in Figure 50 are reported in Table 3. Carbon_FeZIF has the lowest OER performance (onset potential at 0.78 V), and RuO_2 has the best (onset potential at 0.42 V). The OER performance of Carbon_CoFeZIF is between Carbon_CoZIF and Carbon_FeZIF. According to Figure 50, Carbon_CoZIF has the best OER result among the three prepared ZIFs.

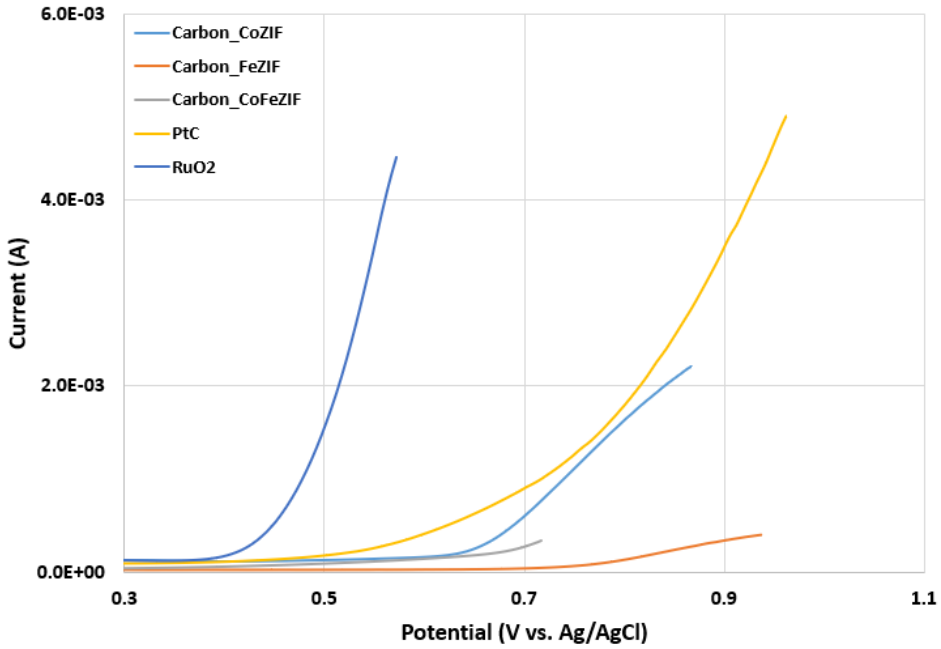

Figure 50: The OER in 100 mVs^{-1} of PtC and three prepared Carbon_ZIFs that pyrolyzed at 800˚C.

Table 3. The onset potential of the OER graph of RuO_2, PtC, and Carbon_ZIFs that pyrolyzed at 800˚C.

Sample	CoZIF	FeZIF	CoFeZIF	PtC	RuO_2
Onset potential (V)	0.67 ±0.03	0.78 ±0.04	0.69 ±0.03	0.75 ±0.03	0.42 ±0.02

3.2.6 The Bifunctional Performance of MOFs and ZIFs

The bifunctional oxygen electrocatalyst has acceptable ORR and OER performance. It means the ORR performance of a bifunctional electrocatalyst must be close to PtC performance, and the OER performance must be close to RuO_2 performance. The bifunctional potential (ΔE) values of the prepared MOFs and ZIFs are listed in Table 4.

The ideal bifunctional oxygen electrocatalysts have the smallest ΔE value. The ΔE values for Carbon_CoZIF and Carbon_CoFeZIF are smaller than all MOF samples. It determined the better bifunctional performance of the ZIF samples over MOF samples. The ΔE value of CoFeZIF (0.78 V) is even smaller than standard PtC (0.85 V). Carbon_CoFeZIF has the best bifunctional electrocatalytic performance among all samples of this project. The presence of Co in Carbon_CoZIF and Co/Fe in Carbon_CoFeZIF improves their bifunctional potential.

Table 4. The bifunctional potential of the prepared MOFs and ZIFs.

Sample	Sample code	ΔE (V)
PPy-coated HKUST MOFs	PPy-coated HKUST MOF-600˚C	1.7
	PPy-coated HKUST MOF-700˚C	1
	PPy-coated HKUST MOF-800˚C	0.93
	PPy-coated HKUST MOF-900˚C	1.1
	PPy-coated HKUST MOF-1000˚C	1.05
	PPy-coated HKUST MOF-1100˚C	1.13
ZIFs	Carbon_CoZIF-800˚C	0.765
	Carbon_FeZIF-800˚C	1.17
	Carbon_CoFeZIF-800˚C	0.78
Standard Platinum	PtC	0.85

3.2.7 Kinetic Analysis of MOFs and ZIFs

The LSV analysis is performed in different rotations (400, 900, 1600, and 2500 rpm) to control the diffusion influence on the electrochemical performance of the samples. The previous studies calculated the number of electrons by the LSV analysis in different rotations and the K-L equation (equation 12) [65,189]. As is obvious in the following Figures, the rotation rate can control the ORR performance and O_2 diffusion to the electrocatalyst surface. The electrode rotation provided a diffusion-convection layer near the electrocatalyst surface. Increasing the rotation rate increases the convection current, allowing the physical movement of reactants and products to flow around the electrode.

With an increasing convection rate, the limiting current density is increased, meaning the maximum current density the electrocatalyst can reach is increased, due to the reaction being able to occur more quickly [190]. By performing LSV under hydrodynamic conditions, the rate of electron transfer between the electrode and electrolyte interface can be understood and used to assess the kinetics and mass transfer effects. The LSV profiles were recorded using a RDE electrode to determine the kinetics ORR at various electrode rotation rates and a fixed scan rate [14]. The solution movement away from the disc caused by electrode rotating might result in vacuum formation at the disc center, causing more electroactive ions to be attracted from the bulk solution towards the electrode surface [14].

The LSV curves of PtC are illustrated in Figure 51. Also, PPy-coated HKUST MOF that pyrolyzed at 700˚C and 800˚C are illustrated in Figures 52 and 53 respectively. As is obvious in the following figures, the rotation rate influences the oxygen diffusion to the electrocatalyst surface. Oxygen diffusion depends on the rotation rate of RDE. The number of electrons determines the ORR pathways ($2e^-$or $4e^-$). The number of electrons in the ORR mechanism can be calculated by calculating the current density of different rotation rates at one specific potential. The selected potentials need to have a constant distance between each rotation [191]. Otherwise, the next step will not be linear. For example, the current densities of different rotations need to be reported at -0.22 V, -0.25 V, and -0.3 V for the PtC sample. The obtained data for each potential will draw which will provide a linear line. This process should be reported for -0.22 V, -0.25 V, and -0.3 V for the PtC sample. Then, the slope and intercept of these lines will be used in the K-L calculation (equation 14) to find the number of electrons (n) in the ORR process. This

calculation as one of the future works of this project will be completed in the next step of the project.

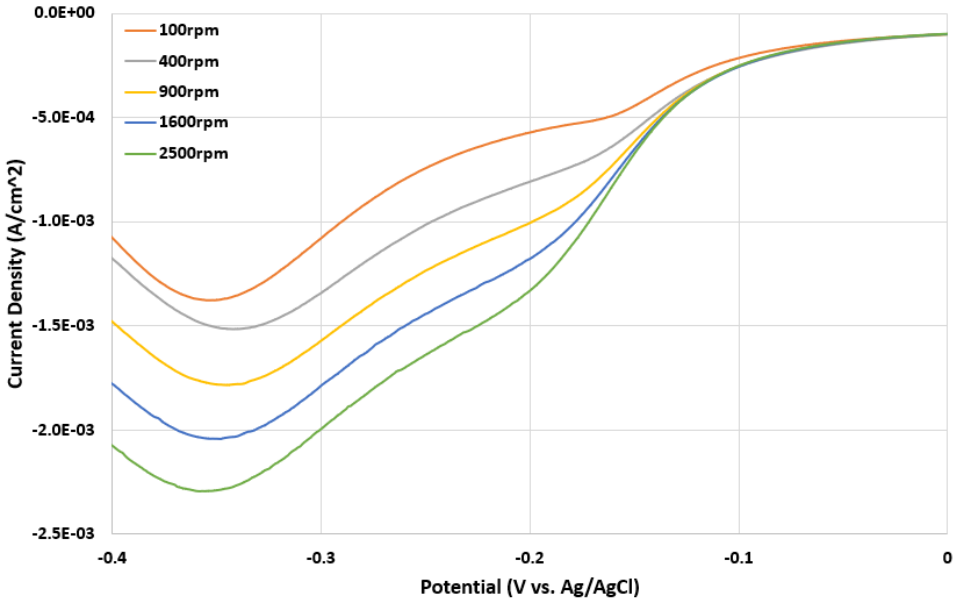

Figure 51: The LSV analyses in 10 mVs^{-1} of PtC in different rotations (100, 400, 900, 1600, and 2500 rpm).

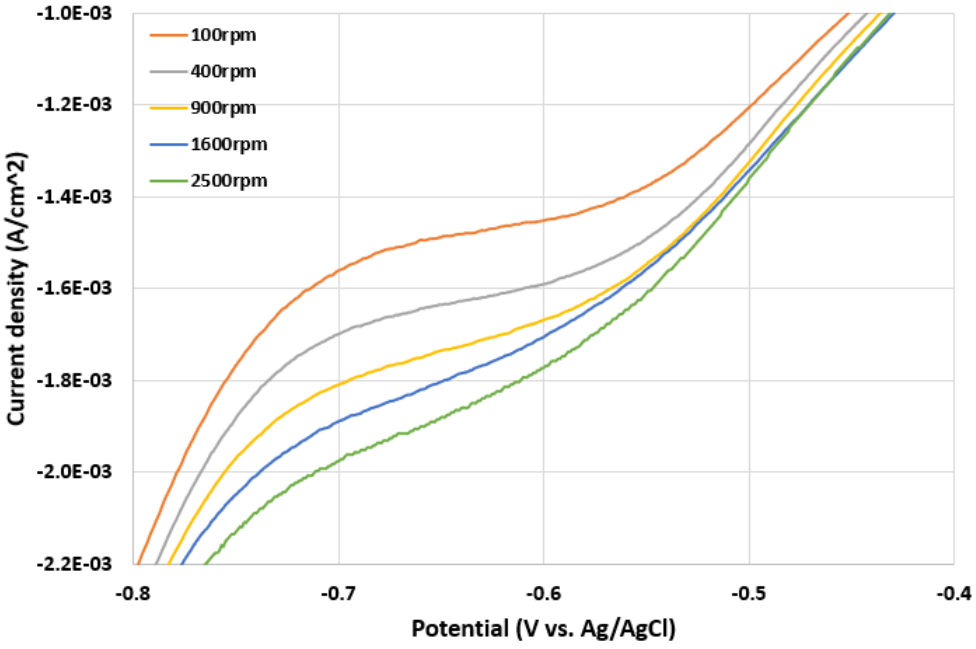

Figure 52: The LSV analyses in 10 mVs^{-1} of PPy-coated HKUST MOF that pyrolyzed at 700˚C in different rotations (100, 400, 900, 1600, and 2500 rpm).

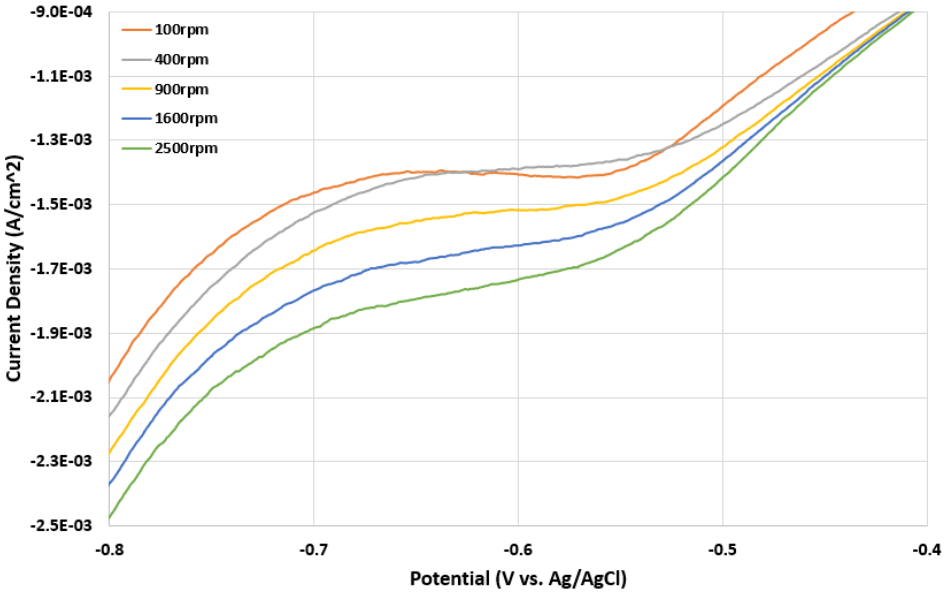

Figure 53: The LSV analyses in 10 mVs^{-1} of PPy-coated HKUST MOF that pyrolyzed at 800˚C in different rotations.

The L-S analysis of Carbon_CoZIF and Carbon_CoFeZIF in different rotations are illustrated in Figures 54 and 55 respectively. The small peak at 0.2V in Carbon_CoZIF is related to the Co reduction. The peak at 0.15V in Carbon_CoFeZIF is related to the Co and Fe reduction.

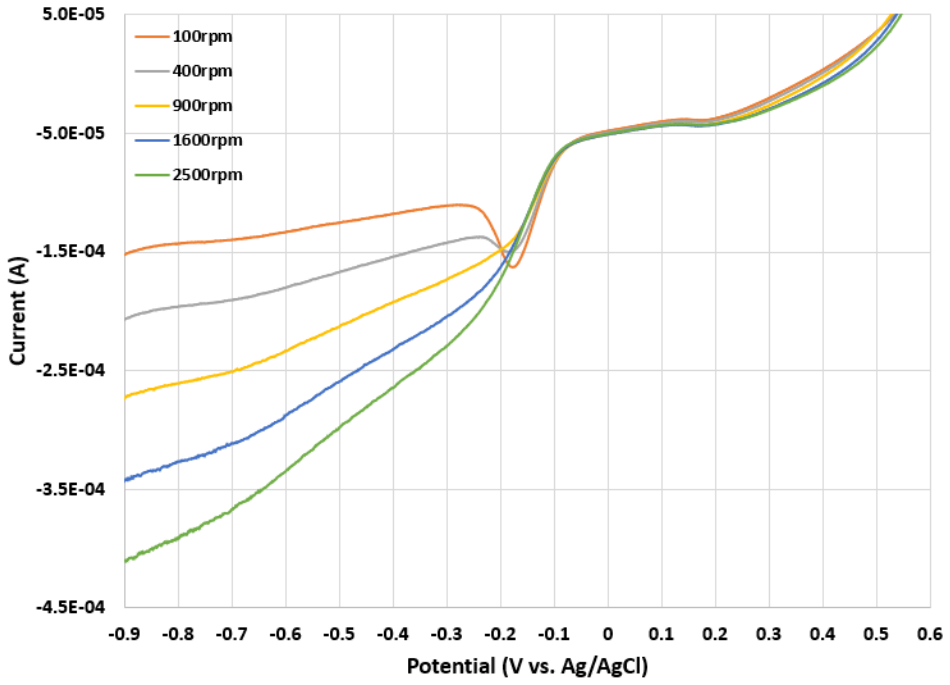

Figure 54: The LSV analyses in 10 mVs^{-1} of Carbon_CoZIF that pyrolyzed at 800˚C in different rotations.

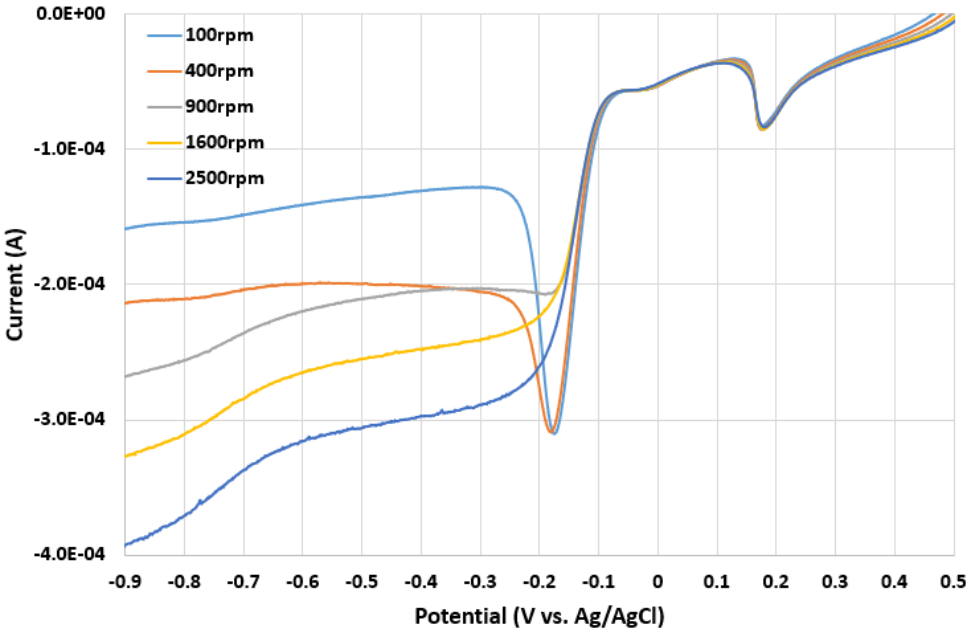

Figure 55: The LSV analyses in 10 mVs^{-1} of Carbon_CoFeZIF that pyrolyzed at 800˚C in different rotations.

4.0 Discussion

Different characterization methods were used to analyze the samples before and after pyrolysis. The characterization of the samples before pyrolysis including ATR-IR and XRD confirmed the synthesis methods. According to the ATR-IR spectra, the pyrolyzed samples have less functional groups than the samples before pyrolysis because the peak intensities for the pyrolyzed samples were much lower than samples before pyrolysis. It indicates the carbonization process leads to a considerable reduction in the functional groups in the samples. Also, the XRD patterns of HKUST MOF and CoZIF were similar to the literature which confirmed their synthesis method. The ATR-IR spectra of the samples after pyrolysis determined the formation of graphene oxide. Also, the XRD patterns of the pyrolyzed samples illustrated the formation of graphene oxide and graphene. It means the pyrolysis of these samples led to the formation of graphene oxide and graphene. Graphene-like carbon materials are considered the main product of the pyrolysis of the carbon-based materials [192]. The SEM image of the PPy-coated HKUST MOF verified the sedimentation of PPy particles on the MOF surface [109]. Also, the SEM images of the ZIF samples (before and after pyrolysis) illustrated their porous structures [193]. The EDX-mapping of the pyrolyzed samples determined the distribution of metal and nitrogen in the samples (especially for Carbon_ZIF samples). Both XRD and SEM determined the existence of the amorphous structures in the samples. The SEM images of the pyrolyzed samples determined their porosity. It determined the pyrolysis of MOFs and ZIFs (especially ZIFs) can provide doped-carbon structures. The electrochemical analyses including CV and LSV determined the superior electrochemical performance of the Carbon_ZIFs over pyrolyzed MOFs. The CV and LSV voltammograms of the

Carbon_ZIFs were more similar to PtC voltammograms than pyrolyzed MOF samples. The higher activity of the Carbon_ZIFs is related to the covalent C-N bonds while the PPy just sedimented on the HKUST MOF with weaker physical interactions. The PPy-coating (with physical interactions) could not provide N-doping as imidazole in the ZIF structures (with covalent bonds). Hence, Carbon_ZIFs have more capability to preserve their N-content in the pyrolysis process over PPy-coated HKUST MOF. Also, the stability of the Carbon_ZIFs is higher than the pyrolyzed MOF samples. It determined the Carbon_ZIFs have better electrocatalytic performance and cyclic stability. The OER analysis of the samples by LSV technique determined more modifications should be done to achieve better OER activity. The CV results determined that Carbon_CoZIF and Carbon_CoFeZIF have ORR peaks close to the ORR peak of PtC. The LSV results determined that Carbon_CoZIF and Carbon_CoFeZIF have ORR peaks close to the ORR peak of PtC in different rotation rates. The cyclic stability results determined that Carbon_CoZIF and Carbon_CoFeZIF have cyclic stability which can compete with the cyclic stability of PtC in 1456 cycles. The OER onset potentials of pyrolyzed MOF and Carbon_ZIFs were close to the OER onset potential of PtC. However, none of the samples can compete with RuO_2 as the standard OER sample. Hence, more modifications should be done to obtain better OER performance. The ΔE value as a bifunctional parameter can determine the overall performance of an oxygen electrocatalyst for ORR and OER reactions. The lower ΔE indicates the higher activity of an oxygen electrocatalyst. The ΔE contents of the Carbon_ZIFs are lower than the pyrolyzed MOF samples. Also, the ΔE contents of Carbon_CoZIF and Carbon_CoFeZIF were slightly lower than PtC as a standard sample. It determined that Carbon_CoZIF and

Carbon_CoFeZIF as low-cost electrocatalysts have a potential to compete with standard commercial oxygen electrocatalysts. Based on all characterization and electrochemical properties, Carbon_CoZIF and Carbon_CoFeZIF as the two best samples of this thesis should be further developed for scale-up production.

5.0 Conclusion

The ORR and OER have an undeniable role in the MABs and FCs. The low-cost and high-performance ORR and OER electrocatalysts have been widely developed to provide better electrochemical performance. A chemical reaction between BTC and CuN has prepared the HKUST MOF. Then, HKUST MOF was coated by PPy. The pyrolyzed PPy-coated HKUST MOF as nitrogen-doped carbon has ORR and OER activity. The ORR performance of PPy-coated HKUST MOF that pyrolyzed at 700 and 800˚C is -0.3V and close to PtC ORR performance (-0.1V). The pyrolyzed MOF samples have no cyclic stability after 1456 cycles. The ORR performance of pyrolyzed ZIFs (-0.1V) is better than pyrolyzed MOFs and closer to PtC. Also, the cyclic stability of CoZIF is even better than PtC. The OER performance of PPy-coated HKUST MOF that pyrolyzed at 900˚C is slightly better than the PtC sample. The OER performance of Carbon_CoZIF is close to the PtC sample. The pyrolyzed hybrid ZIF at 800˚C that contained Co and Fe can be considered an appropriate bifunctional electrocatalyst (ΔE = 0.80V). The bifunctional potential as the bifunctional performance of Carbon_CoFeZIF is even better than the PtC sample. It determined that Carbon_CoFeZIF, which costs about three percent of platinum, has better cyclic stability and bifunctional electrocatalytic performance. Carbon_CoZIF and Carbon_CoFeZIF as the two best samples of this project that have contained the highest overall electrochemical parameters, including cyclic stability in 1456 cycles, ORR performance, OER performance, and ΔE overpotential can be considered as bifunctional oxygen electrocatalysts for MABs and FCs.

6.0 Future Work

6.1 Thermal Optimization of ZIF-based Electrocatalysts

The ZIFs were pyrolyzed at 800˚C. The pyrolysis temperature has a considerable influence on the electrochemical performance of carbons. Therefore, one of the future works can be the thermal optimization of ZIF-based electrocatalysts via pyrolysis in different temperatures (600, 700, 800, 900, 1000, and 1100˚C). In this project, Carbon_ZIFs were prepared at 800˚C. CoZIF and CoFeZIF should be pyrolyzed at different temperatures (600, 700, 900, 1000, and 1100˚C).

6.2 Synthesis Optimization of ZIF-based Electrocatalysts

In this project, the ratio of Co and Fe for the synthesis of CoFeZIF was (1:1). This ratio should be optimized by analysis of different ratios of Co/Fe, such as (1:2) and (2:1). Then, the electrochemical properties of new Carbon_CoFeZIF samples with different metal ratio should be compared with the current Carbon_CoFeZIF sample. Also, the metal nitrate to MIM ratio was (1:2). This ratio was used in previous publications to prepare CoZIF (ZIF-67) [194,195]. It is essential to find this metal/MIM ratio to enhance the electrochemical performance.

6.3 Explore Other Metals for ZIF-based Electrocatalysts

In this project, CoZIF, FeZIF, and CoFeZIF were prepared. Carbon_CoZIF and Carbon_CoFeZIF had the best ORR, OER, and cyclic stability results. The other hydrated metal nitrates can be analyzed and compared with Carbon_CoFeZIF results. Other low-cost hydrated metal nitrates such as chromium (III) nitrate, manganese (II) nitrate, nickel (II) nitrate, and zinc (II) nitrate hexahydrate should be developed to find different doped

metals in the carbon structure. Also, new hybrid ZIFs similar to Carbon_CoFeZIF can be developed in future projects to find novel hybrid ZIFs with better electrocatalytic performance.

6.4 Economical Analyses of the Industrial Production of ZIFs

In this project, Carbon_CoFeZIF and Carbon_CoZIF had the best electrocatalytic performance. The next step will be to fabricate this bifunctional electrocatalyst on a large scale. This electrocatalyst scale-up is another project that may follow in the future. Fortunately, hydrated metal nitrates have low costs. For example, the price of 1Kg of some hydrated metal nitrates like iron (III) nitrate nonahydrate 99.95% Sigma-Aldrich (175 USD), cobalt (II) nitrate nonahydrate 99.0% Fisher Scientific (258 USD) indicated the amazing economical potential of ZIFs to be used as bifunctional oxygen electrocatalysts precursor.

6.5 Computational Analyses to Evaluate the Structure of Carbon_ZIFs

In this project, Carbon_CoFeZIF and Carbon_CoZIF had the best electrocatalytic results. But still, their structures should be more evaluated by density functional theory (DFT) to determine the mechanism for ORR and OER processes. For example, the OER mechanism (AEM/LOM) of the samples especially Carbon_CoZIF and Carbon_CoFeZIF should be analyzed in the next study. Also, the number of electrons in ORR analysis can be calculated by the K-L equation to determine the type of ORR (2-electron or 4-electron systems).

The other future project through computational study can be the analysis of different doping atoms in the Carbon_ZIFs. For example, different types of nitrogen including graphitic nitrogen, pyridinic nitrogen, pyrrolic nitrogen, and pyrazole nitrogen in the carbon structure can improve the ORR/OER performance. The N-doped carbon structure can be analyzed by XPS and computational study [196,197]. Therefore, the Carbon_ZIFs should be analyzed by both XPS and computational methods to determine the type of carbon-nitrogen bonds.

7.0 References

1 M. Mutarraf, Y. Guan, L. Xu, C. L. Su, J. Vasquez and J. Guerrero, *Sustain. Energy Technol. Assessments*, 2022, **52**, 102177.

2 H. Cruz-Martínez, H. Rojas-Chávez, P. Matadamas-Ortiz, J. Ortiz-Herrera, E. López-Chávez, O. Solorza-Feria and D. Medina, *Mater. Today Phys.*, , DOI:10.1016/j.mtphys.2021.100406.

3 C. Vilela, A. J. D. Silvestre, F. M. L. Figueiredo and C. S. R. Freire, *J. Mater. Chem. A*, 2019, **7**, 20045–20074.

4 T. M. Huggins, J. J. Pietron, H. Wang, Z. J. Ren and J. C. Biffinger, *Bioresour. Technol.*, 2015, **195**, 147–153.

5 B. Wang, E. Ang, Y. Yang, Y. Zhang, M. Ye, Q. Liu and C. Li, *Chem. – A Eur. J.*, 2021, **27**, 512–536.

6 J.-Y. Hwang, S.-T. Myung and Y.-K. Sun, *Chem. Soc. Rev.*, 2017, **46**, 3529–3614.

7 Y. Chen, J. Xu, P. He, Y. Qiao, S. Guo, H. Yang and H. Zhou, *Sci. Bull.*, 2022, **67**, 2449–2486.

8 J.-S. Lee, S. Tai Kim, R. Cao, N.-S. Choi, M. Liu, K. T. Lee and J. Cho, *Adv. Energy Mater.*, 2011, **1**, 34–50.

9 N. Javed, T. Noor, N. Iqbal and S. Naqvi, *RSC Adv.*, 2023, **13**, 1137–1161.

10 J. Zhang, H. Zhang, Y. Zhang, X. Wang, H. Li, F. Feng, K. Wang, G. Zhang, S. Sun and Y. Zhang, *J. Mater. Chem. A*, 2023, **11**, 7924–7948.

11 T. Narins, *Extr. Ind. Soc.*, 2017, **4**, 321–328.

12 Z. Meng, N. Chen, S. Cai, R. Wang, J. Wu and H. Tang, *Mater. Chem. Front.*, 2021, **5**, 2649–2667.

13 Z. Liu, Z. Deng, S. Davis, C. Giron and P. Ciais, *Nat. Rev. Earth Environ.*, 2022, **3**, 217–219.

14 N. Bhuvanendran, S. Ravichandran, Q. Xu, T. Maiyalagan and H. Su, *Int. J. Hydrogen Energy*, 2022, **47**, 7113–7138.

15 Z. Han, J. J. Feng, Y. Q. Yao, Z. G. Wang, L. Zhang and A. J. Wang, *J. Colloid Interface Sci.*, 2021, **590**, 330–340.

16 S. Chen, X. Liu, H. Sun, Z. Cao, J. Xiong and Y. Li, *J. Alloys Compd.*, 2022, **897**, 163203.

17 F. Besharat, F. Ahmadpoor, Z. Nezafat, M. Nasrollahzadeh, N. Manwar, P. Fornasiero and M. Gawande, *ACS Catal.*, 2022, **12**, 5605–5660.

18 X. Ge, A. Sumboja, D. Wuu, T. An, B. Li, F. W. T. Goh, T. S. A. Hor, Y. Zong and Z. Liu, *ACS Catal.*, 2015, **5**, 4643–4667.

19 M. Khan, N. K. Janjua, A. Ahmad, R. Luque, A. A. Al-Kahtani and A. M. Tighezza, *Int. J. Energy Res.*, 2022, **46**, 14161–14173.

20 R. Huang, Y. Wen, H. Peng and B. Zhang, *Chinese J. Catal.*, 2022, **43**, 130–138.

21 S. Sekhon, J. Lee and J. Park, *J. Energy Chem.*, 2022, **65**, 149–172.

22 Y. Yu, Y. Liu, X. Peng, X. Liu, Y. Xing and S. Xing, *Sustain. Energy Fuels*, 2020, **4**, 5156–5164.

23 S. Ahn and A. Manthiram, *J. Mater. Chem. A*, 2019, **7**, 8641–8652.

24 D. Liu, Y. Tong, X. Yan, J. Liang and S. X. Dou, *Batter. Supercaps*, 2019, **2**, 743–765.

25 M. Luo, W. Sun, B. Bin Xu, H. Pan and Y. Jiang, *Adv. Energy Mater.*, 2021, **11**,

2002762.
26 C. X. Zhao, J. N. Liu, J. Wang, D. Ren, J. Yu, X. Chen, B. Q. Li and Q. Zhang, *Adv. Mater.*, 2021, **33**, 1–8.
27 N. Wang, S. Ning, X. Yu, D. Chen, Z. Li, J. Xu, H. Meng, D. Zhao, L. Li, Q. Liu, B. Lu and S. Chen, *Appl. Catal. B Environ.*, 2022, **302**, 120838.
28 W. Zhu, H. Yuan, F. Liao, Y. Shen, H. Shi, Y. Shi, L. Xu, M. Ma and M. Shao, *Chem. Eng. J.*, 2020, **389**, 124240.
29 C. Zhou, X. Chen, S. Liu, Y. Han, H. Meng, Q. Jiang, S. Zhao, F. Wei, J. Sun, T. Tan and R. Zhang, *J. Am. Chem. Soc.*, 2022, **144**, 2694–2704.
30 M. Aizudin, W. Fu, R. Pottammel, Z. Dai, H. Wang, X. Rui, J. Zhu, C. Li, X. Wu and E. Ang, *Small*, 2023, 2305217.
31 P. Barman, L. Dutta and B. Azzopardi, *Energies*, 2023, **16**, 3369.
32 W. Yu, W. Shang, Y. He, Z. Zhao, Y. Ma and P. Tan, *Chem. Eng. J.*, 2022, **431**, 134032.
33 X. Zhu, C. Hu, R. Amal, L. Dai and X. Lu, *Energy Environ. Sci.*, 2020, **13**, 4536–4563.
34 Y.-J. Wang, W. Long, L. Wang, R. Yuan, A. Ignaszak, B. Fang and D. Wilkinson, *Energy Environ. Sci.*, 2018, **11**, 258–275.
35 X. Zhang, P. Lu, X. Cui, L. Chen, C. Zhang, M. Li, Y. Xu and J. Shi, *J. Catal.*, 2016, **344**, 455–464.
36 Y. Liu, X. Yue, K. Li, J. Qiao, D. Wilkinson and J. Zhang, *Coord. Chem. Rev.*, 2016, **315**, 153–177.
37 L. Yang, J. Shui, L. Du, Y. Shao, J. Liu, L. Dai and Z. Hu, *Adv. Mater.*, 2019, **31**, 1804799.
38 A. Brouzgou, S. Q. Song and P. Tsiakaras, *Appl. Catal. B Environ.*, 2012, **127**, 371–388.
39 J. Wu, X. Z. Yuan, J. J. Martin, H. Wang, J. Zhang, J. Shen, S. Wu and W. Merida, *J. Power Sources*, 2008, **184**, 104–119.
40 S. Ren, X. Duan, S. Liang, M. Zhang and H. Zheng, *J. Mater. Chem. A*, 2020, **8**, 6144–6182.
41 X. Yang, H. Mi, X. Ren, P. Zhang and Y. Li, *Nanoscale Res. Lett.*, 2020, **15**, 4–15.
42 S. Singh, K. Takeyasu and J. Nakamura, *Adv. Mater.*, 2019, **31**, 1804297.
43 X. Zhao, P. Pachfule, S. Li, T. Langenhahn, M. Ye, C. Schlesiger, S. Praetz, J. Schmidt and A. Thomas, *J. Am. Chem. Soc.*, 2019, **141**, 6623–6630.
44 S. Niu, S. Li, Y. Du, X. Han and P. Xu, *ACS Energy Lett.*, 2020, **5**, 1083–1087.
45 S. Xu, Y. Kim, D. Higgins, M. Yusuf, T. Jaramillo and F. Prinz, *Electrochim. Acta*, 2017, **255**, 99–108.
46 N. Suen, S. Hung, Q. Quan, N. Zhang, Y. Xu and H. Chen, *Chem. Soc. Rev.*, 2017, **46**, 337–365.
47 J. Nørskov, J. Rossmeisl, A. Logadottir, L. Lindqvist, J. Kitchin, T. Bligaard and H. Jónsson, *J. Phys. Chem. B*, 2004, **108**, 17886–17892.
48 D. M. Heard and A. Lennox, *Angew. Chemie Int. Ed.*, 2020, **59**, 18866–18884.
49 Z.-F. Huang, J. Wang, Y. Peng, C.-Y. Jung, A. Fisher and X. Wang, *Adv. Energy Mater.*, 2017, **7**, 1700544.
50 G. Zhong, S. Xu, L. Liu, C. Z. Zheng, J. Dou, F. Wang, X. Fu, W. Liao and H. Wang, *ChemElectroChem*, 2020, **7**, 1107–1114.

51 J. Wang, C.-X. Zhao, J.-N. Liu, D. Ren, B.-Q. Li, J.-Q. Huang and Q. Zhang, *Nano Mater. Sci.*, 2021, **3**, 313–318.
52 W. Chen, Q. Xiang, T. Peng, C. Song, W. Shang, T. Deng and J. Wu, *iScience*, 2020, **23**, 101532.
53 R. Nandan, O. Bisen and K. Nanda, *J. Phys. Chem. C*, 2021, **125**, 10378–10385.
54 K. Mayrhofer, D. Strmcnik, B. Blizanac, V. Stamenkovic, M. Arenz and N. Markovic, *Electrochim. Acta*, 2008, **53**, 3181–3188.
55 J. Wang, X. Duan, J. Gao, Y. Shen, X. Feng, Z. Yu, X. Tan, S. Liu and S. Wang, *Water Res.*, 2020, **185**, 116244.
56 J. Zhang and L. Dai, *ACS Catal.*, 2015, **5**, 7244–7253.
57 C. Hu and L. Dai, *Adv. Mater.*, 2019, **31**, 1804672.
58 D. Wang, X. Pan, P. Yang, R. Li, H. Xu, Y. Li, F. Meng, J. Zhang and M. An, *ChemSusChem*, 2021, **14**, 33–55.
59 J. Quílez-Bermejo, E. Morallón and D. Cazorla-Amorós, *Carbon N. Y.*, 2020, **165**, 434–454.
60 W. Zhang, X. Yao, S. Zhou, X. Li, L. Li, Z. Yu and L. Gu, *Small*, , DOI:10.1002/smll.201800423.
61 R. Ma, G. Lin, Y. Zhou, Q. Liu, T. Zhang, G. Shan, M. Yang and J. Wang, *npj Comput. Mater.*, , DOI:10.1038/s41524-019-0210-3.
62 D. Guo, R. Shibuya, C. Akiba, S. Saji, T. Kondo and J. Nakamura, *Science (80-.).*, 2016, **351**, 361–365.
63 C. Li, Q. Zheng, Q. Xiang, L. Yu, P. Chen, D. Gao, Q. Liu, F. He, D. Yu, Y. Liu and C. Chen, *J. Chem. Educ.*, 2021, **98**, 3026–3031.
64 F. Vidal-Iglesias, J. Solla-Gullón, V. Montiel and A. Aldaz, *Electrochem. commun.*, 2012, **15**, 42–45.
65 S. Treimer, A. Tang and D. Johnson, *Electroanalysis*, 2002, **14**, 165–171.
66 J. Li, *Nano-Micro Lett.*, 2022, **14**, 112.
67 Y. Bu, O. Gwon, G. Nam, H. Jang, S. Kim, Q. Zhong, J. Cho and G. Kim, *ACS Nano*, 2017, **11**, 11594–11601.
68 X. Wang, H. Zhong, S. Xi, W. S. V. Lee and J. Xue, *Adv. Mater.*, 2022, **34**, 1–27.
69 S. Chandrasekaran, D. Ma, Y. Ge, L. Deng, C. Bowen, J. Roscow, Y. Zhang, Z. Lin, R. D. K. Misra, J. Li, P. Zhang and H. Zhang, *Nano Energy*, 2020, **77**, 105080.
70 X. Li, Z. Cheng and X. Wang, *Electrochem. Energy Rev.*, 2021, **4**, 136–145.
71 X. Lv, Z. Xiao, H. Wang, X. Wang, L. Shan, F. Wang, C. Wei, X. Tang and Y. Chen, *J. Energy Chem.*, 2021, **54**, 626–638.
72 T. Ioroi, T. Nagai, Z. Siroma and K. Yasuda, *Int. J. Hydrogen Energy*, 2022, **47**, 38506–38516.
73 Y. L. Zhang, K. Goh, L. Zhao, X. L. Sui, X. F. Gong, J. J. Cai, Q. Y. Zhou, H. Da Zhang, L. Li, F. R. Kong, D. M. Gu and Z. B. Wang, *Nanoscale*, 2020, **12**, 21534–21559.
74 C. Zhao, J. Liu, J. Wang, D. Ren, J. Yu, X. Chen, B. Li and Q. Zhang, *Adv. Mater.*, 2021, **33**, 2008606.
75 Z. Jin, X. Zhou, Y. Hu, X. Tang, K. Hu, K. Reddy, X. Lin and H.-J. Qiu, *Chem. Sci.*, 2022, **13**, 12056–12064.
76 W. Gong, H. Zhang, L. Yang, Y. Yang, J. Wang and H. Liang, *J. Ind. Eng. Chem.*,

2022, **106**, 492–502.
77 K. Zeng, X. Zheng, C. Li, J. Yan, J. Tian, C. Jin, P. Strasser and R. Yang, *Adv. Funct. Mater.*, 2020, **30**, 2000503.
78 Y. Liang, Y. Han, J. Li, J. Wang, D. Liu and Q. Fan, *J. Energy Chem.*, 2022, **70**, 643–655.
79 D. Chen, J. Yu, Z. Cui, Q. Zhang, X. Chen, J. Sui, H. Dong, L. Yu and L. Dong, *Electrochim. Acta*, 2020, **331**, 135394.
80 X. Jia, S. Gao, T. Liu, D. Li, P. Tang and Y. Feng, *Electrochim. Acta*, 2017, **245**, 59–68.
81 M. Ma, A. Kumar, D. Wang, Y. Wang, Y. Jia, Y. Zhang, G. Zhang, Z. Yan and X. Sun, *Appl. Catal. B Environ.*, 2020, **274**, 119091.
82 G. Li, Y. Tang, T. Fu, Y. Xiang, Z. Xiong, Y. Si, C. Guo and Z. Jiang, *Chem. Eng. J.*, 2022, **429**, 132174.
83 Z. Liu, Z. Zhao, Y. Wang, S. Dou, D. Yan, D. Liu, Z. Xia and S. Wang, *Adv. Mater.*, 2017, **29**, 1606207.
84 T. Asefa, *Acc. Chem. Res.*, 2016, **49**, 1873–1883.
85 L. Gao, M. Zhu, Z. Zhang and G. Cui, *Electrochim. Acta*, 2019, **327**, 134980.
86 Q. Zhao, Y. Meng, J. Li and D. Xiao, *Appl. Surf. Sci.*, 2019, **481**, 473–483.
87 T. Van Tam, S. G. Kang, M. H. Kim, S. G. Lee, S. H. Hur, J. S. Chung and W. M. Choi, *Adv. Energy Mater.*, 2019, **9**, 1–11.
88 H. Elhousseini, H. Younus, S. Chaemchuen, S. Dekyvere, X. Zen, D. He, J. Park, T. Han and F. Verpoort, *Catal. Sci. Technol.*, 2021, **11**, 4149–4161.
89 J. Sanetuntikul, S. Hyun, P. Ganesan and S. Shanmugam, *J. Mater. Chem. A*, 2018, **6**, 24078–24085.
90 Y. Liu, J. Bao, Z. Li, L. Zhang, S. Zhang, L. Wang, X. Niu, P. Sun and L. Xu, *J. Colloid Interface Sci.*, 2022, **607**, 1201–1214.
91 J.-C. Li, P.-X. Hou, M. Cheng, C. Liu, H.-M. Cheng and M. Shao, *Carbon N. Y.*, 2018, **139**, 156–163.
92 N. Deng, Q. Zeng, Y. Feng, H. Gao, G. Wang, J. Yan, T. Zheng, Y. Liu, W. Kang and B. Cheng, *Catal. Sci. Technol.*, 2023, **13**, 4823–4838.
93 C. Xie, D. Yan, H. Li, S. Du, W. Chen, Y. Wang, Y. Zou, R. Chen and S. Wang, *ACS Catal.*, 2020, **10**, 11082–11098.
94 M. Yu, R. Dong and X. Feng, *J. Am. Chem. Soc.*, 2020, **142**, 12903–12915.
95 Y. Ni, L. Lin, Y. Shang, L. Luo, L. Wang, Y. Lu, Y. Li, Z. Yan, K. Zhang, F. Cheng and J. Chen, *Angew. Chemie Int. Ed.*, 2021, **60**, 16937–16941.
96 Y. Xie, C. Feng, Y. Guo, S. Li, C. Guo, Y. Zhang and J. Wang, *Appl. Surf. Sci.*, 2021, **536**, 147786.
97 L. Lu, Y. Zheng, R. Yang, A. Kakimov and X. Li, *Mater. Today Chem.*, , DOI:10.1016/j.mtchem.2021.100488.
98 Q. Zhai, Y. Pan and L. Dai, *Accounts Mater. Res.*, 2021, **2**, 1239–1250.
99 X. Wen, X. Yang, M. Li, L. Bai and J. Guan, *Electrochim. Acta*, 2019, **296**, 830–841.
100 Y.-J. Wang, H. Fan, A. Ignaszak, L. Zhang, S. Shao, D. Wilkinson and J. Zhang, *Chem. Eng. J.*, 2018, **348**, 416–437.
101 H. F. Wang, L. Chen, H. Pang, S. Kaskel and Q. Xu, *Chem. Soc. Rev.*, 2020, **49**, 1414–1448.

102 K. Zhang, W. Mai, J. Li, G. Li, L. Tian and W. Hu, *ACS Appl. Nano Mater.*, 2019, **2**, 5931–5941.
103 Z. Pei, Z. Tang, Z. Liu, Y. Huang, Y. Wang, H. Li, Q. Xue, M. Zhu, D. Tang and C. Zhi, *J. Mater. Chem. A*, 2018, **6**, 489–497.
104 M. Li, S. Chen, B. Li, Y. Huang, X. Lv, P. Sun, L. Fang and X. Sun, *Electrochim. Acta*, 2021, **388**, 138587.
105 C. Liu, J. Wang, J. Wan and C. Yu, *Coord. Chem. Rev.*, 2021, **432**, 213743.
106 S. Chui, S. Lo, J. Charmant, A. Orpen and I. Williams, *Science (80-.).*, 1999, **283**, 1148–1150.
107 L. Chai, L. Zhang, X. Wang, L. Xu, C. Han, T.-T. Li, Y. Hu, J. Qian and S. Huang, *Carbon N. Y.*, 2019, **146**, 248–256.
108 S. Gao, B. Fan, R. Feng, C. Ye, X. Wei, J. Liu and X. Bu, *Nano Energy*, 2017, **40**, 462–470.
109 N. Patterson, B. Xiao and A. Ignaszak, *RSC Adv.*, 2020, **10**, 20162–20172.
110 Z. Hu, T. Kundu, Y. Wang, Y. Sun, K. Zeng and D. Zhao, *ACS Sustain. Chem. Eng.*, 2020, **8**, 17042–17053.
111 Q. Ren, H. Wang, X. Lu, Y. Tong and G. Li, *Adv. Sci.*, 2018, **5**, 1700515.
112 I. Khan, Y. Qian, A. Badshah, M. Nadeem and D. Zhao, *ACS Appl. Mater. Interfaces*, 2016, **8**, 17268–17275.
113 E. Ploetz, H. Engelke, U. Lächelt and S. Wuttke, *Adv. Funct. Mater.*, 2020, **30**, 1909062.
114 C. Duan, Y. Yu and H. Hu, *Green Energy Environ.*, 2022, **7**, 3–15.
115 Y. Li, M. Cui, T. Li, Y. Shen, Z. Si and H. guo Wang, *Int. J. Hydrogen Energy*, 2020, **45**, 16540–16549.
116 C. Feng, Y. Guo, S. Qiao, Y. Xie, L. Zhang, L. Zhang, W. Wang and J. Wang, *Appl. Surf. Sci.*, 2020, **533**, 147481.
117 K. Kida, M. Okita, K. Fujita, S. Tanaka and Y. Miyake, *CrystEngComm*, 2013, **15**, 1794–1801.
118 M. U. Tahir, H. Arshad, H. Zhang, Z. Hou, J. Wang, C. Yang and X. Su, *J. Colloid Interface Sci.*, 2020, **579**, 195–204.
119 E. L. Bustamante, J. L. Fernández and J. M. Zamaro, *J. Colloid Interface Sci.*, 2014, **424**, 37–43.
120 C. Tong, G. Cai, Y. Yang, T. Wang, Y. Yang, Y. Chen, S. Shi, L. Wu and Y. Guo, *J. Mater. Chem. C*, 2023, **11**, 1872–1878.
121 A. Pichon, A. Lazuen-Garay and S. James, *CrystEngComm*, 2006, **8**, 211.
122 Y. Miao, D. T. Lee, M. D. de Mello, M. Ahmad, M. K. Abdel-Rahman, P. M. Eckhert, J. A. Boscoboinik, D. H. Fairbrother and M. Tsapatsis, *Nat. Commun.*, 2022, **13**, 1–8.
123 Y. Xiao, A. N. Hong, D. Hu, Y. Wang, X. Bu and P. Feng, *Chem. - A Eur. J.*, 2019, **25**, 16358–16365.
124 J. Wang, S. Chaemchuen, N. Klomkliang and F. Verpoort, *Cryst. Growth Des.*, 2021, **21**, 5349–5359.
125 J. López-Cabrelles, J. Romero, G. Abellán, M. Giménez-Marqués, M. Palomino, S. Valencia, F. Rey and G. Mínguez Espallargas, *J. Am. Chem. Soc.*, 2019, **141**, 7173–7180.
126 F. Tang, W. Xia, H. Zhang, L. Zheng, Y. Zhao, J. Ge and J. Tang, *Nano Res.*,

2022, **15**, 6670–6677.
127 A. Abidin, K. Loh, W. Wong, A. Mohamad and I. Puspasari, *Int. J. Hydrogen Energy*, 2018, **43**, 11047–11055.
128 J. Sha, S. Jiang, D. Cai, Y. Xue, G. Li, Z. Xiong, Y. Lei, Y. Si, P. He and C. Guo, *Mater. Sci. Eng. B*, 2023, **290**, 116291.
129 B. Costa, I. Rosa, V. Silva, Q. Wu, R. Samulewski, F. Scacchetti, M. Moisés, M. Lis and F. Bezerra, *Polymers (Basel).*, 2022, **14**, 4256.
130 N. Patterson, B. Xiao and A. Ignaszak, *RSC Adv.*, 2020, **10**, 20162–20172.
131 W. James, C. Sullivan and N. Marshall, *CrystEngComm*, 2021, **23**, 4938–4945.
132 M. Safaei, M. Foroughi, N. Ebrahimpoor, S. Jahani, A. Omidi and M. Khatami, *TrAC Trends Anal. Chem.*, 2019, **118**, 401–425.
133 J. Ethiraj, S. Palla and H. Reinsch, *Microporous Mesoporous Mater.*, 2020, **294**, 109867.
134 H. Zhou, W. Cao, N. Sun, L. Jiang, Y. Liu and H. Pang, *Chinese Chem. Lett.*, 2021, **32**, 3123–3127.
135 L. Shrestha, R. Shrestha, Y. Yamauchi, J. Hill, T. Nishimura, K. Miyazawa, T. Kawai, S. Okada, K. Wakabayashi and K. Ariga, *Angew. Chemie*, 2015, **127**, 965–969.
136 W. Li, K. Yang, J. Peng, L. Zhang, S. Guo and H. Xia, *Ind. Crops Prod.*, 2008, **28**, 190–198.
137 C. Falco, J. Marco-Lozar, D. Salinas-Torres, E. Morallón, D. Cazorla-Amorós, M. Titirici and D. Lozano-Castelló, *Carbon N. Y.*, 2013, **62**, 346–355.
138 R. Crocombe, *Appl. Spectrosc.*, 2018, **72**, 1701–1751.
139 E. Paschalis, K. Verdelis, S. Doty, A. Boskey, R. Mendelsohn and M. Yamauchi, *J. Bone Miner. Res.*, 2001, **16**, 1821–1828.
140 B. Ingham, *Crystallogr. Rev.*, 2015, **21**, 229–303.
141 J. Lefebvre, F. Galli, C. Bianchi, G. Patience and D. Boffito, *Can. J. Chem. Eng.*, 2019, **97**, 2588–2593.
142 M. Isaacs, J. Davies-Jones, P. Davies, S. Guan, R. Lee, D. Morgan and R. Palgrave, *Mater. Chem. Front.*, 2021, **5**, 7931–7963.
143 D. Krishna and J. Philip, *Appl. Surf. Sci. Adv.*, 2022, **12**, 100332.
144 A. Aarva, V. Deringer, S. Sainio, T. Laurila and M. Caro, *Chem. Mater.*, 2019, **31**, 9243–9255.
145 K. Mauritz and R. Moore, *Chem. Rev.*, 2004, **104**, 4535–4586.
146 H. Rasouli, L. Naji and M. Hosseini, *RSC Adv.*, 2017, **7**, 3190–3203.
147 F. Scholz, *ChemTexts*, 2015, **1**, 17.
148 X. Huang, Z. Wang, R. Knibbe, B. Luo, S. Ahad, D. Sun and L. Wang, *Energy Technol.*, 2019, **7**, 1801001.
149 T. Dobbelaere, P. Vereecken and C. Detavernier, *HardwareX*, 2017, **2**, 34–49.
150 N. Raeisi-Kheirabadi, A. Nezamzadeh-Ejhieh and H. Aghaei, *ACS Omega*, 2022, **7**, 31413–31423.
151 A. Radhakrishnan and B. Beena, *Indian J. Adv. Chem. Sci.*, 2014, **2**, 158–161.
152 R. Lin, L. Ge, H. Diao, V. Rudolph and Z. Zhu, *ACS Appl. Mater. Interfaces*, 2016, **8**, 32041–32049.
153 Q. Ain, S. Haq, A. Alshammari, M. Al-Mutlaq and M. Anjum, *Beilstein J. Nanotechnol.*, 2019, **10**, 901–911.

154 A. Zarnegaryan and Z. Dehbanipour, *Appl. Surf. Sci. Adv.*, 2021, **4**, 100074.
155 I. Faniyi, O. Fasakin, B. Olofinjana, A. Adekunle, T. Oluwasusi, M. Eleruja and E. Ajayi, *SN Appl. Sci.*, 2019, **1**, 1181.
156 I. Jang, S. Hajra, R. Sahu and H. Kim, *Sensors Actuators B Chem.*, 2023, **396**, 134589.
157 H. Han, X. Yuan, Z. Zhang and J. Zhang, *Inorg. Chem.*, 2019, **58**, 3196–3202.
158 E. Andris, R. Navrátil, J. Jašík, G. Sabenya, M. Costas, M. Srnec and J. Roithová, *Chem. – A Eur. J.*, 2018, **24**, 5078–5081.
159 M. Afkhami-Ardekani, M. Naimi-Jamal, S. Doaee and S. Rostamnia, *Catalysts*, 2022, **13**, 9.
160 C. Valencia, C. Valencia, F. Zuluaga, M. Valencia, J. Mina and C. Grande-Tovar, *Molecules*, 2018, **23**, 2651.
161 M. Raffi, S. Mehrwan, T. Bhatti, J. Akhter, A. Hameed, W. Yawar and M. Hasan, *Ann. Microbiol.*, 2010, **60**, 75–80.
162 S. Sundriyal, V. Shrivastav, H. Kaur, S. Mishra and A. Deep, *ACS Omega*, 2018, **3**, 17348–17358.
163 K. Zhu, J. Liu, S. Li, L. Liu, L. Yang, S. Liu, H. Wang and T. Xie, *Adv. Mater. Interfaces*, 2017, **4**, 1700377.
164 M. Rouhani, J. Hobley, F. Chau-Nan Hong and Y.-R. Jeng, *Carbon N. Y.*, 2021, **184**, 772–785.
165 A. Farha, A. Al Naim, J. Mazher, O. Nasr and M. Alouane, *Materials (Basel).*, 2020, **13**, 879.
166 G. Raja, A. Nallathambi, A. Prakasam, S. Gopinath, C. Ragupathi, S. Narayanan, P. Tamizhdurai, R. Kumaran, N. Alsaiari, K. Abualnaja and M. Ouladsmane, *J. Saudi Chem. Soc.*, 2022, **26**, 101440.
167 R. Siburian, H. Sihotang, S. Lumban, M. Supeno and C. Simanjuntak, *Orient. J. Chem.*, 2018, **34**, 182–187.
168 S. Feng, X. Jia, J. Yang, Y. Li, S. Wang and H. Song, *J. Mater. Sci. Mater. Electron.*, 2020, **31**, 22534–22545.
169 N. Dwivedi, R. Yeo, N. Satyanarayana, S. Kundu, S. Tripathy and C. Bhatia, *Sci. Rep.*, 2015, **5**, 7772.
170 Y. Wu, Y. Lin and J. Xu, *Photochem. Photobiol. Sci.*, 2019, **18**, 1081–1091.
171 R. Murakami, H. Kageyama, K. Nakamura, H. Tanaka, H. Shinotsuka, H. Yoshikawa and K. Yoshihara, *e-Journal Surf. Sci. Nanotechnol.*, 2019, **17**, 61–68.
172 A. Jindal, S. Basu and A. P, *RSC Adv.*, 2015, **5**, 69378–69387.
173 J. Wang and Y. Mo, *J. Chem. Phys.*, , DOI:10.1063/1.5087865.
174 M. C. Biesinger, *Surf. Interface Anal.*, 2017, **49**, 1325–1334.
175 A. Domán, B. Nagy, L. P. Nichele, D. Srankó, J. Madarász and K. László, *Appl. Surf. Sci.*, 2018, **434**, 1300–1310.
176 W. Xia, J. Zhu, W. Guo, L. An, D. Xia and R. Zou, *J. Mater. Chem. A*, 2014, **2**, 11606–11613.
177 P. Fu, S. Hu, J. Xiang, L. Sun, S. Su and J. Wang, *J. Anal. Appl. Pyrolysis*, 2012, **98**, 177–183.
178 X. Ye, Z. Chen, S. Ai, B. Hou, J. Zhang, Q. Zhou, H. Liu and S. Cui, *Mater. Res. Express*, 2019, **6**, 075601.
179 L. Leng, Q. Xiong, L. Yang, H. Li, Y. Zhou, W. Zhang, S. Jiang, H. Li and H.

Huang, *Sci. Total Environ.*, 2021, **763**, 144204.
180 Z. Liu, F. Zhen, Q. Zhang, X. Qian, W. Li, Y. Sun, L. Zhang and B. Qu, *Bioresour. Technol.*, 2022, **359**, 127471.
181 Y. Gao, Z. Xiao, D. Kong, R. Iqbal, Q.-H. Yang and L. Zhi, *Nano Energy*, 2019, **64**, 103879.
182 W.-Y. Yan, S.-L. Zheng, W. Jin, Z. Peng, S.-N. Wang, H. Du and Y. Zhang, *J. Electroanal. Chem.*, 2015, **741**, 100–108.
183 A. Garcia and M. Koper, *ACS Catal.*, 2018, **8**, 9359–9363.
184 C. Do, T. Pham, N. Nguyen and V. Tran, *Adv. Nat. Sci. Nanosci. Nanotechnol.*, 2013, **4**, 035011.
185 Y. Li and H. Dai, *Chem. Soc. Rev.*, 2014, **43**, 5257–5275.
186 D. Yang, L. Zhang, X. Yan and X. Yao, *Small Methods*, 2017, **1**, 1700209.
187 S. Prass, J. St-Pierre, M. Klingele, K. Friedrich and N. Zamel, *Electrocatalysis*, 2021, **12**, 45–55.
188 H.-S. Park, E. Seo, J. Yang, Y. Lee, B.-S. Kim and H.-K. Song, *Sci. Rep.*, 2017, **7**, 7150.
189 R. Zhou, Y. Zheng, M. Jaroniec and S.-Z. Qiao, *ACS Catal.*, 2016, **6**, 4720–4728.
190 I. Dumitrescu and R. M. Crooks, *Proc. Natl. Acad. Sci.*, 2012, **109**, 11493–11497.
191 W. Chen, Q. Xiang, T. Peng, C. Song, W. Shang, T. Deng and J. Wu, *iScience*, 2020, **23**, 101532.
192 X. Kong, Y. Zhu, H. Lei, C. Wang, Y. Zhao, E. Huo, X. Lin, Q. Zhang, M. Qian, W. Mateo, R. Zou, Z. Fang and R. Ruan, *Chem. Eng. J.*, 2020, **399**, 125808.
193 G. Zhou, G. Liu, X. Liu, Q. Yu, H. Mao, Z. Xiao and L. Wang, *Adv. Funct. Mater.*, , DOI:10.1002/adfm.202107608.
194 F. Boorboor Ajdari, E. Kowsari and A. Ehsani, *J. Colloid Interface Sci.*, 2018, **509**, 189–194.
195 Z. Liu, D. Ye, X. Zhu, S. Wang, Y. Zou, L. Lan, R. Chen, Y. Yang and Q. Liao, *Chem. Eng. J.*, 2022, **432**, 134192.
196 Z. Duan and G. Henkelman, *J. Phys. Chem. C*, 2020, **124**, 12016–12023.
197 J. Masa, W. Xia, M. Muhler and W. Schuhmann, *Angew. Chemie Int. Ed.*, 2015, **54**, 10102–10120.

Curriculum Vitae

Candidate's full name: Hamidreza Parsimehr

Universities attended:
University of Qom (2010-2014), Bachelor of Science in Applied Chemistry
Iran Polymer and Petrochemical Institute (2014-2017), Master of Science in Polymer Chemistry
University of New Brunswick (2021-Ongoing), Master of Science in Chemistry

Publications: (Sorted by publication date)
Parsimehr, Hamidreza, et al. "Waste-to-Wealth: Wheat-Based Porous Electrodes for Electrochemical Energy Storage Devices." ECS Advances 2.2 (2023): 020503.

Moharramnejad, Mojtaba, et al. "Cobalt-based electroactive compounds: synthesis and their electrochemical and pseudocapacitance performance." Journal of Materials Science: Materials in Electronics 34.6 (2023): 499.

Moharramnejad, Mojtaba, et al. "Zinc-based metal-organic frameworks: Synthesis and recent progress in biomedical application." Journal of Inorganic and Organometallic Polymers and Materials 32.9 (2022): 3339-3354.

Parsimehr, Hamidreza, et al. "Stimuli-Responsive Electrochemical Energy Storage Devices." The Chemical Record 22.9 (2022): e202200075.

Rastegar, Niloofar, et al. "Sound-absorbing porous materials: a review on polyurethane-based foams." Iranian Polymer Journal (2022): 1-23.

Parsimehr, Hamidreza, et al. "Electrochemical energy storage electrodes from rice biochar." Biomass conversion and biorefinery (2022): 1-17.

Parsimehr, Hamidreza, et al. "Energy harvesting/storage and environmental remediation via hot drinks wastes." The Chemical Record 21.5 (2021): 1098-1118.

Goharshenas Moghadam, Saba, et al. "Multifunctional superhydrophobic surfaces." Advances in Colloid and Interface Science 290 (2021): 102397.

Parsimehr, Hamidreza, et al. "Ambient temperature cross-linkable acrylic latexes: effect of cross-link density, glass transition temperature and application temperature difference on mechanical properties." Polymer Bulletin (2021): 1-20.

Ehsani, Ali, et al. "Functionalized graphene oxide aerogel as a high efficient material for electrochemical sensing of organic pollutant." Surfaces and Interfaces 22 (2021): 100817.

Ehsani, Ali, et al. "Influence of nanostructured VO-acetylacetonate coordination system with 2-(pyridin-4-ylmethylene) hydrazine-1-carbothioamide in pseudocapacitance

performance of p-type conductive polymer composite film." Plastics, Rubber and Composites 50.4 (2021): 172-179.

Parsimehr, Hamidreza, et al. "Algae-based electrochemical energy storage devices." Green Chemistry 22.23 (2020): 8062-8096.

Ehsani, Ali, and Hamidreza Parsimehr. "Electrochemical energy storage electrodes from fruit biochar." Advances in Colloid and Interface Science 284 (2020): 102263.

Parsimehr, Hamidreza, and Ali Ehsani. "Corn-based Electrochemical Energy Storage Devices." The Chemical Record 20.10 (2020): 1163-1180.

Moradi, Gholamreza, et al. "Organoclay nanoparticles interaction in PU: PMMA IPN foams: Relationship between the cellular structure and damping-acoustical properties." Applied Acoustics 164 (2020): 107295.

Azadi, Nasim, et al. "Cultural heritage protection via hybrid nanocomposite coating." Plastics, Rubber and Composites 49.9 (2020): 414-424.

Ehsani, Ali, et al. "Electrochemical energy storage electrodes via citrus fruits derived carbon: a minireview." The Chemical Record 20.8 (2020): 820-830.

Ehsani, Ali, et al. "Environment-friendly electrodes using biopolymer chitosan/poly ortho aminophenol with enhanced electrochemical behavior for use in energy storage devices." Polymer Composites 40.12 (2019): 4629-4637.

Conference Presentations: (Sorted by publication date)
R3 Cleantech: Advancing Climate Innovation, Fredericton, NB, Canada (2023)
4th National Conference on the Pavement marking, Iran Polymer and Petrochemical Institute (IPPI), Tehran, Iran. (2016)